Heterogeneous Condensation of the Lennard-Jones Vapour onto Nanoscale Particles

A Thesis Submitted to the
College of Graduate Studies and Research
in Partial Fulfillment of the Requirements
for the degree of Doctor of Philosophy
in the Department of Chemistry
University of Saskatchewan
Saskatoon

By
Levent Inci

Permission to Use

In presenting this thesis in partial fulfilment of the requirements for a Postgraduate degree from the University of Saskatchewan, I agree that the Libraries of this University may make it freely available for inspection. I further agree that permission for copying of this thesis in any manner, in whole or in part, for scholarly purposes may be granted by the professor or professors who supervised my thesis work or, in their absence, by the Head of the Department or the Dean of the College in which my thesis work was done. It is understood that any copying or publication or use of this thesis or parts thereof for financial gain shall not be allowed without my written permission. It is also understood that due recognition shall be given to me and to the University of Saskatchewan in any scholarly use which may be made of any material in my thesis.

Requests for permission to copy or to make other use of material in this thesis in whole or part should be addressed to:

Head of the Department of Chemistry
176 Thorvaldson Building
110 Science Place
University of Saskatchewan
Saskatoon, Saskatchewan
Canada
S7N 5C9

Abstract

The heterogeneous condensation of a vapour onto a substrate is a key step in a wide range of chemical and physical process that occur in both nature and technology. For example, dust and pollutant aerosol particles, ranging in size from several microns down to just a few nanometers, serve as cloud condensation nuclei in the atmosphere, and nanoscale structured surfaces provide templates for the controlled nucleation and growth of variety of complex materials. While much is known about the general features of heterogeneous nucleation onto macroscopic surfaces, much less is understood about both the dynamics and thermodynamics of nucleation involving nanoscale heterogeneities. The goal of this thesis is to understand the general features of condensation of vapours onto different types of nanoscale heterogeneity that range in degree of solubility from being insoluble, to partially miscible through to completely miscible.

The heterogeneous condensation of the Lennard-Jones vapour onto an insoluble nanoscale seed particle is studied using a combination of molecular dynamics simulations and thermodynamic theory. The nucleation rate and free energy barrier are calculated from molecular dynamics using the mean first passage time method. These results show that the presence of a weakly interacting seed has no effect on the formation of small cluster embryos but accelerates the rate by lowering the free energy barrier of the larger clusters. A simple phenomenological model of film formation on a small seed is developed by extending the capillarity based liquid drop model. It captures the general features of heterogeneous nucleation, but a comparison with the simulation results show that the model significantly overestimates the height of the nucleation barrier while providing good estimates of the critical film size.

A non-volatile liquid drop model that accounts for solution non-ideality is developed to describe the thermodynamics of partially miscible and fully miscible droplets in a solvent vapour. The model shows ideal solution drops dissolve always spontaneously, but partially miscible drops exhibit a free energy surface with two minima, associated with a partially dissolved drop and a fully dissolved drop, separated by a free energy barrier. The solubility transition between the two drops is shown to follow a hysteresis loop as a function of system volume similar to that observed in deliquescence. A simple lattice gas model describing the absorption of mono-layers of vapour onto the particle is also developed.

Finally, molecular dynamics simulation of miscible and partially miscible binary Lennard-Jones mixtures are also used to study this system. For all cases studied, condensation onto the drop occurs spontaneously. Sub-monolayers of the solvent phase form when the system volume is large. At smaller system volumes, complete film formation is observed and the dynamics of film growth are dominated by cluster-cluster coalescence. Some degree of mixing into the core of the particle is observed for the miscible mixtures for all volumes. However, mixing of the solvent into the particle core only occurs below an onset volume for the partially miscible case, suggesting the presence of a solubility transition similar to the one described by the thermodynamic model.

Acknowledgements

This work would not have been possible without the support and encouragement of Dr. Richard Bowles, for this I am very grateful. I would also like to thank the Department of Chemistry and my supervisor for financial support throughout my studies.

I would also like to thank the members of my Ph.D. committee Dr. Ian Burgess, Lee Wilson and John Tse, for their help and support.

Thanks also to the past and present members of our research group, especially to Cletus, Mehdi and Ashwin, whose friendship and interest have made this task enjoyable.

Finally, I am very thankful to my family.

This thesis is dedicated to my family

Contents

List of Tables

List of Figures

Chapter 1

Introduction

When a vapour becomes supersaturated with respect to the equilibrium vapour pressure of the bulk liquid, it becomes metastable and the system can lower its free energy by transforming to the more stable equilibrium liquid. However, if the vapour is only mildly supersaturated and is between the binodal and spinodal lines of the phase diagram, then the phase change occurs via an activated process called nucleation. At a molecular level, this involves the formation of small clusters, resulting from density fluctuations, that must overcome a free energy barrier before they are able to grow into a new phase. The ability of the clusters to overcome this barrier controls the kinetics of the phase transformation.

Understanding how metastable systems change phase is important to a wide range of naturally occurring processes, like rain formation in the atmosphere [1, 2], to engineering applications such as the controlled formation of complex structures in colloidal photonic-crystals [3]. The main goal of the thesis is to study the nucleation kinetics of vapour condensation in the presence of heterogeneities, which help to accelerate the phase change, using thermodynamics, statistical mechanics and molecular simulation. This chapter will provide a literature review of the main theoretical and technical aspects of nucleation with an emphasis on heterogeneous nucleation in a supersaturated vapour. Section 1.1 covers theory of nucleation and gives details for both homogeneous and heterogeneous nucleations. Then, the role of heterogeneous nucleation in nature and technology will be surveyed and the connections to the current work highlighted. In section 1.2, the background details of the molecular dynamics simulations and mean first passage time methods are presented. The scope of the research presented in this thesis is outlined in section 1.3

1.1 Theory of Nucleation

1.1.1 Phase Stability and Metastability

A phenomenological approach using bulk thermodynamics provides a starting point for understanding the concepts of phase stability and metastability, here, we follow the development described by Debenedetti [4]. In an isolated system of fixed energy, U, volume, V and number of particles or mass, N, the system is in equilibrium if,

$$(\Delta \bar{S})_{U,V,N} \leq 0 \text{ or } (\Delta U)_{\bar{S},V,N} \geq 0, \tag{1.1}$$

where $\bar{S}$ is the entropy and delta (Δ) represents variations along a path from equilibrium to another state with the subscript variables held constant. That is, at equilibrium, $\bar{S}$ is a maximum along a path with U, V, N held constant and U is a maximum along a path with $\bar{S}, V, N$ held constant. These inequalities are necessary and sufficient conditions for equilibrium. However, entropy and energy are not easily controlled experimentally and alternative equilibrium criteria can be obtained in terms of the Helmholtz, F, and Gibbs, G, free energies,

$$(\Delta F)_{T,V,N} \geq 0, \tag{1.2}$$

$$(\Delta G)_{T,P,N} \geq 0, \tag{1.3}$$

where T is the temperature and P is the pressure.

Eqs. 1.1- 1.3 define the equilibrium conditions for various systems but to understand thermodynamic stability it is necessary to know how a system responds to small fluctuations about its equilibrium state. In the case of the isolated system considered in Eq. 1.1, this can be evaluated by expanding the energy with respect to small variations, δ, to give

$$[\delta U + \frac{1}{2}\delta^2 U + ...]_{\bar{S},V,N} \geq 0. \tag{1.4}$$

For a stable equilibrium the first term in Eq. 1.4 , $\delta U \mid_{\bar{S},V,N} = 0$, but the second terms should be positive, $\delta^2 U \mid_{\bar{S},V,N} > 0$. Therefore, when $\delta^2 U \mid_{\bar{S},V,N} = 0$ the system reaches a limit of stability. Fig. 1.1 provides a generic free energy picture highlighting the features of stability and metastability. The stable equilibrium phase represents the lowest global free energy state of the system. The metastable state is a local free energy minimum separated from the global minimum by a barrier. In both of these states, the local curvature of the free

energy surface returns small fluctuations back to the equilibrium state, but large fluctuations away from the metastable state will allow the system to move towards the stable equilibrium state. The free energy maximum represents an unstable equilibrium. At the limit of stability (Fig. 1.1b), the metastable phase also becomes unstable to even the smallest of fluctuations as the free energy surface decreases monotonically towards the stable state.

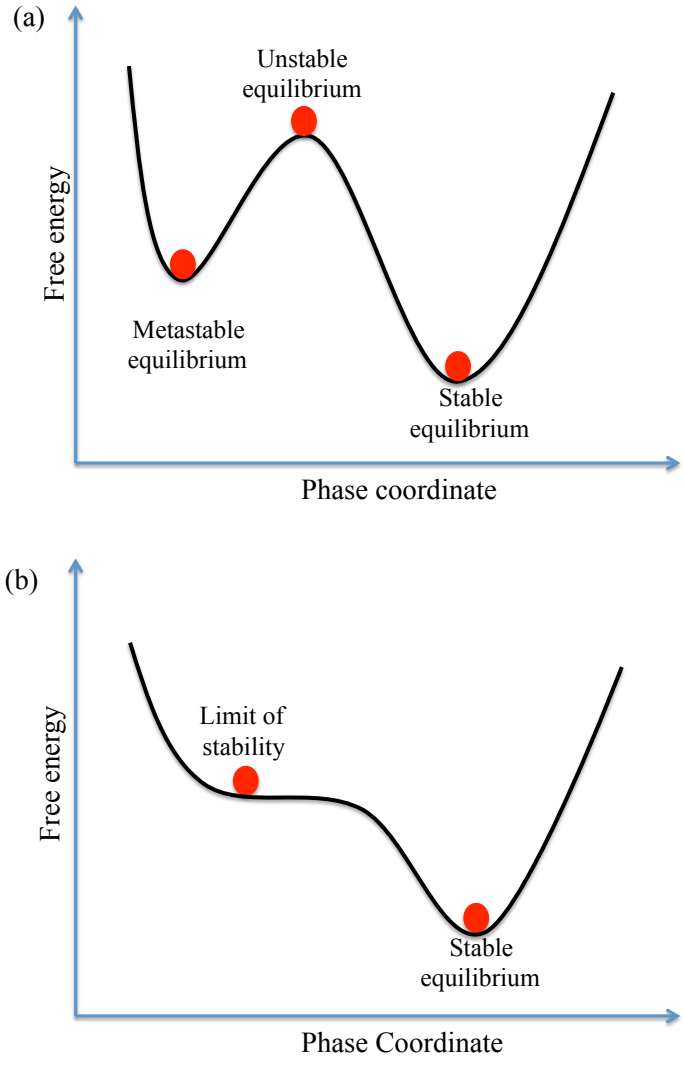

Figure 1.1: The evolution of the system from a metastable equilibrium to a stable equilibrium.

The Van der Waals equation of state [5] (EOS),

$$P = \frac{\rho kT}{1-\rho b} - \rho^2 a. \tag{1.5}$$

where a and b are material dependent constants, and ρ is the molecules per unit volume ($\rho = N/V$), provides the simplest example of a system with a first order phase transition between a vapour and liquid. Fig 1.2 plots an isotherm for the system and highlights the main features of the EOS and its connection with metastability. The solid black curve, **bcb′,** denotes the equilibrium coexistence line between the two phases which is also known as the binodal line. The coexistence pressure, P_1 (denoted by the dashed line), along an isotherm, T_1 is located using the Maxwell equal areas construction, between points **bed** and **dfb′**. The limit of stability conditions can be rewritten in terms of variables of the EOS,

$$\left(\frac{\partial P}{\partial v}\right)_{T,N} = 0, \ \left(\frac{\partial^2 P}{\partial v^2}\right)_{T,N} = 0. \tag{1.6}$$

where v is the volume per molecule.

Thus, the limit of stability points represent maxima and minima on the equation of state and the locus of limits of stability points (line **ecf**) is called the spinodal curve. Point **c** represents the critical point. The area between the coexistence line and spinodal, shown by gray in Fig. 1.2, is the metastable region where states between **b** and **e** correspond to the stretched uniform liquid and states between **b′** and **f** correspond to the supersaturated vapour. States between **e** and **f** represents the unstable region. In the metastable region, the phase transition occurs by nucleation, which is an activated process, and a free anergy barrier must be surmounted to form a large enough nucleus. However, in the unstable region the transition occurs by spinodal decomposition which is a spontaneous process and no free energy barrier must be overcome.

1.1.2 Homogeneous Nucleation

Nucleation is the process where fluctuations create a small nuclei of a new phase within a parent phase. Formation of rain droplets, crystallization, gas bubbles in a carbonated liquid are some examples in which nucleation plays an important role. In the absence of impurities, this process is called the homogeneous nucleation. This is a rare event since it relies on the formation of critical nucleus described by classical nucleation theory (CNT) in which a free

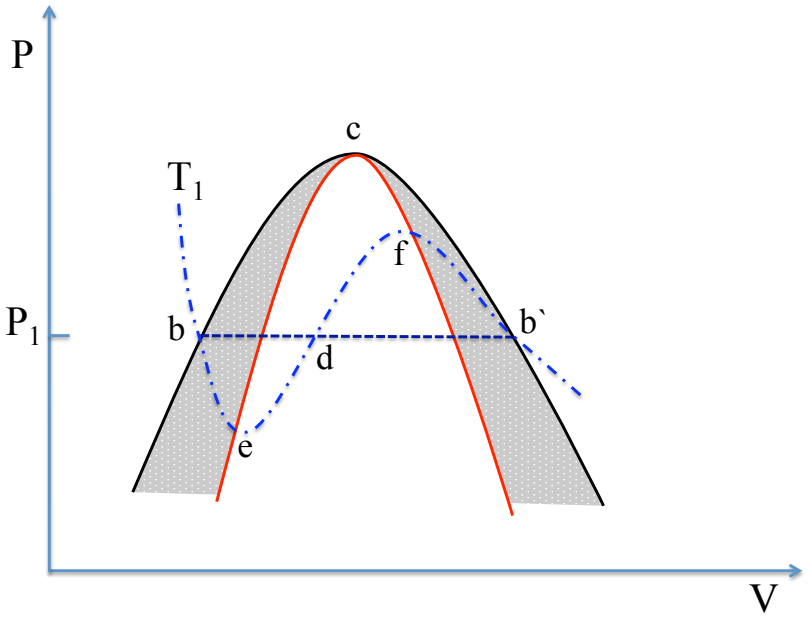

Figure 1.2: Pressure versus volume phase diagram in vapour liquid equilibrium corresponding to a subcritical temperature T_1.

energy barrier must be overcome to form this critical size nucleus and then the new phase grows spontaneously [4, 6, 7, 8, 9, 10].

CNT provides a basis for describing the rate of nucleation in terms of the number of droplets of the new phase formed per unit time per unit volume. In a supersaturated vapour, small embryos of new phase are created and destroyed as a result of density fluctuations. Suppose that there is no molecular association in the metastable gas and that the concentration of embryos consisting of n monomers is small, then embryos can only grow or shrink in size by adding or losing single molecules or atoms. Under these conditions we can write the rate of forming an n-sized embryo, $J(n)$, is the difference between the growth rate and the decay rate [4, 10] which can be expressed,

$$J(n) = f(n-1)A(n-1)\beta(n-1) - f(n)A(n)\alpha(n). \tag{1.7}$$

The first term in Eq. 1.7 represents the rate at which embryos containing n molecules are formed by single molecule condensation on to a $(n-1)$ molecule-sized embryos with units of $volume^{-1} \times time^{-1}$. The second term is the rate at which n-sized are destroyed by single molecule evaporation. $f(n)$ and $f(n-1)$ are the actual embryos concentrations containing n and $n-1$ molecules, and $A(n)$ and $A(n-1)$ are the surface areas of n, and $n-1$ molecule

embryos respectively. $\beta(n-1)$ is the flux per unit time and area of single molecule condensation onto a $n-1$ molecule embryo and $\alpha(n)$ is the flux of single molecule evaporation from a n molecule embryo.

Good estimates of β can be obtained from the kinetic theory of gases, but generally, α is not known. However, α can be found by assuming an equilibrium distribution of embryos and using microscopic reversibility. Setting $J(n) = 0$, then assuming detailed balance between condensation and evaporation gives,

$$N(n-1)A(n-1)\beta = N(n)A(n)\alpha, \tag{1.8}$$

where $N(n-1)$ and $N(n)$ are the equilibrium concentrations of the embryos. Assuming single molecule fluxes are independent of embryo size and that they do not change during the equilibrium change, solving Eq. 1.8 for α yields

$$\alpha = \frac{N(n-1)A(n-1)\beta}{N(n)A(n)}. \tag{1.9}$$

Substituting the result into Eq. 1.7 gives

$$J(n) = N(n-1)A(n-1)\beta\left[\frac{f(n-1)}{N(n-1)} - \frac{f(n)}{N(n)}\right]. \tag{1.10}$$

Assuming a steady state where J becomes independent of n where droplet growth rates and decay rates are equal, we can write Eq. 1.10 as,

$$\frac{J}{\beta A(n-1)N(n-1)} = \frac{f(n-1)}{N(n-1)} - \frac{f(n)}{N(n)}. \tag{1.11}$$

Then summing from $n = 2$ to $n = \Lambda$, where Λ is a large number, we write Eq. 1.11 many times and sum, therefore the intermediate terms cancel, and then Eq. 1.11 becomes

$$J = \frac{\frac{f(1)}{N(1)} - \frac{f(\Lambda+1)}{N(\Lambda+1)}}{\sum_{n=1}^{\Lambda} \frac{1}{\beta A(n)N(n)}}. \tag{1.12}$$

Eq. 1.12 shows that J can be calculated using the equilibrium droplet distribution $N(n)$, β and ratio of actual to equilibrium concentrations of single molecule embryos and of large size embryos. For sufficiently large n, $f(n)$ will vanish and Eq. 1.12 becomes,

$$J = \frac{1}{\sum_{n=1}^{\Lambda} \frac{1}{\beta A(n)N(n)}}. \tag{1.13}$$

The minimum work to form an n-molecule embryo is related to $N(n)$, and its details will be given later in this section. This work can be written as

$$\Delta F = \gamma A + (P - P^{'})V^{'} + n(\mu^{'}(T, P^{'}) - \mu(T, P)), \tag{1.14}$$

where γ is the interfacial surface tension, A is the interfacial area between the embryo and the bulk phase, P is the bulk pressure , $P^{'}$ is the pressure inside the embryo and $V^{'}$ is the volume of the embryo. μ and $\mu^{'}$ are the chemical potentials of the bulk and the embryo, respectively.

Using the capillarity assumptions of uniform bulk densities for both phases, a sharp interface characterized by the bulk, planar surface tension and assuming the incompressibility of the embryo, we can write,

$$\mu^{'}(T, P^{'}) - \mu^{'}(T, P) = v^{'}(P^{'} - P), \tag{1.15}$$

and

$$\Delta F = \gamma A + n[\mu^{'}(T, P) - \mu(T, P)] = \gamma A + n\Delta\mu. \tag{1.16}$$

Since the surface area is proportional to $n^{2/3}$, we can write the phenomenological expression for the work of forming an n-sized embryo of the new phase in CNT as,

$$\Delta F(n) = n\Delta\mu + an^{2/3}, \tag{1.17}$$

where $\Delta\mu$ is the difference in chemical potential between the bulk stable and metastable phases and a is a geometric constant that is dependent on the shape of the embryo and proportional to the interfacial surface tension.

The first term in Eq. 1.17 represents the free energy gained by moving molecules from the metastable mother phase to the more stable phase and is negative, while the positive, second term accounts for the free energy cost of introducing an interface between the two phases. The functional form of Eq. 1.17 highlights the activated nature of the nucleation process and shows that embryos must overcome a free energy barrier, $\Delta F(n^*)$, associated with making a critical cluster of size n^*, before they can grow spontaneously into the new phase as shown in the Fig. 1.3 . The critical barrier height is obtained from $\partial F(n)/\partial n = 0$.

The simplest phenomenological model used in CNT to describe the condensation of a supersaturated vapour, which involves the capillarity assumptions of uniform bulk densities for both phases and a sharp interface characterized by the bulk, planar surface tension, gives the critical barrier and critical cluster size for the homogeneous nucleation as

$$\Delta F_{hom}(n^*) = \frac{16\pi}{3}\frac{v_l^2\gamma_{vl}^3}{(kT\ln S)^2}, \tag{1.18}$$

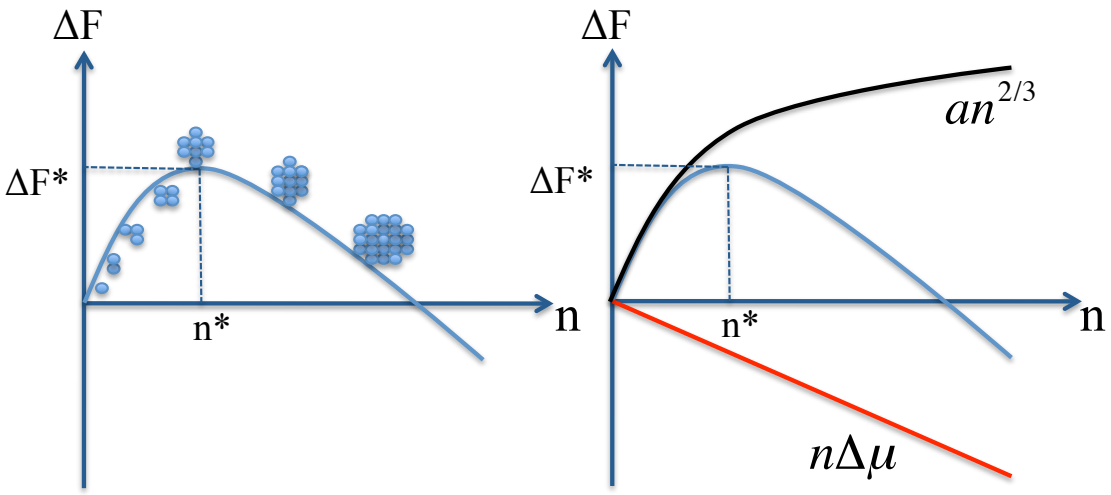

Figure 1.3: Work of forming an embryo.

and

$$n^* = \frac{32\pi}{3}\frac{v_l^2\gamma_{vl}^3}{(kT\ln S)^3}, \tag{1.19}$$

$$r^* = \frac{2v_l\gamma_{vl}}{(kT\ln S)}, \tag{1.20}$$

respectively. Here, r^* is the radius of the critical cluster, v_l is the volume per molecule in the bulk liquid phase, S is the supersaturation and we have used $\Delta\mu \approx kT\ln S$ as well as assuming that the nucleus is spherical in shape.

The rate J depends on $N(n)$ as shown previously, and the minimum work to form an n-molecule embryo is also related to $N(n)$ by assuming an equilibrium embryo distribution,

$$N(n) \propto exp[-\frac{\Delta F(n)}{kT}], \tag{1.21}$$

and

$$N(n) = N_{tot}exp[-\frac{\Delta F(n)}{kT}], \tag{1.22}$$

where N_{tot} is the total number density of the bulk metastable phase.

We can write the homogeneous nucleation rate by substituting Eq. 1.22 into Eq. 1.13 and using integration instead of summation yields,

$$J = \beta N_{tot}[\int_{n\ll n^*}^{n\gg n^*} exp[\frac{\Delta F(n)}{kT}]\frac{1}{A(n)}dn]^{-1}. \tag{1.23}$$

Expanding the work of embryo formation,

$$F(n) \approx F(n^*) + \frac{1}{2}F''(n^*)(n-n^*)^2 = F(n^*) + \frac{1}{2}F''(n^*)(\delta n)^2, \tag{1.24}$$

and substituting this into Eq. 1.23 gives

$$J = \{\beta A(n)\}\,[\sqrt{\frac{-\Delta F''(n^*))}{2\pi kT}}]\left\{N_{tot} exp[-\frac{\Delta F(n^*)}{kT}]\right\} = j(n^*)ZN(n^*), \tag{1.25}$$

where $j(n^*)$ is β times the surface area of the critical nucleus, $N(n^*)$ is the equilibrium concentration of critical nuclei, $\Delta F''(n^*)$ represents the second derivative with respect to n and Z is the Zeldovich factor.

The key point of this derivation is the transformation of a kinetic quantity, the rate, into an equation that has the two parts, a kinetic coefficient multiplied by an equilibrium, thermodynamic quantity, namely the equilibrium number of critically sized droplets. It is equally important to note that this equilibrium number is related to the thermodynamic work of forming a critical cluster and that this quantity is the main focus of most theoretical approaches to nucleation.

1.1.3 Heterogeneous Nucleation

In the presence of a macroscopic surface, nucleation can occur via a heterogeneous process. For example, when a supersaturated vapour is in contact with a solid wall, the nuclei of the stable liquid phase form at the solid-vapour interface. Droplets also form on particles of dust in the atmosphere so heterogeneous nucleation plays a particularly important role in understanding cloud physics.

The presence of the heterogeneous interface generally lowers the free energy barrier to nucleation relative to the homogeneous case, making it the dominant mechanism for a phase change in most practical situations. Consider the formation of a droplet contacting the wall as shown in Fig. 1.4. The nucleus then forms a droplet, contacting the wall with an angle, θ, that is characteristic the interaction of the material with the wall and is related to the wall-liquid (γ_{wl}) and wall-vapour (γ_{wv}) surface tensions through Young's equation [4, 10, 11, 12],

$$\gamma_{vl}\cos\theta = \gamma_{wv} - \gamma_{wl}. \tag{1.26}$$

The minimum work for the formation of the droplet is

$$\Delta F = \gamma_{vl}A_{vl} + (\gamma_{wv} - \gamma_{wl})A_{wl} + (P - P^{'})V^{'} + n(\mu^{'}(T, P^{'}) - \mu(T, P)). \tag{1.27}$$

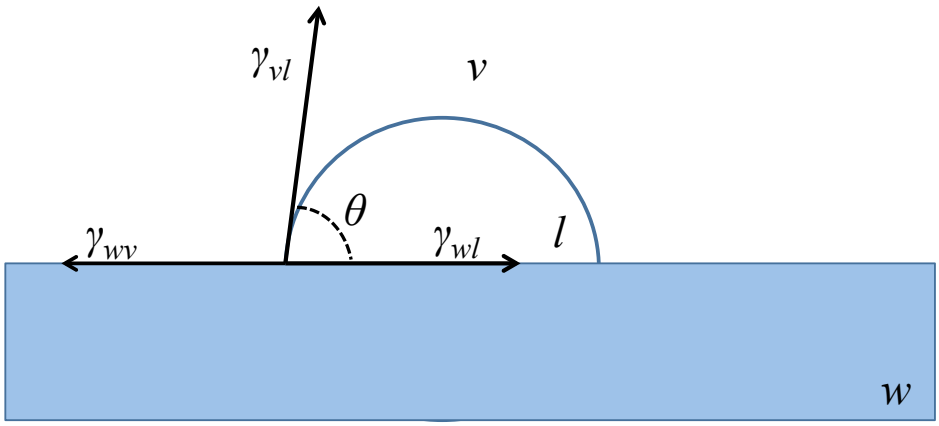

Figure 1.4: Formation of liquid drop on solid surface from a saturated vapour. w, l and v represent wall, liquid and the vapour. θ is the contact angle.

Taking the radius of curvature of the liquid-vapour interface as r, the volume of spherical cap, V_{sc} can be given as

$$V_{sc} = \frac{\pi r^3(2 - 3cos\theta + cos^3\theta)}{3}. \tag{1.28}$$

The liquid-vapour interface area and liquid-wall area can be expressed as $2\pi r^2(1 - cos\theta)$ and $\pi r^2 sin^2\theta$, respectively.

Using Eq. 1.27, Eq. 1.28 with the interface areas, the minimum work for the critical nucleus in heterogeneous nucleation can be written as

$$\Delta F_{het}(n^*) = \frac{16\pi}{3}\frac{v_l^2\gamma_{vl}^3}{(\Delta\mu)^2}\frac{(1 - cos\theta)^2(2 + cos\theta)}{4}. \tag{1.29}$$

Eq. 1.29 can also be written in the form

$$\Delta F_{het}(n^*) = f(\theta)\Delta F_{hom}(n^*), \tag{1.30}$$

where $f(\theta) = \frac{(1-cos\theta)^2(2+cos\theta)}{4}$ and $0 \leq f(\theta) \leq 1$ is solely a function of the contact angle. Eq 1.30 shows that the barrier is always reduced because the wall contributes a portion of the interfacial free energy. In the limit where the contact angle goes to π, the liquid is non-wetting and $f(\theta)$ tends to one. Nucleation then occurs homogeneously in the bulk. If the liquid and surface are highly attractive so the liquid completely wets the wall, $\theta \to 0$ and $f(\theta) \to 0$, causing the barrier to go to zero. Despite the extremely simplified approach involved in CNT, recent simulation studies of heterogeneous nucleation in hard spheres colloids [13, 14, 15] and

the Ising model [16] have shown that Eq. 1.30 is generally correct, as long as an additional term involving the three-phase contact line tension is included in $\Delta F(n)$.

CNT also suggests that as the heterogeneity becomes more microscopic its ability to activate nucleation is greatly reduced [17]. Scheifele [18] and coworkers studied heterogeneous nucleation induced by a small impurity consisting of a line of l fixed spins and evaluated the free energy barrier on approach to the limit of stability of the metastable phase.

They showed that to find the free energy barrier correctly for microscopic systems, it is important to identify the appropriate thermodynamic reference state. This free energy barrier is the minimum reversible work required to apply a constraint that confines the system to the transition state at $n = n^*$ and the reference state is the entire configuration space of the metastable phase such as all the configurations between $l \leq n \leq n^*$. Therefore, the work of formation of n-size cluster, starting from the equilibrium metastable phase, is given by,

$$G(n) - G_m = -kT \ln \frac{P(n)}{\sum_{n'=l}^{n^*} P(n')}, \tag{1.31}$$

where G_m is the free energy of the metastable phase and $\sum_{n'=l}^{n^*} P(n')$ is the sum of all probabilities such that $l \leq n \leq n^*$.

An interesting consequence of this normalization of the probabilities is that the barrier height does not tend to zero at the point where the system reaches its limit of stability. Features of this analysis will be studied further in Chapter 3.

1.1.4 Heterogeneous Nucleation in Nature and Technology

Nanoscale systems demonstrate a variety of structures and phase transitions different from their bulk counterparts as a result of fluctuation of thermodynamic quantities, quantum mechanical and surface effects. For example, as the surface to volume ratio for an atomic cluster becomes very large, the thermodynamically stable cluster crystal structure can change dramatically, and for very small structure the icosahedral structure becomes the most stable [19]. The structure of these particles will affect the chemical properties of the systems. Therefore, studying nanoscale systems, understanding and controlling the properties of these systems, and how their behaviour differs from macroscopic objects is very important for our understanding of many natural processes as well as for nanotechnology.

Aerosols are small particles in suspension in the atmosphere in the solid phase or liquid phase. Aerosols originate both from natural and man-made (anthropogenic) sources. They

can be directly emitted as particles into the atmosphere by volcanoes, desert dust particles, from sea spray and from vegetation. They can also be the result of chemical reactions such as gas-to-particle conversion. It is estimated that 90% of the aerosols can be characterized as originating from natural sources on the global scale. Anthropogenic aerosols are those coming from the combustion of fossil fuel and biomass burning. Soluble organic and inorganic materials are major components of aerosols in the troposphere. For example, mineral acids like sulfuric acid or nitric acid, and soluble inorganic salts such as magnesium chloride, sodium chloride, sulfates, nitrates or other organic material. Aerosol particles have a broad range of phase, composition, size, and mixing characteristics and are an important component of the global climate through their interaction with atmospheric radiation and their influence on cloud properties, atmospheric stability, and chemistry [20, 21].

Deliquescence is the process in which a solid soluble aerosol takes water vapour up from the atmosphere to form a solution droplet and efflorescence is the process in which the solution loses water to form a crystal. Fig. 1.5 illustrates the deliquescence and efflorescence of a soluble aerosol occurring in the atmosphere. At low relative humidity (RH) the aerosol particle is solid. As the relative humidity increases, the particle remains solid until the deliquescence threshold (DRH) is reached, at which the aerosol particle absorbs water vapour from the atmosphere to form a solution droplet. When the dry particle is large, i.e., micron sized, deliquescence occurs at a well defined RH, and the transition is sharp. Once the drop is formed, its size as a function of RH varies according to the Kelvin relation.

If we look at the reverse process, the solution droplet starts to lose water as the RH decreases. However, the system does not retrace the path followed with increasing RH. When it reaches a threshold RH, which is lower than the DRH, the solution droplet nucleates a crystal and the water evaporates. This process is called efflorescence and the threshold humidity as the efflorescence RH (ERH).

Deliquescence is best described in terms of Kölher activation for large particles, and nucleation only becomes important when the size of the dry particle becomes small. Efflorescence is a nucleation process for all particle sizes.

One of the theories for the deliquescence of small particles investigates the effect of surface phenomena on the deliquescence process. The theory is applied to a generic crystal with properties similar to NaCl, in water vapour, and it is found that the surface tension has a

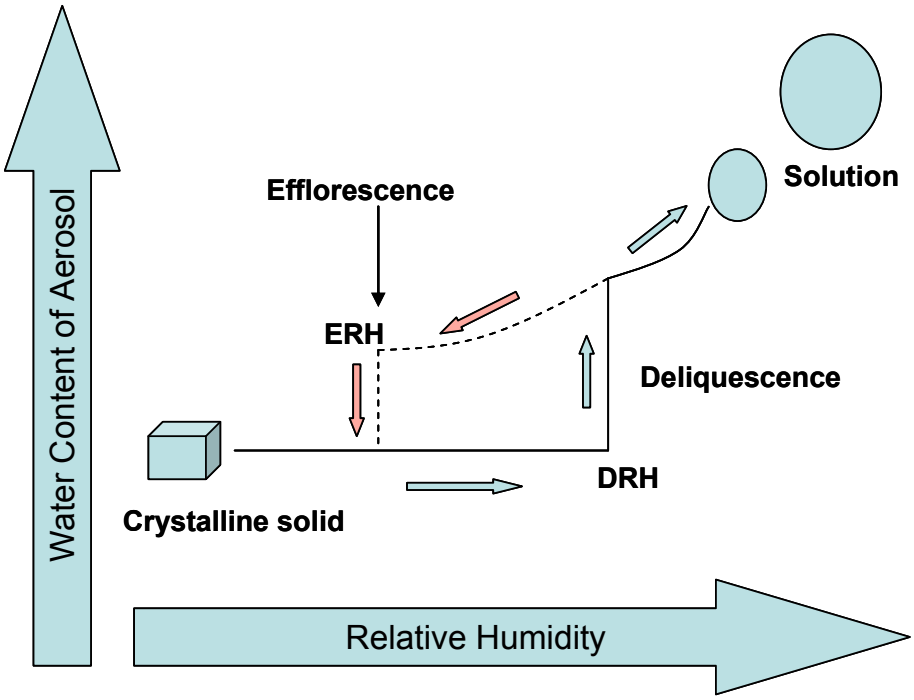

Figure 1.5: Deliquescence and efflorescence process.

significant effect for crystals with a radius smaller than 0.1 μm. For very small systems, the surface tension produces an increase in the pressure required for a crystal of fixed size to deliquesce and as the crystal becomes larger this effect disappears [22].

Wise at al. [23] measured the DRH and ERH, and studied the hygroscopic behaviour, of 0.1 to 4 μm sized particles of NaBr, CsCl, NaCl, $(NH_4)_2SO_4$, and KBr using an environmental transmission electron microscopy (ETEM). They also investigated the morphology changes that these particles undergo as the RH is cycled and showed that differences in electron dose rate, particle size (within bounds), and sample substrate have no effect on phase transitions measured by the ETEM.

Biskos et al. [24] used a tandem nano-differential mobility analyzer to show that the DRH of NaCl nanoparticles, with dry mobility diameters of 6 to 60 nm increased as the particle size decreased. The observations indicate that the hygroscopic growth of NaCl nanoparticles decreases with decreasing particle size. For example, the hygroscopic growth factor of 6 nm particles at 80% RH is approximately 1.55 compared to 1.75 for 60 nm particles. Furthermore, the DRH values increase as the particle gets smaller [24, 25, 26].

Literature reports differ on the possibilities of discontinuous and continuous (i.e., prompt and nonprompt) deliquescence of aerosol particles in the nanosize regime. Hameri et al. [27]

found that particles smaller than 15 nm have nonpromt deliquescence and efflorescence as indicated by the presence what appears to be partially dissolved particle. They suggested the nonpromptness of particle deliquescence and efflorescence occurs because of the presence of hygroscopic impurities in the nanoparticles. However, experiments reported by Biskos et al. demonstrate prompt deliquescence and efflorescence of ammonium sulfate and NaCl particles having diameters from 6 to 60 nm.

The hygroscopic growth can depend of a particle property on size. It is found that the liquid-vapour surface tension γ_{lv} of liquid droplets below a threshold size decreases monotonically with the size of the droplet in the nanometer region. This threshold size is estimated to be around 2 nm, but this has not been tested and could start at larger sizes. Atmospheric aerosol particles are often nonspherical and the shape factor of nonspherical particles is expected to become size dependent below the threshold sizes .

Biskos et al. [24] also developed four models to test how well existing models predict the observations. For particles larger than 8 nm, the measurements agree best with the thermodynamic model, includes the Kelvin effect, to account for the enhanced vapour pressures of small particles due to curvature effects, and a size-dependent shape factor . For 6 nm particles, the smallest size studied, the experiments deviate significantly from the predictions of the model. In addition to nanosize effects, contamination of the nanoparticles has an important effect on deliquescence and efflorescence results.

McGraw [28] investigated size-dependent deliquescence/efflorescence phase transformation for particles down to several nanometers in size. They consider a spherical salt particle covered with a thin layer of solution. They developed a phenomenological model, called the thin layer model, that focuses on the equality of chemical potentials between the phases in each component, i.e., the equality of the chemical potential of the salt in the core and the thin film of the solution, and the equality of chemical potentials of the water in the film and vapour phase. They found that the deliquescence of nanometer sized particles occurs at a relative humidity just below the deliquescence relative humidity of crossing a nucleation barrier.

Zasetsky [29] studied the dissolution of small crystalline NaCl particles with defects in a highly supersaturated water vapour using molecular dynamics simulations. Their system was composed of 512 NaCl particles and 8096 water molecules. They introduced a number

of defects to a perfect crystal which allowed them to simulate the initial stages of the solid to liquid transition on the scale of sizes and times accessible by MD. They showed that the crystal lattice does not breakdown unless the thickness of the water layer over the salt particles exceeds several molecular layers and there are about 10 to 12% defects in the crystal. They found that to see structural changes in the NaCl crystal, the amount of water required, which also depends the size of salt particles and the number of defects, is approximately half of the crystal size.

Mirabel et al. [30] have compared the Köhler theory of activation with classical nucleation theory for the NaCl-H_2O system, and found that for NaCl particles of the size typically found in the atmosphere, the two processes are hardly distinguishable. The Köhler theory of activation makes use of interfacial thermodynamics and in particular the Kelvin relation, to describe the formation and growth of soluble, involatile heterogeneous condensation nuclei. Here, the Kelvin relation in simple form is given by,

$$\frac{P}{P_\infty^0} = \exp\left\{\frac{2\gamma v_1}{rkT}\right\}, \tag{1.32}$$

where P is the vapour pressure of a spherical drop of radius r at temperature T. γ is the surface tension independent of r, P_∞^0 is the vapour pressure of a bulk liquid, k is the Boltzman constant and v_1 is the volume per molecule of liquid. Activation occurs when the height of the free energy barrier is reduced by increasing the pressure, to the point where the droplet is in unstable equilibrium and will grow spontaneously. Mirabel et al. also found that for very small NaCl crystals (10-50 molecules) nucleation can occur at relative humidities significantly lower than those required for activation.

Djikaev et al. [31] have developed a theory for the deliquescence of soluble crystals. The theory considers interfacial effects and is applicable to nanoscale systems. The thermodynamic theory is simple, at the level of the capillarity approximation frequently used in nucleation theory, and includes the effects of disjoining pressure. The initial stage of formation of a droplet on a soluble particle is that the particle gradually dissolves so that a liquid film of aqueous solution forms around it. Then this system is completely dissolved. However in this theory, the soluble aerosols do not deliquesce promptly and transition occurs over a range of supersaturations, unlike experimental results.

Oxtoby and Talanquer [32] have used density functional theory to study the structural and thermodynamic properties of droplets formed on soluble and partially soluble particles

composed of a fluid with an extremely low volatility. They consider cases in which the two components are fully or partially miscible and analyze the structure and stability of droplets formed at various supersaturations. They identify a solubility transition in partially miscible mixtures at which the soluble particle dissolves spontaneously at a well defined value of the supersaturation. The relative change in the droplets size at the transition is greater for the smaller particles. The solubility transition is similar with the deliquescence process of water soluble salts. Comparisons of their results with the predictions of Köhler theory of activation show that the capillarity approximation describes surprisingly well the properties of very large droplets of ideal and non-ideal mixtures, but overestimates the vapour pressure of the droplets, particularly in small systems. This research is the only molecular level treatment of a deliquescence like process to date.

The small systems exhibit these unusual behaviours in the deliquescence and efflorescence experiments due to a variety of physical phenomena such as:

- particle size,
- particle shape,
- surface effects,
- contamination of the particles by other species.

1.2 Nucleation Studies Using Molecular Simulations

1.2.1 Molecular Dynamics Simulations

Molecular dynamics (MD) simulation is a commonly used tool in many fields of science and technology such as materials science, and atmospheric science for modeling solids, liquids and gases at the atomic level. The molecular dynamics method was first introduced by Alder and Wainwright [33] in 1957 to study relaxation accompanying various nonequilibrium phenomena using hard spheres with event driven simulation. In the hard sphere model, particles can be thought of as billiard balls and they obey the laws of elastic collision. There is excluded volume interaction between them, spheres travel in straight lines, and there are no forces acting on the particles between collisions. The behaviour of simple liquids is understood from their studies such as fluid solid phase transitions. In 1964, Rahman [34] used

a realistic potential for liquid argon in his MD simulations at Argonne National Laboratory. The system was composed of 864 particles interacting with a Lennard-Jones potential at 94.4 °K and found the self diffusion constant and pair correlation function agree well with experiment. Rahman and Stilinger [35, 36] simulated the liquid water system. They showed that the effect of pressure increase was to raise fluidity in a system of 216 water molecules.

Simulation techniques have greatly improved with increasing computing power, and many specialized techniques can now be found for particular problems, including the mixed quantum mechanical - classical simulations [37]. MD plays very important role in the analysis of the behaviour of materials at an atomistic level that can not be obtained by experiments.

MD represents a deterministic technique that follows the time evolution of a system consisting of interacting particles. In general, MD simulation is the numerical solution of Newton's equations of motion for an ensemble of atoms where they are integrated using several methods for a short time step, typically 1 fs [37, 38, 39].

Equations of Motion

Newton's equation of motion, for a system of interacting particles is given by,

$$m\frac{d^2\mathbf{r}_i}{dt^2} = \frac{d(m_i\mathbf{v}_i)}{dt} = \mathbf{F}_i, \tag{1.33}$$

where m_i is the mass of the particle and $\mathbf{r}_i$, $\mathbf{v}_i$ and $\mathbf{F}_i$ are the position, velocity and force exerted on the particle, respectively. Given the position $\mathbf{r}_i$ and velocity $\mathbf{v}_i$ of each particle in the system at the time t_0 , the subsequent position $\mathbf{r}_i(t_0 + \delta t)$ and velocity $\mathbf{v}_i(t_0 + \delta t)$ of a particle is calculated by using a scheme like that described in Fig. 1.6.

The force acting on the ith atom at a given time can be obtained from the inter atomic potential $V(\mathbf{r}_1, \mathbf{r}_2, \mathbf{r}_3, ..., \mathbf{r}_N)$ that, in general, is a function of the positions of all the atoms

$$\mathbf{F}_i = - \bigtriangledown_i V(\mathbf{r}_1, \mathbf{r}_2, \mathbf{r}_3, ..., \mathbf{r}_N), \tag{1.34}$$

where N is the number of atoms and $\bigtriangledown$ is the gradient. The gradient of a function, $f(x, y, z)$, in a three dimensional Cartesian coordinate system is given by

$$\bigtriangledown f = \frac{\partial f}{\partial x}\vec{i} + \frac{\partial f}{\partial y}\vec{j} + \frac{\partial f}{\partial x}\vec{k}. \tag{1.35}$$

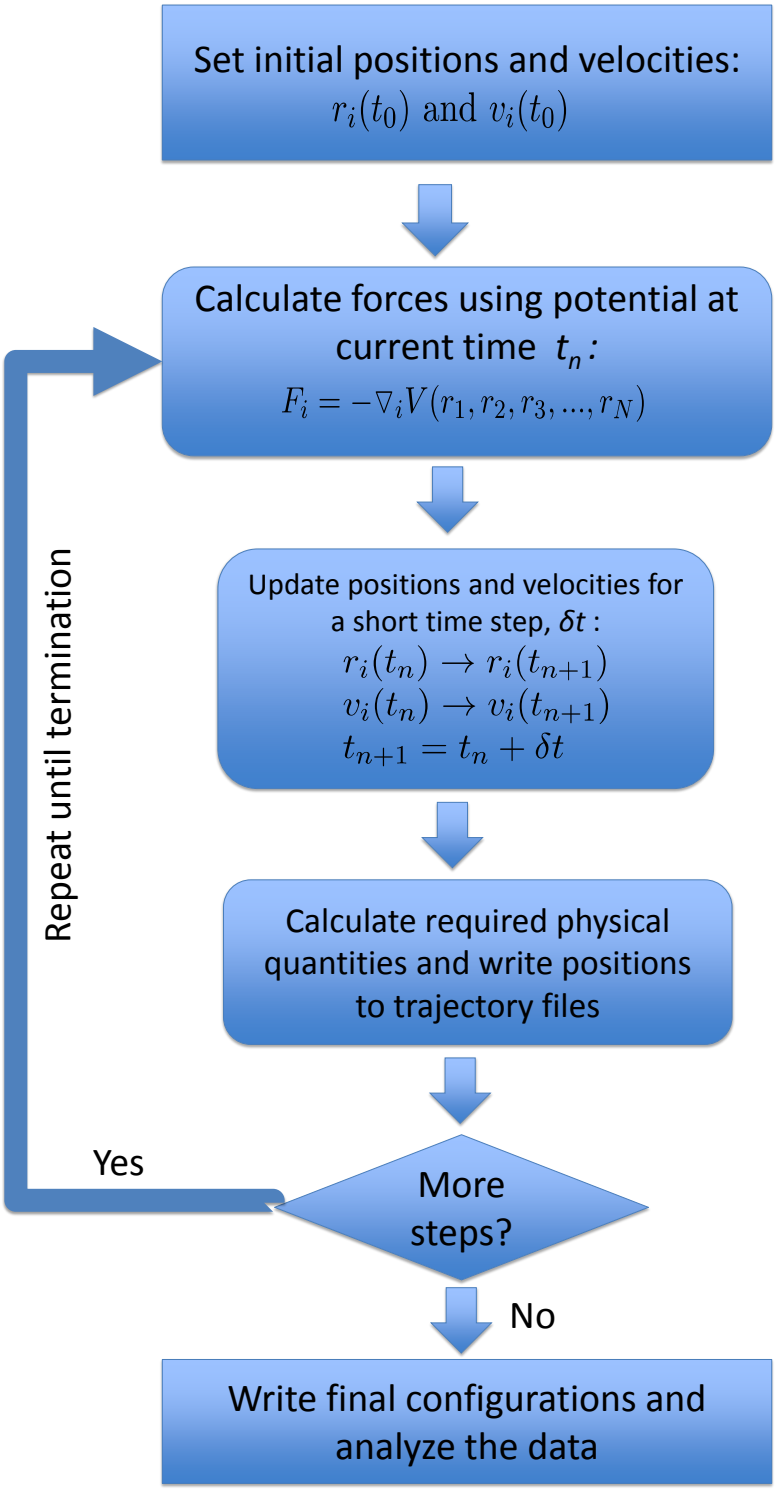

Figure 1.6: A flow chart for a basic MD code.

Once the initial conditions and the interaction potential are defined, the equations of motion can be solved numerically. The results of the solution are the positions, $\mathbf{r}_i(t)$, and velocities, $\mathbf{v}_i(t)$, of all the atoms as a function of time.

Integration Algorithms

Many numerical algorithms, such as Verlet algorithm, leap-frog algorithm and predictor-corrector algorithm have been developed to integrate the equations of motion in MD simulations. In choosing which algorithm to use, four important rules should be considered: (1) the algorithm should conserve energy and momentum; (2) it should be computationally efficient, (3) it should permit a long time step for integration; (4) it should be simple in form and easy to program [37].

In all integration algorithms the positions, velocities and accelerations can be approximated by a Taylor series expansion about time t:

$$\mathbf{r}(t+\delta t) = \mathbf{r}(t) + \mathbf{v}(t)\delta t + \frac{1}{2}\mathbf{a}(t)\delta t^2 + \frac{1}{6}\mathbf{b}(t)\delta t^3 + ..., \tag{1.36}$$

$$\mathbf{v}(t+\delta t) = \mathbf{v}(t) + \mathbf{a}(t)\delta t + \frac{1}{2}\mathbf{b}(t)\delta t^2 + ..., \tag{1.37}$$

$$\mathbf{a}(t+\delta t) = \mathbf{a}(t) + \mathbf{b}(t)\delta t + ..., \tag{1.38}$$

$$\mathbf{b}(t+\delta t) = \mathbf{b}(t) + ..., \tag{1.39}$$

where $\mathbf{a} = \frac{\mathrm{d}^2\mathbf{r}}{\mathrm{d}t^2}$ is the acceleration, and $\mathbf{b} = \frac{\mathrm{d}^3\mathbf{r}}{\mathrm{d}t^3}$ is the third time derivative of the $\mathbf{r}$.

The Verlet algorithm[41] uses positions and accelerations at time t and the positions from time $t - \delta t$ to calculate new positions at time $t + \delta t$. The Verlet algorithm uses no explicit velocities.

To derive the Verlet algorithm one can write,

$$\mathbf{r}(t+\delta t) = \mathbf{r}(t) + \mathbf{v}(t)\delta t + \frac{1}{2}\mathbf{a}(t)\delta t^2, \tag{1.40}$$

and

$$\mathbf{r}(t-\delta t) = \mathbf{r}(t) - \mathbf{v}(t)\delta t + \frac{1}{2}\mathbf{a}(t)\delta t^2. \tag{1.41}$$

Summing these two equations gives,

$$\mathbf{r}(t+\delta t) = 2\mathbf{r}(t) - \mathbf{r}(t-\delta t) + \mathbf{a}(t)\delta t^2, \tag{1.42}$$

The velocities can then be calculated by the formula,

$$\mathbf{v}(t) = \frac{\mathbf{r}(t+\delta t) - \mathbf{r}(t-\delta t)}{2\delta t}. \tag{1.43}$$

The leap-frog algorithm is a modified version of the Verlet algorithm to obtain more accurate velocities [38]. The positions and velocities at a half time step are given by

$$\mathbf{r}(t+\delta t) = \mathbf{r}(t) + \mathbf{v}(t+\frac{1}{2}\delta t)\delta t, \tag{1.44}$$

$$\mathbf{v}(t+\frac{1}{2}\delta t) = \mathbf{v}(t-\frac{1}{2}\delta t) + \mathbf{a}(t)\delta t. \tag{1.45}$$

The leapfrog algorithm is computationally less expensive and requires less storage. This is an important advantage in the case of large scale calculations. The main drawback of this method is that the velocities and positions are not defined at the same time, making it difficult to obtain potential and kinetic energies [65].

Intermolecular Potential

The choice of the appropriate potential energy affects how closely our simulation reproduces the properties of a real system. Therefore, the potential energy is very important and plays a major role in MD simulations. There are different potentials that are developed for different classes of materials due to the different interacting forces. For example, for a pair of atoms i and j, the Lennard-Jones potential function is given by [40],

$$V(\mathbf{r}_{ij}) = 4\epsilon_{ij}\left[(\sigma_{ij}/\mathbf{r}_{ij})^{12} - (\sigma_{ij}/\mathbf{r}_{ij})^{6}\right], \tag{1.46}$$

where ϵ_{ij} and σ_{ij} represent the energy and length interaction parameters.

Periodic Boundary Conditions

A system constructed using periodic boundary conditions (PBC) may be used to relate the properties of the small system to those of the real one. The introduction of periodic boundaries is equivalent to considering an infinite, space-filling array of identical copies of the simulation region. Fig. 1.7 shows a two dimensional view of a simulation cell, here, using

PBC, when an atom a leaves the central box, its images in the neighbouring boxes move in a similar fashion. For example, a simulation box from our simulation is shown in Fig. 1.8 (left) and PBC is at right for the same system.

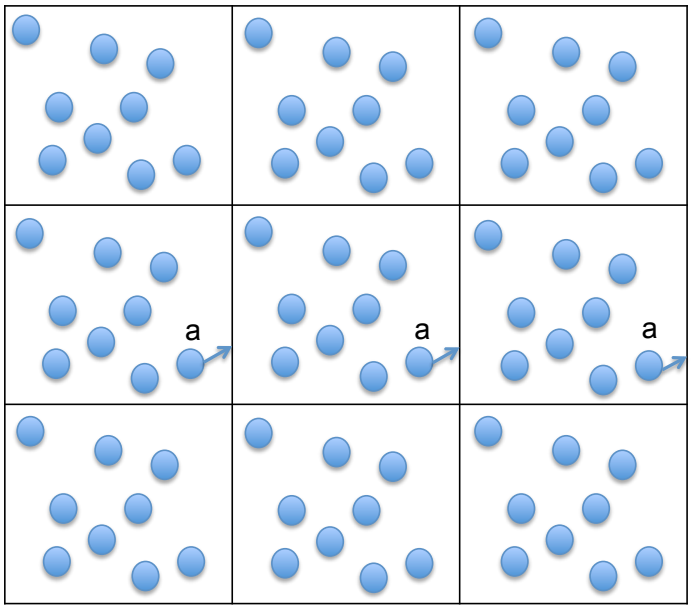

Figure 1.7: Two dimensional view of a MD simulations cell using periodic boundary conditions.

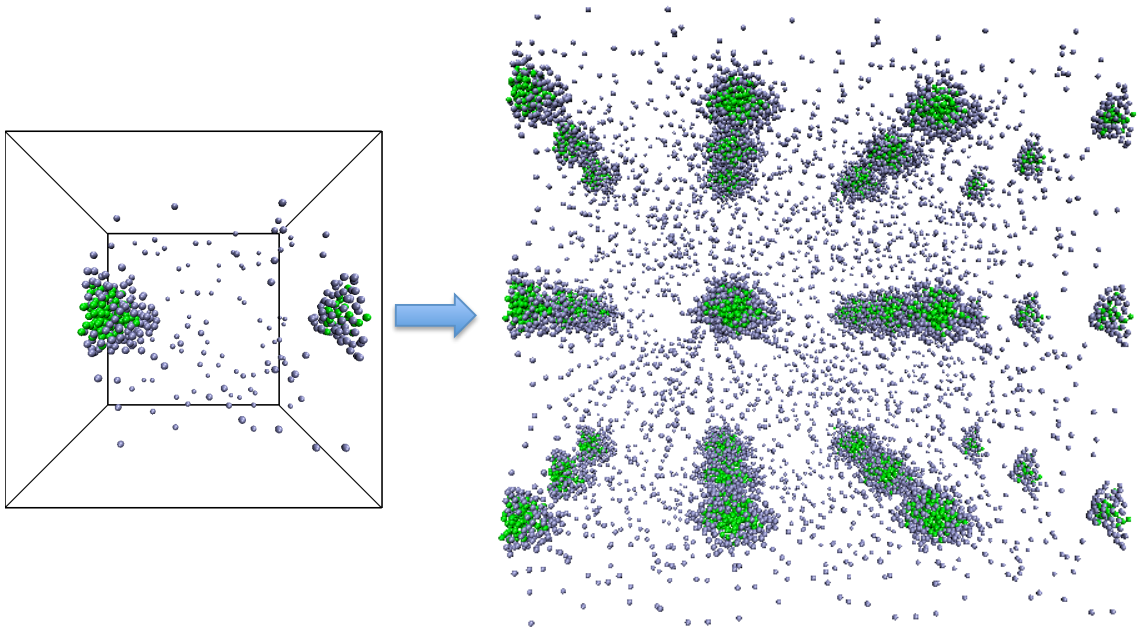

Figure 1.8: Three dimensional view of one of our MD simulation (left) and applying periodic boundary conditions (right).

The system is made infinite in extent using periodic boundary conditions. In particular, the minimum image convention dictates that each atom i in the cell interacts with the closest image of all atoms j. Therefore, the minimum image convention must be taken into account in both the integration of the equations and the interaction potentials. After each integration step, if an atom is found to have moved outside the region its coordinates must be adjusted to bring it back inside. The interaction potentials have an infinite range. In practical applications, it is customary to establish a cutoff radius r_c and disregard the interactions between atoms separated by more than r_c. This results in simpler programs and enormous savings of computer resources, because the number of atomic pairs separated by a distance r grows as r^2.

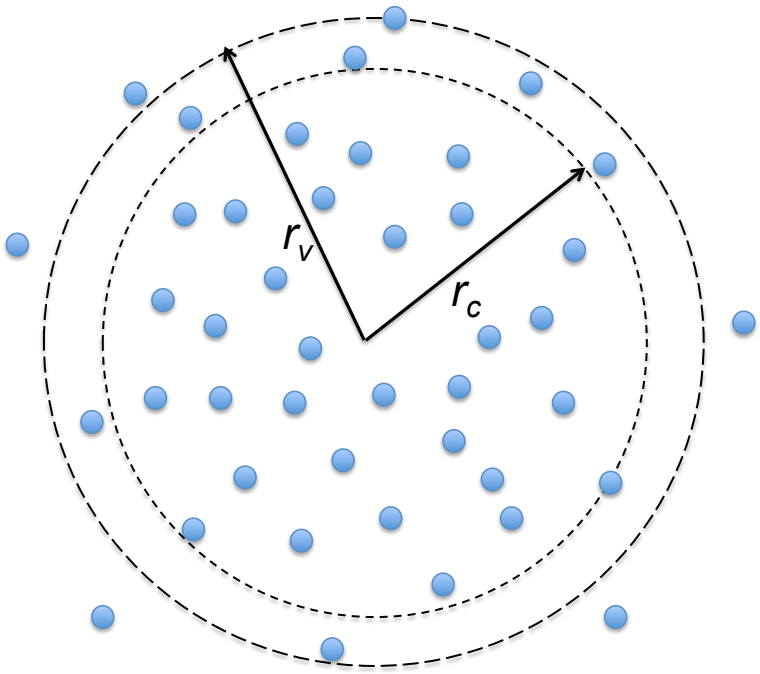

Figure 1.9: Illustration of Verlet neighbour list.

Verlet [41] suggested a method to improve the speed using a list of neighbours of a particular atom and this list is updated at intervals. This is depicted in Fig. 1.9 where r_c is the cutoff in the potential, and r_v is the cutoff in the Verlet neighbour list. As r_v is larger than the cutoff in the potential, it is only necessary to update this array periodically. When an atom has moved a distance of $0.5(r_v - r_c)$ then it is necessary to update the list.

Reduced Units

In the simulations, we express quantities such as temperature, density, pressure, and the like in reduced units. For this purpose, we chose the following basic units:

- Unit of length, σ
- Unit of energy, ϵ
- Unit of mass, m

Then, other physical quantities are expressed in reduced units in the following way: time, $t^* = \frac{t}{\sqrt{m\sigma^2/\epsilon}}$ length, $r^* = \frac{r}{\sigma}$ temperature, $T^* = \frac{k_B T}{\epsilon}$ density, $\rho^* = \rho\sigma^3$ pressure, $P^* = \frac{P}{\epsilon/\sigma^3}$. For example, values of the parameters can be used to translate reduced units to real units for Lennard-Jones argon:

- $\sigma = 3.405\ A^0$
- $\epsilon = 1.656 \times 10^{-21}$J
- $m = 6.693 \times 10^{-26}$ kg

In this thesis, molecular dynamics simulations are used to study the nucleation kinetics of vapour condensation in the presence of heterogeneities. In the next section, we we will give the details how to calculate nucleation rates from molecular dynamics simulations.

1.2.2 Mean First Passage Time Method

The mean first passage time (MFPT) is a new method used to analyze the kinetics of activated process in simulations that gives estimates of the nucleation rate, the size of the critical embryo and the free energy barrier. Reguera and his coworkers introduced this method in 2007 and applied it to the study of nucleation in rare gases [42]. They showed that its application to molecular dynamics simulations is straightforward and allows the precise determination of the rate. For each simulation, the largest clusters size and the time at which the n sized cluster appears for the first time, $t_i(n)$ is kept in the output data. Then the MFPT, $\tau(n)$, for each size n is calculated by averaging over 200 simulations. Wedekind [43] calculated nucleation rates of vapour-liquid nucleation of LJ argon from MD simulations using the MFPT technique, and they compared the results to classical nucleation theory

(CNT) and the modified liquid drop theory. They found that the rate results deviate by 2 to 7 orders of magnitude from CNT however the critical cluster sizes agree well with CNT. Reguera [44] used this technique in the simulation of nucleation of a Lennard-Jones argon vapour and reconstruct the free energy landscape directly from the non-equilibrium kinetics of this system. Julin [45] used molecular dynamics simulations to study cluster-vapour equilibrium of a simple LJ argon system and investigated the dependence of critical cluster size in the range of 20-300 atoms on the vapour density and compared the results with Monte Carlo simulations, density functional theory and square gradient theory. They found out that the MD results agree well with density functional and square gradient theory calculations however, critical sizes and free energies are higher than the Monte Carlo simulation results.

Here we explain the theory behind MFPT. The dynamics of many nonequilibrium processes can be described by a Fokker-Plank equation [46]

$$\frac{\partial P(x,t)}{\partial t} = \frac{\partial}{\partial x}\left(D(x) e^{-\beta \Delta G(x)} \frac{\partial}{\partial x} P(x,t) e^{\beta \Delta G(x)} \right) = -\frac{\partial J(x,t)}{\partial x}, \tag{1.47}$$

where x is the reaction coordinate that describes the state of the system. In nucleation, the size of the largest cluster is usually used as the reaction coordinate. $P(x,t)$ is the probability distribution function, $J(x,t)$ is the flux, $D(x)$ is a generalized diffusion coefficient, $\Delta G(x)$ is the free-energy, and $\beta = 1/k_B T$ where T is the temperature and k_B is the Boltzmann's constant.

For an activated process involving a high barrier, the system reaches a steady state with a time-independent probability distribution $P_{st}(x)$ given by

$$\frac{\partial P_{st}(x)}{\partial t} = 0. \tag{1.48}$$

The reaction rate, J, is then given by

$$J = -D(x) e^{-\beta \Delta G(x)} \frac{\partial}{\partial x} P_{st}(x) e^{\beta \Delta G(x)}. \tag{1.49}$$

Since, from Eq. 1.47, $\partial P_{st}(x)/\partial t = \partial J/\partial x = 0$, we can write Eq. 1.49 as

$$\frac{\partial(\beta \Delta G(x))}{\partial x} = -\frac{\partial \ln P_{st}(x)}{\partial x} - \frac{J}{D(x) P_{st}(x)}. \tag{1.50}$$

Integration of this equation yields,

$$\beta \Delta G(x) = -\ln P_{st}(x) - J \int \frac{dx'}{D(x') P_{st}(x')} + C, \tag{1.51}$$

where C is the integration constant. At equilibrium, $J = 0$, and Eq. 1.50 becomes

$$\beta\Delta G(x) = -\ln P_{eq}(x), \tag{1.52}$$

which relates the equilibrium distribution, P_{eq}, with the free energy.

To reconstruct the free-energy landscape from the knowledge of $P_{st}(x)$, the mean first passage time, which is related to steady state rate as $J = 1/2\tau$, can be used,

$$\tau(x; x_0, a) = \int_{x_0}^{x} \frac{1}{D(y)} dy \; e^{(\beta\Delta G(y))} \int_{a}^{y} dz \; e^{(-\beta\Delta G(z))}, \tag{1.53}$$

where $\tau(x; x_0, a)$ is defined as the average time it takes for the system to reach the state x, having started at state x_0, when there are reflecting boundary conditions at a, and absorbing boundary conditions at x.

Taking the double derivative of Eq. 1.53 with respect to x, yields

$$\frac{\partial \ln(A(x)D(x))}{\partial x} = \frac{1}{A(x)D(x)} + \frac{\partial(\beta\Delta G(x))}{\partial x}, \tag{1.54}$$

where $A(x) = \partial\tau(x)/\partial x$. Integrating this equation allows one to reconstruct free energy;

$$\beta\Delta G(x) = \ln(B(x)) - \int \frac{dx'}{B(x')} + C, \tag{1.55}$$

where $B(x) = A(x)D(x)$.

Using Eq. 1.50 and Eq. 1.54 gives,

$$\frac{\partial(B(x)P_{st}(x))}{\partial x} = P_{st}(x) - JA(x). \tag{1.56}$$

Integration of this equation yields,

$$B(x) = -\frac{1}{P_{st}(x)} \left[\int_{x}^{b} P_{st}(x')dx' - \frac{\tau(b) - \tau(x)}{\tau(b)} \right]. \tag{1.57}$$

For example, if we use the reaction coordinate as the size of the cluster, n, the MFPT can be represented by [42],

$$\tau(n) = \frac{\tau_J}{2}[1 + erf((b - n^*)c)], \tag{1.58}$$

where n^* is the critical size, τ_J is the nucleation time, which is related to the steady state nucleation rate as $J = 1/\tau_J V$, c is associated with the Zeldovich factor, Z, as $c = \sqrt{\pi}Z$ and $erf(x) = 2/\sqrt{\pi}\int_0^x e^{-x^2}dx$ is the error function. For example, Fig 1.10 shows the application of Eq. 1.58 to our simulation data. Here the system has a total of 513 particles and has a

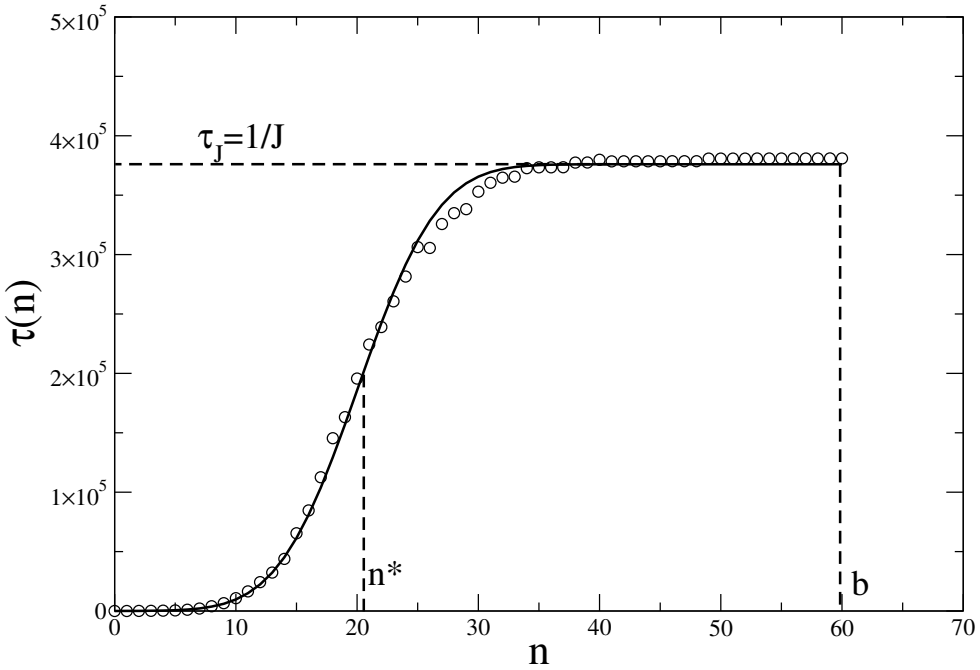

Figure 1.10: Illustration of the MFPT method. Circles are from simulations and line is the fit for Eq. 1.58.

supersaturation $S = 8.00$. The circles shows the data from 200 simulations and the solid line is the fitting to the data. This allowed us to extract J, n^* and c by using them as parameters in the fit of Eq. 1.58. For this particular system, the values are $n^* = 22$, $\tau_J = 3.91 \times 10^5$ and $J = 3.12 \times 10^{23}$ cm$^{-3}s^{-1}$.

The free energy barrier is given by [44],

$$\beta\Delta G(n) = \beta\Delta G(n_0) + \ln\left[\frac{B(n)}{B(n_0)}\right] - \int_{n_0}^{n} \frac{dn'}{B(n')}, \tag{1.59}$$

where

$$B(n) = -\frac{1}{P_{st}(n)}\left[\int_n^b P_{st}(n')dn' - \frac{\tau(b) - \tau(n)}{\tau(b)}\right]. \tag{1.60}$$

Here, b is the upper absorbing boundary, while $n_0 = 0$ represents the lower reflecting boundary and the reference state. $P_{st}(n)$ is the steady state probability that the largest cluster in a given configuration from the ensemble of runs is of size n.

There are many different methods to calculate nucleation rates from molecular dynamics simulations other than MFPT such as the direct observation method (DOM) [47], Yasuoka-Matsumoto method (YM) [48] and survival probability (SP) [49]. DOM uses the time the first cluster exceeds a predefined threshold size n_t in the system. Since the critical size at the maximum of the free energy barrier is not known a priori and the predefined threshold

size is an arbitrary parameter, they influence the onset times and hence the nucleation rate results. The Yasuoka-Matsumoto method uses the growth-decay dynamics of clusters to calculate nucleation rates. This method also depends on the chosen threshold cluster size and is generally applied to large systems to achieve good statistics. The MFPT method is parameter free and easy to implement to molecular dynamics simulations. Furthermore, other than nucleation rates, the critical cluster size, Zeldovich factor and free energy barrier can be calculated for this method. It has been also shown that this method is very effective for small systems. Due to the advantages of MFPT, we decided to use this method in our MD simulations.

1.3 Scope of the Thesis

The goal of this research is to understand the heterogeneous condensation of the Lennard-Jones vapour onto nanoscale particles of varying solubility by developing phenomenological models and using molecular dynamics simulations techniques.

In chapter 2, the heterogeneous condensation of a Lennard-Jones vapour onto an insoluble nanoscale seed particle is studied using molecular dynamics simulations and the results compared with the phenomenological model. First, we examine the problem of heterogeneous nucleation onto a nanoscale seed particle by considering a simple thermodynamic model, which is the extension of the liquid drop model originally developed by Reiss et al. [61]. In this model, the system has a fixed total number of particles N, a fixed volume V, and a constant temperature T. The heterogeneity is considered to be an insoluble, spherical, solid particle, while the liquid forms a uniform film that completely wets the particle giving rise to a film-particle composite and leaving the rest of atoms in the vapour phase, which is treated as an ideal gas. We study the coexistence between a liquid drop and its vapour, and its stability. Then, estimation of the nucleation rate and the height of the free energy barrier using the mean first passage time method shows that the presence of a weakly interacting seed has little effect on the work of forming very small cluster embryos but accelerates the rate by lowering the barrier for larger clusters, suggesting a competition between the energetic and entropic contributions in cluster formation in the bulk and at the heterogeneity. As the interaction is increased, the free energy of formation is reduced for all cluster sizes. A comparison of our simulation results with the model developed shows that heterogeneous classical

nucleation theory provides a good estimate of the critical size of the film but significantly overestimates the size of the barrier.

In Chapter 3, a Lennard-Jones binary mixture consisting of a non-volatile liquid nano-droplet surrounded by a solvent vapour phase is studied using Molecular Dynamics (MD) simulations to understand the adsorption process and the formation of thin film around the nano-droplet. We analyze the liquid drop model with a larger nanodroplet-vapour system and investigate adsorption process for larger nanodroplets using lattice gas model in which nano-droplet represented by a cube that has m equivalent sites for vapour particles in a lattice. Both miscible and partially miscible systems are examined. Investigations of this system show that the formation of thin film around the nano-droplet appears to be dominated by large fluctuations in the size of largest cluster, suggesting this phenomenon involves the coalescence of smaller clusters on the surface of the droplet. Then this process is followed by a subsequent growth of the film. Film sizes on different size nano droplets are also compared with the lattice gas adsorption model and the model fits well for large volumes.

The results from the simulations and theory are discussed in the final chapter. Possible corrections to the phenomenological models developed in the thesis are also given in this chapter.

The work from Chapter 2 and some preliminary results from Chapter 3 have been published as "Heterogeneous condensation of the Lennard-Jones vapour onto a nanoscale seed particle" (J. Phys. Chem. **134**, 114505 (2011)) and "The solubility transition in partially miscible, non-volatile liquid drops" (Nucleation and Atmospheric Aerosols: 19th International Conference (AIP Conf. Proc., 2013), respectively.

Chapter 2

Heterogeneous Condensation of the Lennard-Jones Vapour onto a Nanoscale Seed Particle

2.1 Introduction

The heterogeneous condensation of a vapour onto a substrate is a key step in a wide range of chemical and physical processes that occur in both nature and technology. For example, dust and pollutant aerosol particles, ranging in size from several microns down to just a few nanometers, serve as cloud condensation nuclei in the atmosphere [50, 51], while nanoscale structured surfaces provide templates for the controlled nucleation and growth of complex materials such as colloidal metamaterials [3]. The general principles of heterogeneous nucleation on bulk surfaces are well known [4, 12], but the details of how the process changes as the size of the heterogeneity becomes microscopic, and is the same size, or smaller, than the nanometer-sized fluctuations involved in the nucleation process itself, are not well understood. Recent experiments [52] have shown that vapour condensation onto small clusters and nanoparticles, with diameters of $1 - 24$ nm, occurs at supersaturations well below those predicted by classical nucleation theory [6, 7, 8, 9] (CNT) and the Kelvin relation, which suggests that very small particles are far better at activating nucleation than expected. Similarly, Sear [53] found that a microscopic heterogeneity, consisting of a single fixed spin, was sufficient to accelerate the nucleation rate in a two-dimensional Ising model by as much as four orders of magnitude. This raises interesting questions regarding how small a heterogeneity can be and still have an influence on nucleation and whether there are practical limits to our ability to study homogeneous nucleation in the presence of small concentrations of impurities.

The goal of the present work is to quantify the effect of a very small seed particle on the condensation of the Lennard - Jones (LJ) vapour, by measuring both the nucleation rate and

free energy barrier associated with heterogeneous nucleation, and compare the results with a simple thermodynamic model. Homogeneous nucleation in the LJ system has been studied by simulations [54, 55, 56, 57], as has heterogeneous nucleation on macroscopic surfaces [58]. However, studies involving small, seed particles in the LJ vapour have focused on examining the qualitative effects of highly attractive seeds, i.e. where the vapour - seed interaction is in the order of being ten times more attractive than the vapour-vapour interaction [59, 60]. By studying the impact of seeds with interactions very similar to those of the vapour phase, we hope to understand how small heterogeneities perturb the bulk system. We can then directly address the question as to whether small impurities can seriously impact our ability to measure homogeneous nucleation rates, as well as assess the ability of CNT to predict heterogeneous nucleation on seed particles. The chapter is organized as follows: A simple phenomenological thermodynamic model describing the heterogeneous nucleation onto a nanoscale heterogeneity is developed and analyzed in Section 2.2. Section 2.3 describes the molecular dynamics simulation study of the this system and compares the calculated nucleation barriers with those obtained from the phenomenological. The discussion is contained in Section 2.4.

2.2 Liquid Drop Model with an Insoluble Seed Particle

We begin examining the problem of heterogeneous nucleation onto an insoluble nanoscale seed particle by considering the simple thermodynamic model described in Fig. 2.1, which represents the heterogeneous nucleation extension of the liquid drop model [61, 62]. The system has a fixed total number of particles, N, a fixed volume, V, and a constant temperature, T. The heterogeneity is considered to be an insoluble, spherical, solid particle with radius r_0, while the liquid forms a uniform film of n_2 atoms that completely wets the particle giving rise to a film-particle composite of radius r_2. The $n_1 = N - n_2$ atoms remaining in the vapour phase are treated as an ideal gas. The first step will be to derive expressions for the equilibrium coexistence between the film and the vapour phase. This will be followed by a derivation of an expression for the free energy of formation of a film as a function of the film size.

At constant N, V, T, the Helmholtz free energy, F, is the appropriate thermodynamic

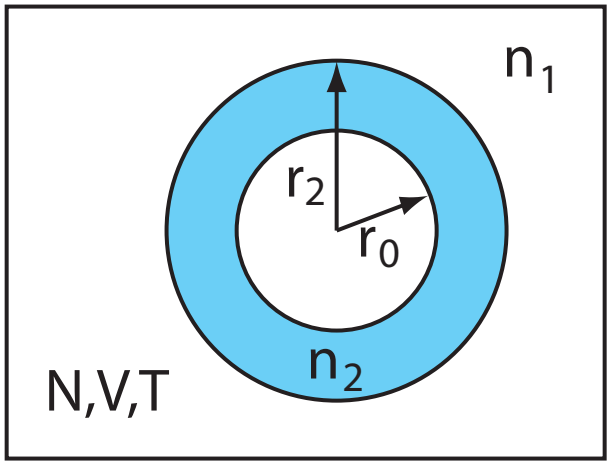

Figure 2.1: N, V, T model consisting of an insoluble heterogeneity of radius r_0 completely wet by a thin film of n_2 liquid atoms giving the film-seed composite a total radius of r_2. The vapour is an ideal gas of n_1 atoms.

potential and variations in F are given by

$$dF = dU - Td\bar{S} \ , \tag{2.1}$$

where, $U = U_1 + U_2$, is the total internal energy and $\bar{S} = \bar{S}_1 + \bar{S}_2$ is the total entropy. Here, the subscripts 1 and 2 represent the vapour and liquid phases respectively. Variations in U are given by,

$$dU_1 = Td\bar{S}_1 - p_1 dV_1 + \mu_1 dn_1 \ , \tag{2.2}$$

and

$$dU_2 = Td\bar{S}_2 - p_2 dV_2 + \mu_2 dn_2 + \gamma_{12} dA_{12} + \gamma_{02} dA_{02} \ , \tag{2.3}$$

where p_1 and p_2 are the pressures of each phase respectively, while μ_1 and μ_2 are their chemical potentials. The area of the liquid-vapour interface is given by, $A_{12} = 4\pi r_2^2$, and the solid-liquid surface area, $A_{02} = 4\pi r_0^2$. γ_{12} and γ_{02} are the planar surface tensions of the vapour-liquid and liquid-solid interfaces respectively. Here, it is assumed that the droplet is spherical and interfaces between the phases are sharp, consistent with the capillarity approximation, and both solid-liquid and liquid-vapour interfaces have been assigned to the droplet phase. Substituting Eqs. 2.2 and 2.3 into Eq. 2.1 while using the conservation laws, $dV_1 = -dV_2$ and $dn_1 = -dn_2$, along with $dA_{12} = 2dV_2/r_2$ and $dA_{02} = 0$ yields,

$$dF = -\left(p_2 - p_1 - \frac{2\gamma_{12}}{r_2}\right) dV_2 + (\mu_2 - \mu_1) dn_2 \ . \tag{2.4}$$

At equilibrium, $dF = 0$, and Eq. 2.4 yields the expected equality of chemical potentials between the two phases and the Laplace relation for the difference in pressures across a curved interface,

$$\mu_2 = \mu_1 \ , \tag{2.5}$$

and

$$\Delta p = p_2 - p_1 = \frac{2\gamma_{12}}{r_2}. \tag{2.6}$$

A more detailed description of coexistence can be obtained by using the Gibbs-Duhem relation for each phase. For the vapour, we have

$$\bar{S}_1 dT - V_1 dp_1 + n_1 d\mu_1 = 0. \tag{2.7}$$

Using $PV = n_1 kT$ and integrating Eq. 2.7 at constant T yields,

$$\mu_1(p_1) - \mu_1^{eq}(p_1^{eq}) = kT \ln \frac{p_1}{p_1^{eq}}, \tag{2.8}$$

where we have chosen the reference pressure, p_1^{eq}, as the coexistence pressure of the vapour in contact with a liquid, with a planar interface.

To obtain a Gibbs-Duhem relation for the liquid and its associated interface, first we write the total internal energy for liquid phase,

$$U_2 = T\bar{S}_2 - p_2 V_2 + \mu_2 n_2 + \gamma_{12} A_{12} + \gamma_{02} A_{02}, \tag{2.9}$$

and take the total differential to obtain,

$$\begin{aligned} dU_2 &= T d\bar{S}_2 + \bar{S}_2 dT - (p_2 dV_2 + V_2 dp_2) + \mu_2 dn_2 + n_2 d\mu_2 \\ &+ \gamma_{12} dA_{12} + A_{12} d\gamma_{12} + \gamma_{02} dA_{02} + A_{02} d\gamma_{02}. \end{aligned} \tag{2.10}$$

Combining Eqs. 2.3 and 2.10 then yields the required relation for the liquid phase,

$$\bar{S}_2 dT - V_2 dp_2 + n_2 d\mu_2 + A_{12} d\gamma_{12} + A_{02} d\gamma_{02} = 0. \tag{2.11}$$

If we assume that the surface tension is independent of pressure and that the liquid is incompressible, the integration of the Eq. 2.11 between pressures p_2^{eq} and p_2, at constant T, gives,

$$\mu_2(p_2) - \mu_1^{eq}(p_1^{eq}) = \nu_2(p_2 - p_1^{eq}) \ , \tag{2.12}$$

where $\nu_2 = V_2/n_2$ is the volume per molecule in the liquid phase. We have also taken advantage of Eq. 2.5 and the fact that Eq. 2.6 gives us $p_2^{eq} = p_1^{eq}$ in the limit $r_2 \to \infty$, i.e. at a planar interface. Combining Eqs. 2.6, 2.8 and 2.12 yields the coexistence equation,

$$kT \ln \frac{p_1}{p_1^{eq}} = \frac{2\gamma_{12}}{r_2}\nu_2 + \nu_2(p_1 - p_1^{eq}) \ , \tag{2.13}$$

where

$$p_1 = \frac{(N - n_2)kT}{V - (n_2\nu_2 + (4/3)\pi r_0^3)} \ . \tag{2.14}$$

Eq. 2.13 is equivalent to the Kelvin relation for the current model and can be solved numerically to find the equilibrium size of the film. In an open system, there would be one solution corresponding to the unstable equilibrium of the critical-sized film. Films that are thinner than the critical size tend to evaporate while thicker films grow spontaneously into a macroscopic drop as they consume molecules from a continually replenished vapour. However, in our closed system, N is fixed and the growth of the liquid film depletes the number of molecules in the vapour phase, causing the supersaturation to decrease so that the film and vapour must eventually come into stable equilibrium.

Fig. 2.2 shows numerical solutions to the equilibrium film sizes obtained from Eq. 2.13 as a function of the total volume of the system for seed particles with sizes $r_0 = 2.0\sigma$ and $r_0 = 3.8\sigma$. In the limit that $r_0 \to 0$, the model recovers the solutions describing the formation of a liquid drop in the N, V, T ensemble [62], i.e. the homogeneous nucleation, and the $r_0 = 0$ model has been included here for comparison with the heterogeneous nucleation case. We have used the Lennard-Jones parameters of Baidakov et al. [63] for p_{eq}, ν_2 and γ_{12} which are given in Table 2.1 . All droplet sizes exhibit an evaporation volume, V_e above which it is not possible to stabilize a film of any size and the stable equilibrium state consists of a dry particle surrounded by vapour. The liquid drop model, without the heterogeneity ($r_0 = 0$), has two solutions below the V_e. The large n_2 cluster belongs to the stable droplet in equilibrium with the vapour while the small droplet is the unstable, critical sized droplet that must be formed before the droplet can grow. We note two important features: firstly, there is always a barrier to the formation of the droplet, even at very small system volumes, which correspond to high initial supersaturations. Secondly, the droplet size remains finite at the evaporation volume.

When a small insoluble particle is introduced into the system ($r_0 = 2.0\sigma$), we see that there are still two solutions at volumes just below the evaporation volume, but now the size of

the small critical cluster tends to zero at a finite V, as the volume of the system is decreased so that there is no barrier to film formation at small enough volumes. Below this volume there is just one solution, corresponding to the stable thick film that grows spontaneously. As the size of the solid particle is increased, we eventually reach a seed size ($r_0 = 3.8\sigma$) for which there is never a nucleation barrier associated with the formation of the film and the stable film grows continually from $n_2 = 0$ at the evaporation volume. This final result is consistent with the results of heterogeneous nucleation of films on bulk surfaces that exhibit complete wetting.

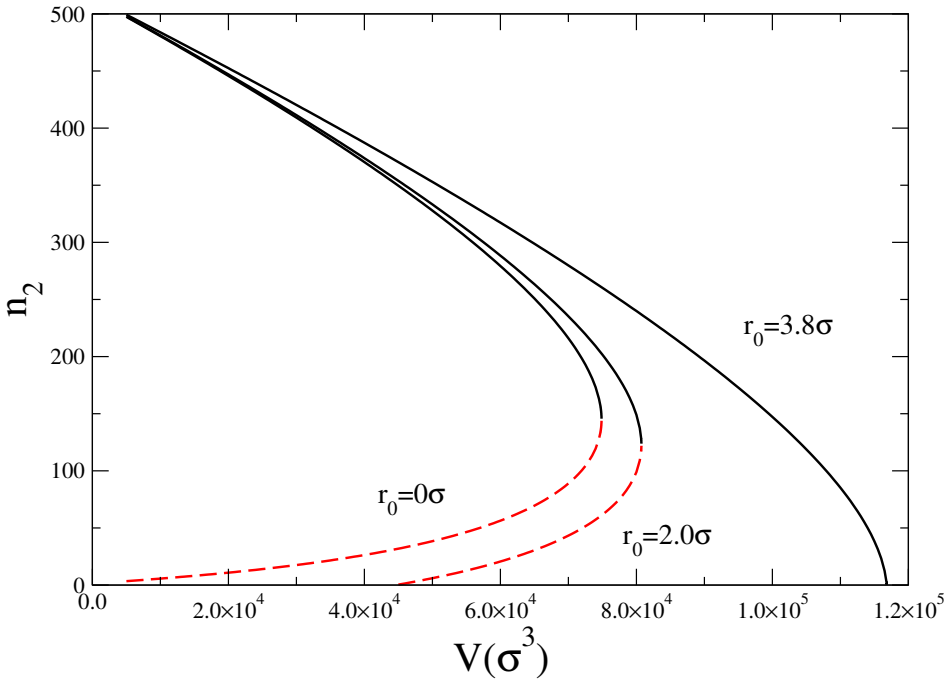

Figure 2.2: Coexistence solutions for the film size, n_2, as a function of the volume, V, from Eq. 2.13, with $N = 512$ and $T^* = 0.67$, in the presence of different size heterogeneous particles, $r_0/\sigma = 0, 2.0$ and 3.8. The locally stable and unstable solutions are represented by the solid and dashed lines respectively.

T^*	p^*_{eq}	ν^*_2	γ^*_{12}
0.67	0.00103	1.25	1.153
0.80	0.00542	1.25	0.855

Table 2.1: Parameters, in reduced units, for conditions T^*, p^*_{eq} at coexistence for the bulk liquid obtained from Baidakov et al.

To obtain an expression for the free energy of forming a film with n_2 particles, we start with Eq. 2.4, along with the expressions for the chemical potentials from Eqs. 2.8 and 2.12. Noting that $dV_2 = \nu_2 dn_2$ for a incompressible liquid, gives us an equation for dF in terms of dn_2,

$$dF = \left(v_2 \left(p_1 - p_1^{eq}\right) + \frac{2\nu_2\gamma_{12}}{r_2} - kTln\frac{p_1}{p_1^{eq}} \right) dn_2. \tag{2.15}$$

Integrating with respect to n_2, at constant temperature, and taking into account the n_2 dependancy of p_1 in Eq. 2.14 and $r_2 = \sqrt[3]{\left(\frac{3n_2\nu_2}{4\pi} + r_0^3\right)}$, yields,

$$\begin{aligned} \Delta F(n_2) = F(n_2) - F(0) \quad &= \quad -n_2 kT \ln \frac{p_1}{p_1^{eq}} + n_2(kT - \nu_2 p_1^{eq}) + \\ & \qquad NkT \ln \frac{p_1}{p_0} + \gamma_{12}(A_{12}(n_2) - 4\pi r_0^2), \end{aligned} \tag{2.16}$$

where $p_0 = NkT/(V - (4/3)\pi r_0^3)$ is the pressure of the initial vapour before any film is formed. Eq. 2.16 represents the work of forming a film of n_2 molecules starting from an infinitely thin film with $n_2 = 0$ that wets the particle. Fig. 2.3 shows plots of Eq. 2.16 at different V for the case with $r_0 = 1.0\sigma$, where we know from our coexistence curves that there is a range of volumes with two equilibrium solutions. For $V = 8.5 \times 10^4\sigma^3$, which is above the V_e, the lowest free energy state is that of the dry nanoparticle surrounded by vapour, as expected. As the volume decreases we see the formation of the stable, local minimum associated with the large film, which is separated from the dry particle state by a free energy barrier. However, at $V = 6.6 \times 10^4\sigma^3$ the large film is metastable with respect to the dry particle state. At smaller V, the thick film eventually becomes the most stable state and at even smaller volumes we reach the point where there is no barrier to the formation of the thick film. These plots also confirm that the coexistence solutions for the small and large film solutions represent unstable ($\partial^2 F/\partial n_2^2 < 0$) and stable ($\partial^2 F/\partial n_2^2 > 0$) equilibrium states.

Despite the simplicity of the thermodynamic model presented here, it captures the main features of heterogeneous nucleation on to a nanoscale impurity. The model clearly shows that even for a system that completely wets the impurity there is a free energy barrier to forming a film once the heterogeneity is small enough. The model also exhibits a hysteresis loop with the dry impurity and thick film being metastable over a range of system volumes. These metastable regions are then terminated when the free energy barriers disappears, signifying the limit of stability for each the states. However, it is worth noting that the free energy curves in Fig. 2.3 do not have the characteristic local minimum at small n_2 observed

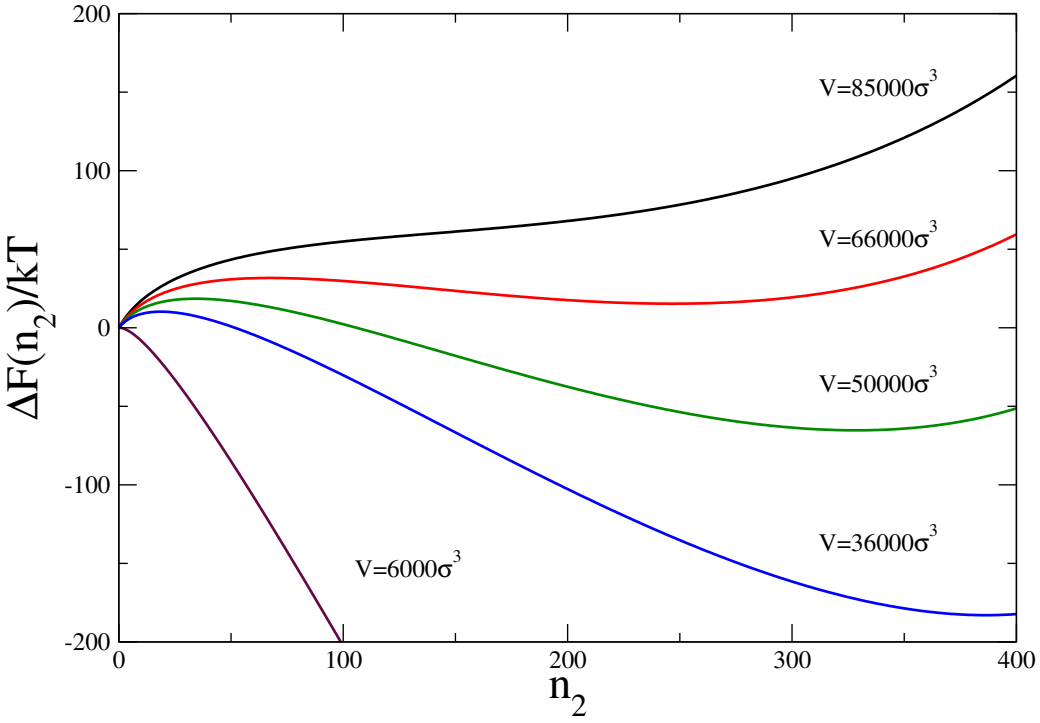

Figure 2.3: $\Delta F(n_2)/kT$ as a function of n_2, with $N = 512$, $r_0/\sigma = 1.0$ and $T^* = 0.67$, for different system volumes.

in many nanoscale heterogeneous nucleation problems and associated with the initial wetting of the impurity particles. This is because the $n_2 = 0$ reference state of the model represents an infinitely thin film that covers the entire particle. Such a state does not exist in the a molecular system where the particles have size. In principle, there is an additional term, $4\pi r_0^2(\gamma_{12}-\gamma_{01})$ that should appear in Eq. 2.16 and represents the free energy change associated with this wetting process, but this will be a negative constant applied to all film sizes. It is not included here as it does not effect the probability of observing the critical sized cluster within the context of the model.

Finally, we examine the system size dependence of the nucleation barriers and critical sizes for the nucleation of the film from the dry particle as predicted by the model. Fig. 2.4 shows the critical size of the film, n_2^* and the height of the barrier, $\Delta F(n_2^*)/kT$, as a function of the initial supersaturation, $S = p_0/p_1^{eq}$, for different numbers of system sizes, N. As N increases,

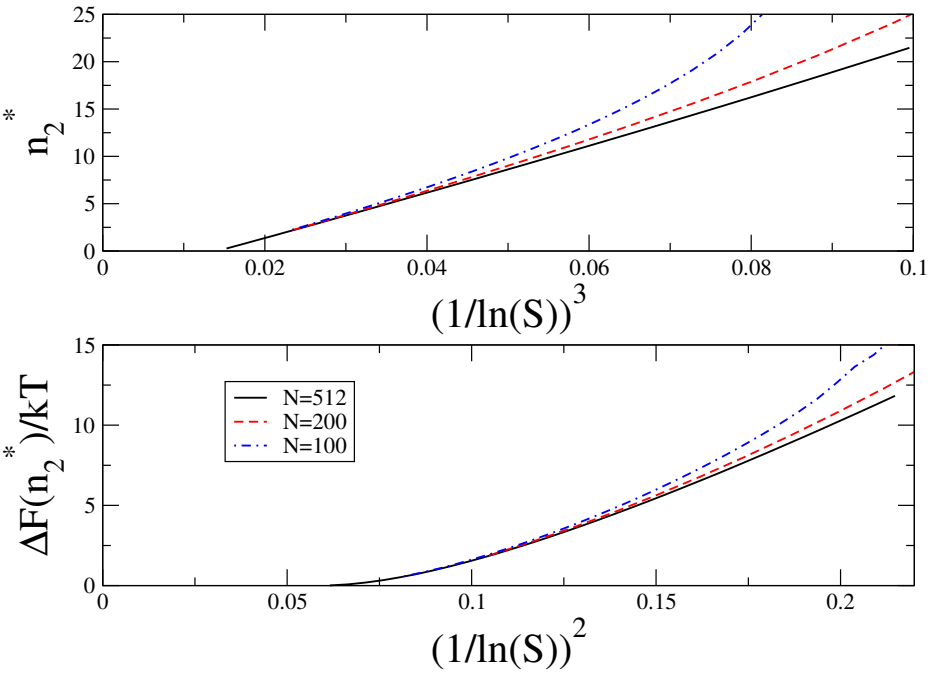

Figure 2.4: (Top) The critical film size, n_2^* as a function of $(1/\ln(S))^3$ for system sizes $N = 100, 200$ and 512. (bottom) The height of the nucleation barrier $\Delta F(n_2^*)/kT$, as a function of $(1/\ln(S))^2$ for system sizes $N = 100, 200$ and 512.

the system size effects due to the depletion of the vapour phase caused by the formation of the film should be less significant and the model should behave more like an open system. CNT predicts that the critical size of the film should be linear in $\ln(S)^{-3}$ and this is true for this model once $N = 512$, but for smaller N we see a more rapid increase in the critical size than expected.

The height of the nucleation barrier is expected to be linear in $\ln(S)^{-2}$. The curves in Fig. 2.4 (bottom) becomes more linear at low values of S, as N increases. However, the curvature of $\Delta F(n_2^*)/kT$ at high supersaturations is common for all values of N and this might be characteristic of the system approaching the limit of stability. For both n_2^* and $\Delta F(n_2^*)/kT$, the curves begin to converge with increasing system size suggesting the system size effects are becoming unimportant.

2.3 Simulations and Results

2.3.1 Simulation Details

Molecular dynamics simulations in the canonical, (N, V, T) ensemble are now used to study the condensation of a vapour onto a nanoscale heterogeneity. The composite system (vapour + heterogeneity) is modelled as a cut, but unshifted, Lennard - Jones mixture with the interaction potential,

$$V(r_{ij}) = 4\epsilon_{ij}\left[(\sigma_{ij}/r_{ij})^{12} - (\sigma_{ij}/r_{ij})^{6}\right], \tag{2.17}$$

where ϵ_{ij} and σ_{ij} represent the energy and length interaction parameters. The vapour and heterogeneity are denoted as component 1 and 2 respectively. We use $N = 512$ vapour particles with $\epsilon_{11} = 1.0$, and a single heterogeneity particle with interactions in the range $\epsilon_{12} = 1.0 - 3.0$. This system size has been shown to be large enough that the depletion of the vapour phase caused by nucleation in the N, V, T ensemble is small so the barriers are the same as those calculated in an open system [64]. The heterogeneous liquid drop model, developed in Section 2.2, also suggested that any system size effects were small with $N = 512$. All particles have the same size ($\sigma_{11} = \sigma_{22} = \sigma_{12} = 1$), the seed and gas particles have the same mass, m, and the potential is truncated at $r_c = 6.78\sigma_{ij}$, which should be long enough to approximate the full LJ potential and is consistent with a previous study of homogeneous condensation [57]. The simplicity of this model allows us to treat the heterogenous seed particle as another atom in the molecular dynamics simulation so it is free to translate throughout the system.

The simulations were carried out using the Gromacs 4.0 Package [65], with the leap-frog integration scheme. The velocity rescaling thermostat is employed to maintain the system at a reduced temperature, $T^* = kT/\epsilon_{11} = 0.67$, as this provides an efficient method for temperature control that does not appear to have a significant influence on the kinetics of nucleation, even though the particle dynamics are perturbed in a non-physical way [66]. The volume of the simulation cell is chosen to ensure the initial starting conditions correspond to a particular supersaturation, defined as $S = p/p_{eq}$, where p is the vapour pressure and p_{eq} is the equilibrium coexistence pressure at T as given by Ref. [63]. Time is measure in reduced units, $t^* = t(\epsilon_{11}/m)^{1/2}/\sigma_{11}$ and periodic boundary conditions are used to remove wall effects.

The nucleation rate and free energy barrier are obtained using the mean first passage time

(MFPT) approach explained in Chapter 1, by Reguera et al. [42, 56]. For each state point studied, we obtain 200 initial starting configurations by simulating the vapour phase in the absence of the heterogeneity for 10^6 time steps, saving configurations every 5000 time steps. The heterogeneity is inserted randomly into the vapour, but ensuring that it is not placed within σ of any vapour molecule in order to avoid the introduction of any unusually large intermolecular interactions and forces. The MD trajectory is then followed as a function of time and the cluster size distribution is analyzed every 1000 time steps until the system is nucleated. Clusters are identified using the Frenkel cluster criteria [54], which identifies liquid-like atoms as those particles that have at least five other atoms within a distance of 1.5σ, and considers two liquid-like atoms within a distance of 1.5σ to be in the same liquid cluster. For computational convenience, the seed particle is counted as a neighbour when identifying liquid particles.

$\tau(n)$, is calculated by measuring the first time the largest cluster in the system reaches the size n in a simulation trajectory, and averaging over the 200 trajectories. However, as a result of the intrinsic nature of the cluster dynamics and the fact that we only sample configurations periodically, the cluster growth is non-monotonic in time and does not proceed through a series of single particle additions or losses. It then becomes necessary to correct the time at which an n-sized cluster is observed for the first time in the simulation if a given cluster is missed in a trajectory all together, or if it is sampled out of order, i.e. when a small cluster is observed only after a larger cluster has already been sampled. We achieve this by assigning any small clusters that have not already been seen in a given trajectory, the same time that is assigned to the next largest cluster when it first appears [67]. Eq. 1.58 is fit to the data, where τ_J, n^* and c are used as fit parameters. The steady state nucleation rate, J, is then obtained from $J = 1/\tau_J V$.

To calculate the free energy of forming a cluster using the MFPT method, using Eqs. 1.59 and 1.60, it is necessary to find the steady state probability of finding an n-sized cluster, $P_{st}(n)$. We calculate this by counting the number of times a cluster of size n appears in our ensemble of trajectories and dividing by the total number of configurations.

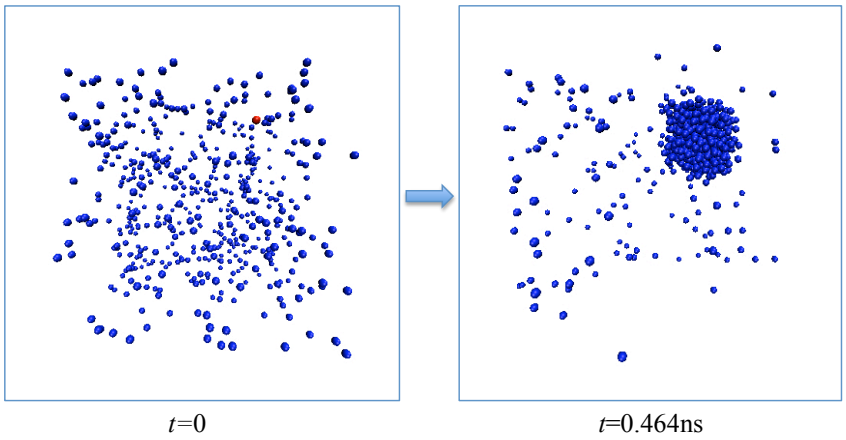

Figure 2.5: Snapshots for systems with $N = 512$, $S = 10.43$ and a seed particle (red) with $\epsilon_{12} = 2.0$ at (left) the initial configuration and (right) after the drop has nucleated.

2.3.2 Simulation Results

Fig. 2.5 shows the simulation boxes for the start and end configurations. Initially, the vapour and seed particle are randomly distributed in the box and by the end of the simulations, a droplet has formed. Fig. 2.6 shows the typical evolution of the largest cluster in the system, for a simulation trajectory with $N = 512$, $S = 10.43$ and a seed particle with $\epsilon_{12} = 2.0$. The largest cluster in the system fluctuates until $t^* = 48000$ then the cluster becomes large enough to pass the free energy barrier to nucleate. Since the N is fixed in our system, the growth of the droplet decreases the supersaturation of the surrounding vapour and eventually the droplet and vapour reach a stable equilibrium.

Fig. 2.7 shows $\tau(n)$ for systems with an initial vapour pressure of $S = 10.43$, for different seed atoms with $\epsilon_{12} = 1.0, 1.5, 2.0$, along with the fits of Eq. 1.58 to the data, while Fig. 2.8 shows the free energy barriers. To estimate the error in our calculations, we divide the ensemble of 200 runs into 10 blocks and calculate $\tau(n)$ and $\Delta F(n)/kT$ for each block. The error bars in $\tau(n)$ represent the standard deviation of the block averages and capture the degree of natural fluctuation in the times. The fluctuations grow significantly once n is greater than the critical size. The standard deviation in $\Delta F(n)/kT \approx 0.5$ near n^*, but this grows to between 1-2 for larger cluster sizes. Eq. 1.58 clearly provides a good fit to our MFPT data over the entire range of supersaturations and particles interactions studied. A full summary of the nucleation rates, barrier heights and critical cluster sizes obtained from the data fits, for all state points studied, can be found in Table 2.2.

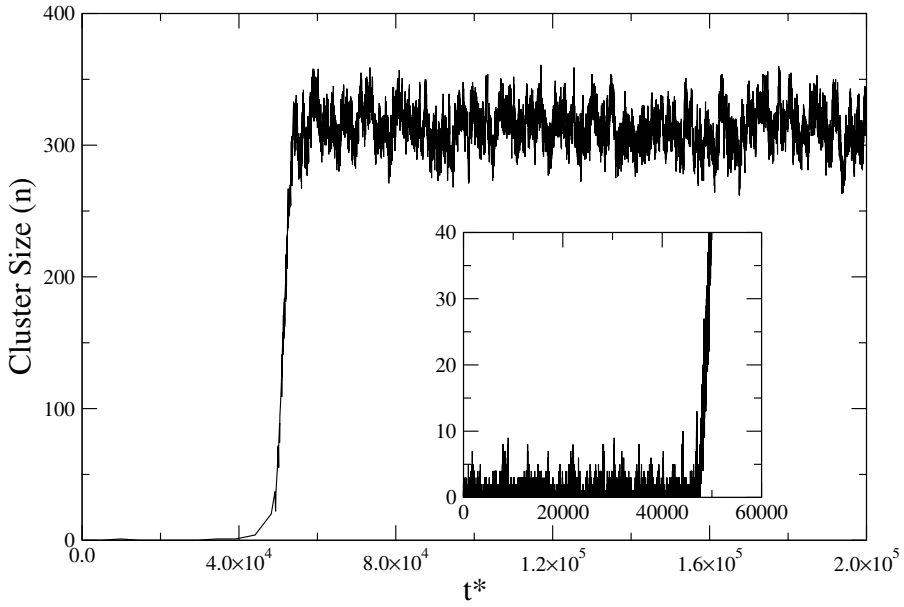

Figure 2.6: The time evolution of the largest cluster for a system with $N = 512$, $S = 10.43$ and a seed particle with $\epsilon_{12} = 2.0$. (Insert) Expanded view of the early times of the trajectory.

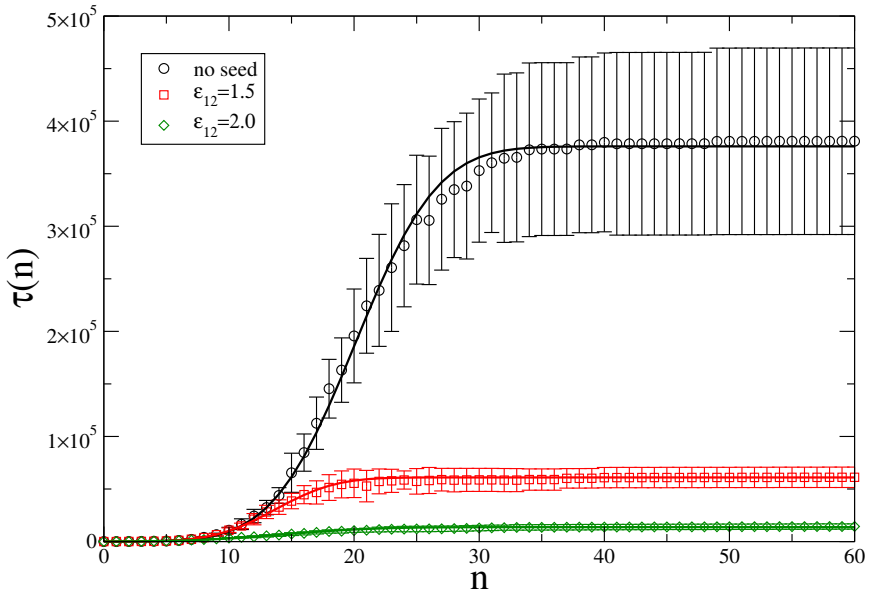

Figure 2.7: $\tau(n)$ as a function of n, for systems with $N = 512$, $S = 10.43$ and a seed particle with $\epsilon_{12} = 1.0$ (no seed), 1.5 and 2.0. The points represent data obtained from simulation and the error bars are the standard deviation of the block averages. The solid lines are best fits of Eq. 1.58 to the data.

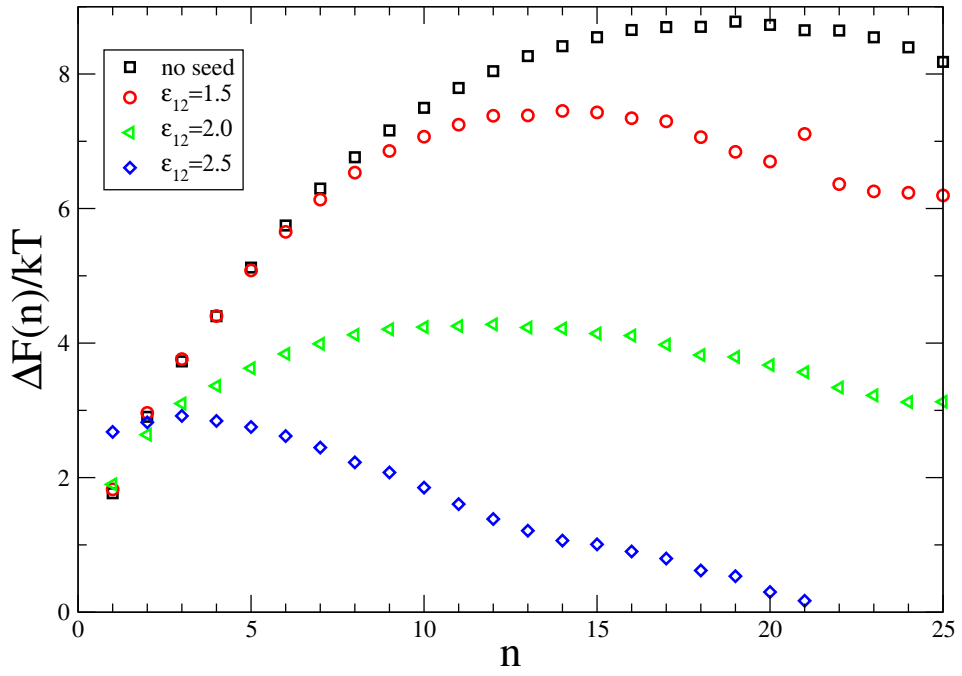

Figure 2.8: $\Delta F(n)/kT$ as a function of n, for systems with $N = 512$, $S = 10.43$ and a seed particle with $\epsilon_{12} = 1.0$ (no seed), $1.5, 2.0$ and 2.5.

Table 2.2: Summary of simulation results.

ϵ_{12}	S	$J \times 10^{25} cm^{-3} s^{-1}$	$n^*(Eq.\ 1.58)$	$n^*(barrier)$	$\Delta F(n^*)/kT$
1.0	12.83	2.92	16	13	5.20
1.0	11.16	0.16	19	17	7.51
1.0	10.43	0.04	20	19	8.78
1.5	10.43	0.09	18	16	8.04
2.0	12.83	17.70	11	7	2.99
2.0	11.16	5.21	13	9	3.82
2.0	10.43	2.36	14	12	4.28
2.0	9.50	0.66	16	14	5.11
2.0	9.00	0.33	17	16	5.77
2.0	8.52	0.09	21	20	6.75
2.0	8.01	0.03	22	23	7.95

As a check on our methodology, we have studied the case where the impurity particle has $\epsilon_{12} = 1.0$ so that the heterogeneity simply appears as one additional vapour molecule. This allows use to compare our results with the previous work of Wedekind et al. [57]. For $S = 10.43$, we obtain $J = 0.04 \times 10^{25} cm^{-3} s^{-1}$ and $n^* = 20$ from the MFPT, where we have used the LJ argon parameters, $\sigma = 0.3405$nm, $\epsilon/k = 120$ K and $m = 6.631 \times 10^{-26}$ kg to make the conversion from reduced units. The barrier calculations give $\Delta F(n)/kT = 8.78$ and $n^* = 19$. While our rate is approximately 33% higher, and our barrier approximately $0.5kT$ lower, than that obtained by Wedekind et al. [57], the results are comparable when the slight difference in the definition of the supersaturation and the error in our calculations are taken into account.

The general effect of increasing the attraction of the seed particle is to increase the rate by lowering the barrier and decreasing the critical cluster size. With $\epsilon_{12} = 1.5$, the work of forming small clusters with sizes 1-5 is the same as in the homogeneous case, with no seed, but then the heterogeneous barrier becomes lower for larger cluster sizes. To understand this, we analyze the MD trajectories and identify both the largest liquid cluster, which is our order parameter, and the largest cluster containing the seed. Fig. 2.9 shows the two measures do not always coincide and most of the fluctuations involving small clusters do not contain the seed so the probability of seeing these clusters in the ensemble remains unchanged by the presence of the seed. However, the seed is always part of the cluster that eventually fluctuates over the barrier, suggesting that the added attraction is sufficient to help build the larger clusters and make them more probable that they would normally be, causing the barrier to decrease.

When $\epsilon_{12} = 2.0$, Fig. 2.8, shows that the free energy of the smaller clusters ($n > 3$) is now decreased below that of the no seed case. At the same time, we also see that while the formation of monomers, dimers and trimers still appears to be relatively independent of the seed, (Fig. 2.10), the seed appears in most, but not all, of the larger fluctuations. For example, at $S = 10.43$, the seed is observed to be connected to trimers and 5-omer 55% and 79% of the time, respectively. The seed is found to be in clusters larger than $n = 10$ more than 96% of the time. This shows that the heterogeneity is playing an integral role in lowering the free energy of forming the clusters. Furthermore, as the interaction between the seed and the vapour increases, the impurity plays an increasingly significant role even in the

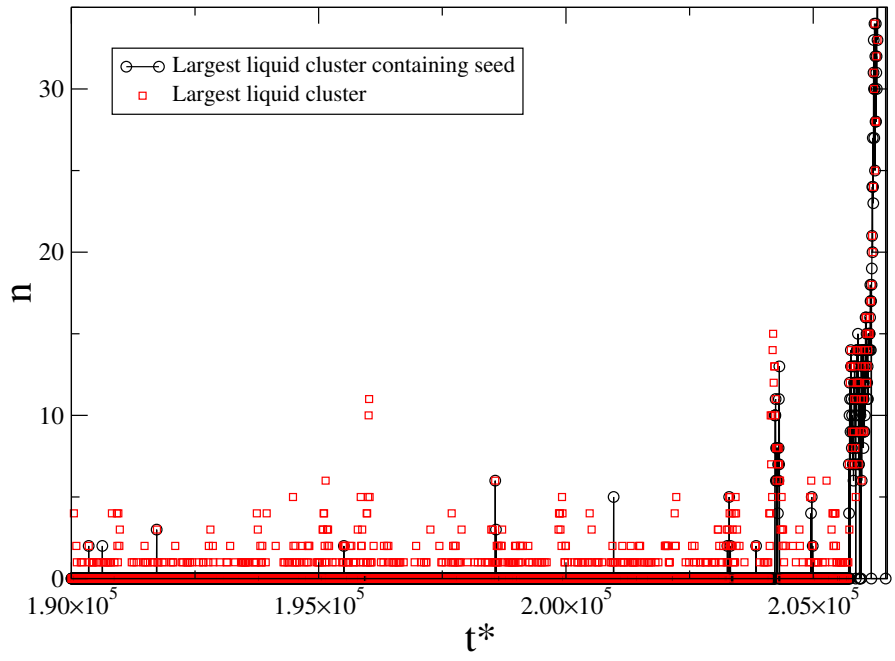

Figure 2.9: Size of the largest cluster (squares), and size of the largest cluster containing the seed (joined circles) as a function of time in a MD trajectory with $\epsilon_{12} = 1.5$ and $S = 10.43$.

smaller clusters.

Finally, when $\epsilon_{12} = 2.5$, the nucleation times are very rapid and we are probably reaching the limits at which the MFPT method can be applied and the free energy barrier calculations may not be reliable. In particular, it becomes difficult to calculate the steady state probabilities because the clusters move over the barrier so quickly, before establishing the equilibrium for the precritical clusters. It should be remembered that the MFPT method is derived on the basis that the barrier is high so that the steepest descent approximation is valid. This may not be the case with $\epsilon_{12} = 2.5$.

We have also checked the effect of changing system size on the nucleation rate and free energy barrier height at a fixed S but a different system size. N=257 and N=1025 which includes seed particles too, are simulated at supersaturation S=9.00. Fig. 2.11 shows the MFPT and their fit to Eq. 1.58.

Fig. 2.12 illustrates the free energy barriers for these systems. At a fixed S,$\Delta F(n)$, and J is expected to remain the same. Bottom plot shows corrected $\Delta F(n)$ values using N=257

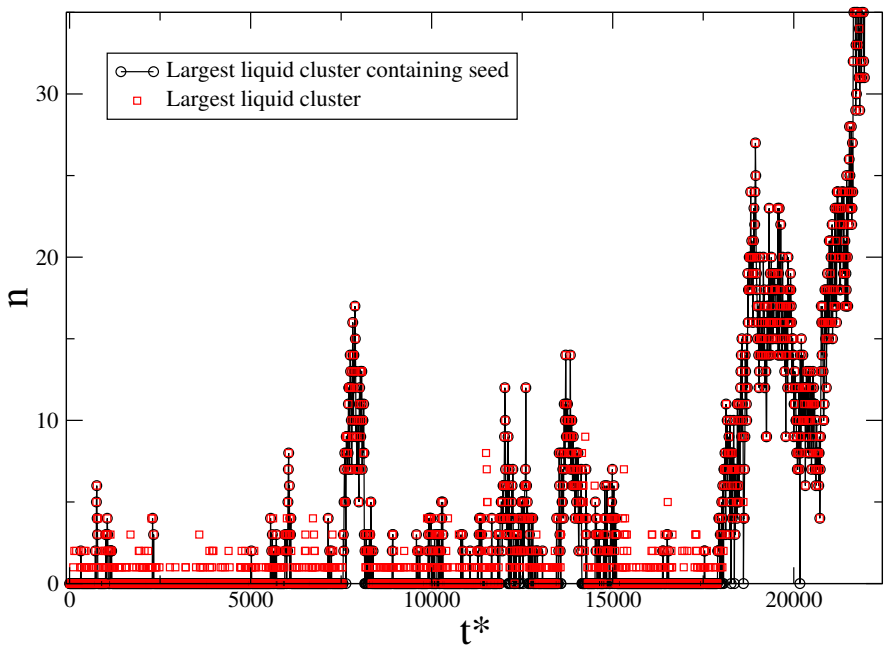

Figure 2.10: Size of the largest cluster (squares), and size of the largest cluster containing the seed (joined circles) as a function of time in a MD trajectory with $\epsilon_{12} = 2.0$ and $S = 10.43$.

as reference and equation is given in the figure. Therefore $\Delta F(n)$ values for N=513 system will be about $\ln(513/257) \sim 0.7kT$, while N=1025 system $\ln(513/257) \sim 1.4kT$ lower than the N=257 system.

Many phenomenological models, like the one developed in Section 2.2, are developed using macroscopic concepts such as particle wetting, i.e., where the seed particle is completely surrounded by layers of condensing fluid phase. However, when the films, clusters and heterogeneities are all nanoscale objects, we would expect fluctuations to play a significant role in their structure and properties. In this respect, it is worth investigating the location of the heterogeneity in the nucleating cluster. For example, a closer look at Figs. 2.9 and 2.10 shows some fluctuations where the largest cluster liquid containing the seed intermittently drops to zero while the largest liquid cluster in the system grows. This effect can be seen more dramatically in Fig. 2.13 (left), where the seed particle appears to leave and rejoin the largest cluster in the system, even after it has nucleated to form the equilibrium drop, suggesting the seed is only weakly associated with the cluster. However, this may also be related to a

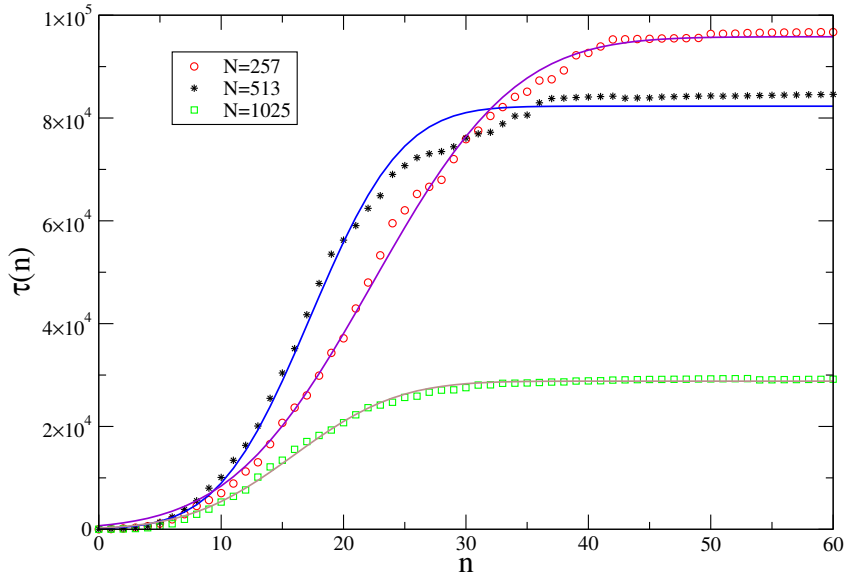

Figure 2.11: $\tau(n)$ as a function of n, for systems with $N = 256, 512$ and 1024, $S = 9.00$ and a seed particle with $\epsilon_{12} = 2.0$. The solid lines are best fits of Eq. 1.58 to the data.

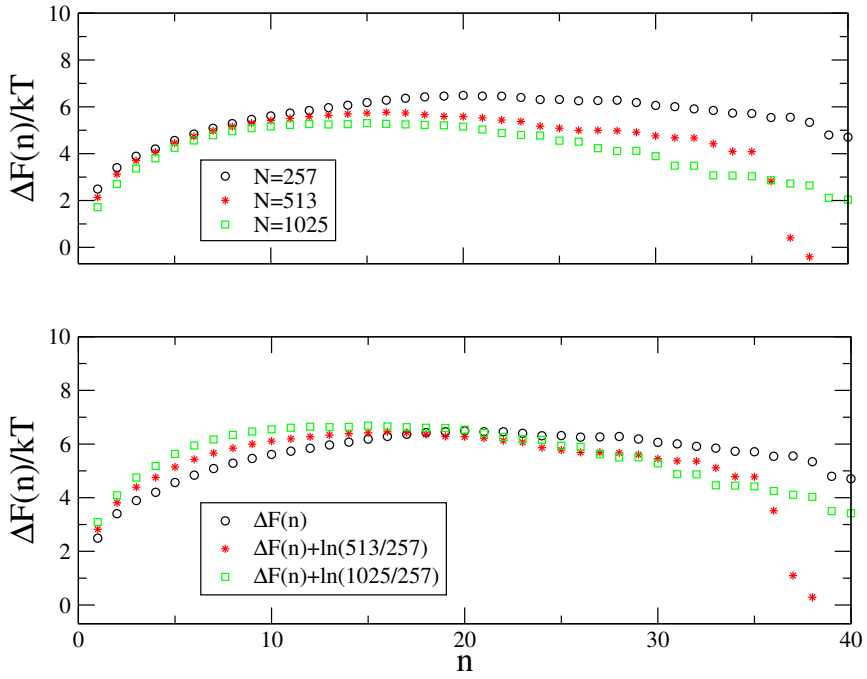

Figure 2.12: $\Delta F(n)/kT$ as a function of n, for systems with $N = 256, 512$ and 1024, $S = 9.00$ and a seed particle with $\epsilon_{12} = 2.0$.

technical aspect of how the clusters are defined. It is important to note that in our simulations it is necessary to define a cluster, but such a definition, while physically motivated, remain somewhat arbitrary and contains threshold values, that may introduce simulation artifacts. This work has used the Frenkel cluster definition, which requires liquid-like atoms to have four neighbours within 1.5σ, then two liquid-like atoms belong to the same cluster if they are within 1.5σ of each other. If the seed particle was near the surface of the largest cluster, where the atoms only have a few neighbours, it may not be directly connected with a liquid-like atom, causing the size of largest cluster containing the seed to go to zero.

To check for this artifact, we also follow the MD trajectories using an alternative cluster criteria. Stillinger identifies two particles as belonging to the same cluster if they are with a fixed cutoff radius, which is usually taken to be 1.5σ. Atoms at the surface of a large cluster that may not have been included in the Frenkel cluster would be included in the Stillinger cluster. Fig. 2.13 (right) shows the largest cluster and the largest cluster containing the seed, both defined by the Stillinger criteria, for the same MD trajectory as shown on the left. The Stillinger cluster is always larger than that the Frenkel cluster, as expected. Before the nucleation event, the largest cluster and the largest cluster with seed are not always the same, even using the Stillinger cluster, highlighting the fact the fluctuations involving small clusters are independent of the seed. However, as it nucleates and grows, the seed is always contained in the largest Stillinger cluster. This confirms that the seed is always part of the nucleating cluster, but may appear near the surface of the drop when $\epsilon_{12} = 1.5$. Fig. 2.14 the same analysis carried out for a system with $\epsilon_{12} = 2.0$. Here, the seed particle is almost always part of the largest cluster using both criteria, suggesting the additional attraction causes the seed to be totally covered by the cluster.

We can further quantify the location of the seed particle within the larger clusters by calculating $ps(r)$, the radial probability of finding the seed a distance r from the centre of mass of the cluster, for different n-size clusters, and comparing this with the density profile of the cluster (see Fig. 2.15). With $\epsilon_{12} = 2.0$, the small cluster sizes of 10 and 14 give rise to broad density profiles where the density of the core is very much lower than the bulk. Nevertheless, it is clear that the seed is generally located in the center of the cluster, so that it is effectively wet by the condensing vapour. It is not until the cluster is size $n = 20$, (see Fig. 2.16) which is post critical, do we see that the density at the core of the cluster starts

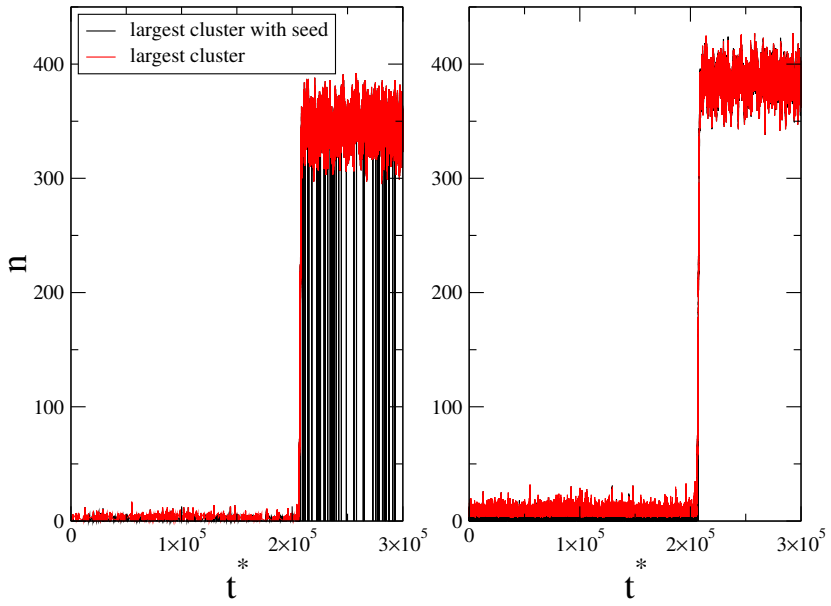

Figure 2.13: The largest cluster and the largest cluster containing the seed using (left) the Frenkel and (right) Stillinger cluster criteria as functions of time with $\epsilon_{12} = 1.5$ and $S = 10.43$.

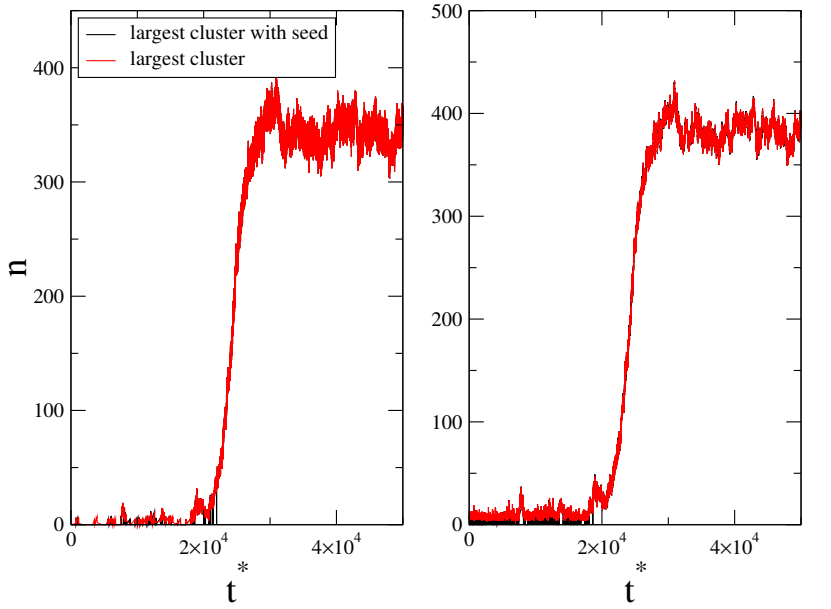

Figure 2.14: The largest cluster and the largest cluster containing the seed using (left) the Frenkel and (right) Stillinger cluster criteria as functions of time with $\epsilon_{12} = 2.0$ and $S = 10.43$.

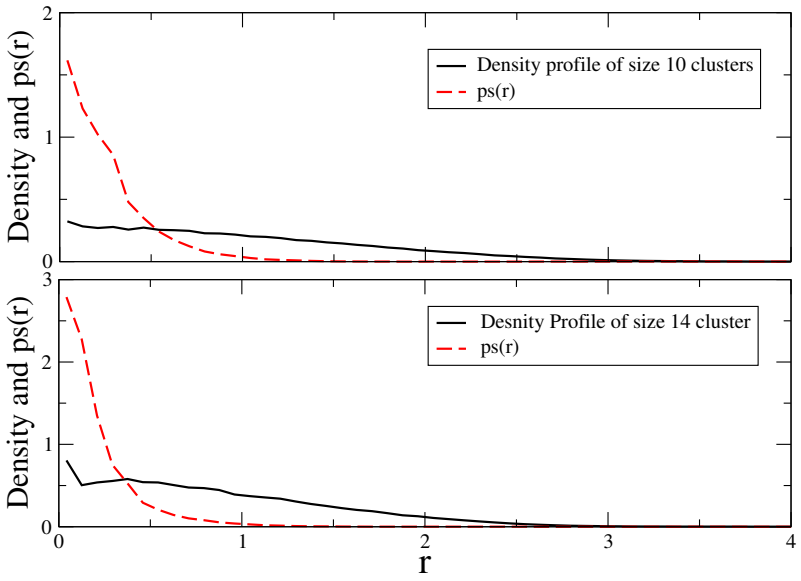

Figure 2.15: The density profile (solid line) and $ps(r)$ (dashed line) for n=10 (top) and n=14 (bottom) clusters, with $S = 10.43$ and $\epsilon_{12} = 2.0$.

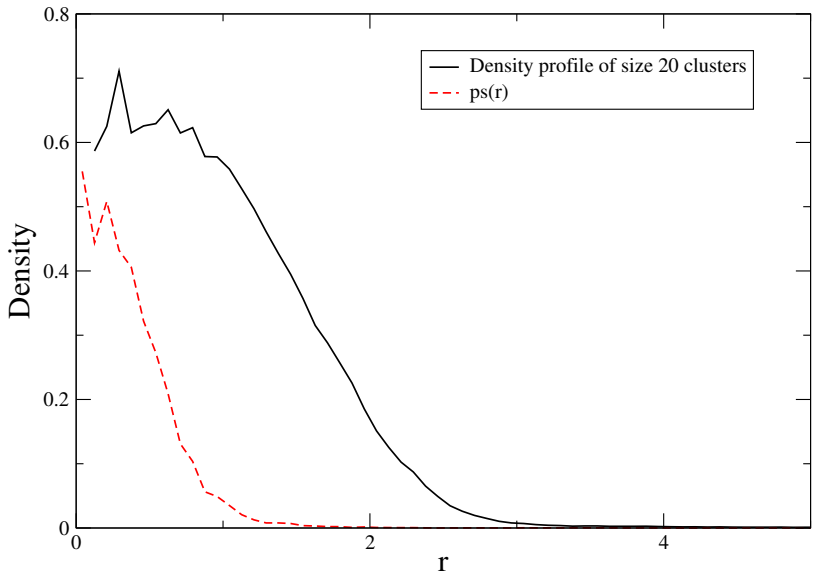

Figure 2.16: The density profile (solid line) and $ps(r)$ (dashed line) for n=20 clusters, with $S = 10.43$ and $\epsilon_{12} = 2.0$.

to reach that of the bulk. We have also looked at density profile and $ps(r)$ for the same system but with $\epsilon_{12} = 1.5$, and and these plots show similar to previous one. One of the key assumptions of CNT is that the uniform drop has the same density and properties as the bulk liquid. That is clearly not the case here and suggests that CNT would have difficulty in predicting the properties of nucleating cluster in this system.

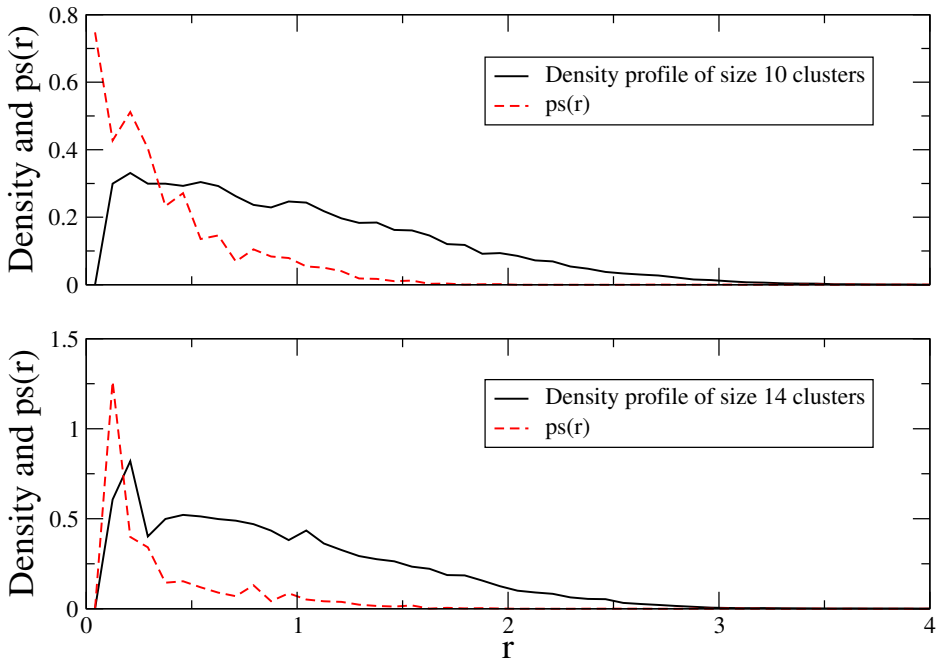

Figure 2.17: The density profile (solid line) and $ps(r)$ (dashed line) for n=10 (top) and n=14 (bottom) clusters, with $S = 10.43$ and $\epsilon_{12} = 1.5$.

To study the effects of supersaturation on heterogeneous nucleation, we use the MFPT method to calculate the rate of nucleation and $\Delta F(n)/kT$ for a system containing a seed particle with $\epsilon_{12} = 2.0$ over a range of S. Fig. 2.19 compares the heterogeneous nucleation rates involving the seed with the homogeneous nucleation rates. Clearly, the heterogeneous nucleation rates increase by 1-2 orders of magnitude over the range of S studied and we are able to measure the heterogeneous rates at lower S, directly in the simulation, than is the case for homogeneous nucleation. However, it is worth noting that the heterogeneity used in our study is not significantly different from the vapour and it is surprising that such increases are possible with such small perturbations.

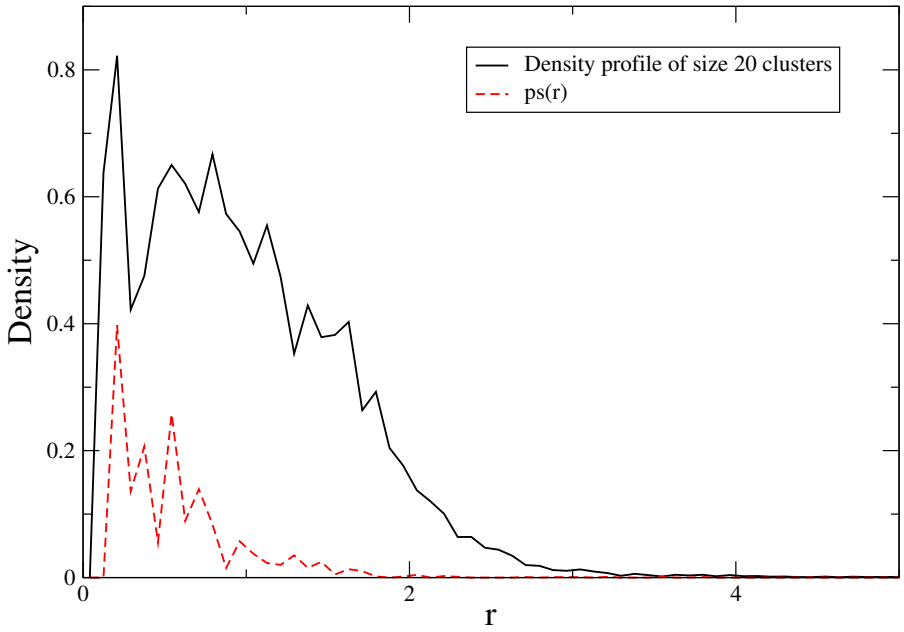

Figure 2.18: The density profile (solid line) and $ps(r)$ (dashed line) for n=20 clusters, with $S = 10.43$ and $\epsilon_{12} = 1.5$.

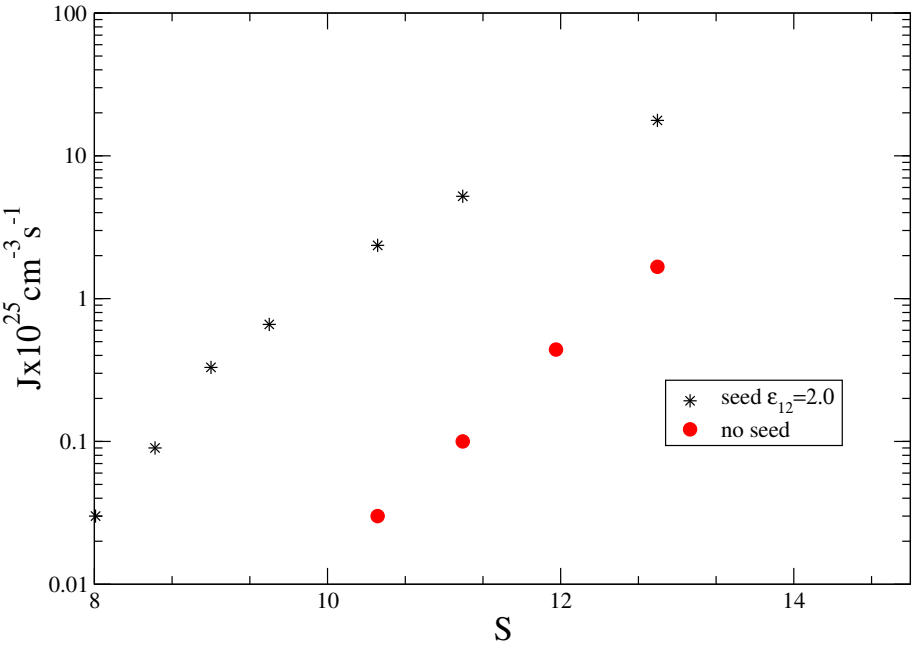

Figure 2.19: Rate versus S for systems with $N = 512$, with and without a seed particle with $\epsilon_{12} = 2.0$.

Fig. 2.20 shows $\Delta F(n)/kT$ and as expected, the barrier to nucleation decreases with increasing supersaturation. We also note that the barrier calculated here does not exhibit a minimum associated with wetting, which is somewhat consistent with our observation that the seed particle is not always wet in the macroscopic sense. These calculations allow us to compare the size of the critical nucleus and height of the barrier found from simulation with the predictions of the CNT-based model in Fig. 2.21. The supersaturation for the model is defined as p_0/p_{eq} in order to maintain the self-consistency with the simulations. This assumes that the LJ vapour phase is well described by an ideal gas at the temperatures and densities studied, which is generally true away from the critical point [43, 68], but still leads to us underestimating the supersaturation in the model by approximately 14% compared to the simulation at $S = 10.43$. The MFPT time approach gives us estimates of the critical size both through the fits of Eq. 1.58 and from the free energy calculations. These are both very close to, but a little lower than the predictions of the model. On the other hand, the model overestimates the heights of the free energy barriers by a 100% or more, which would lead to many orders of magnitude error in the rate.

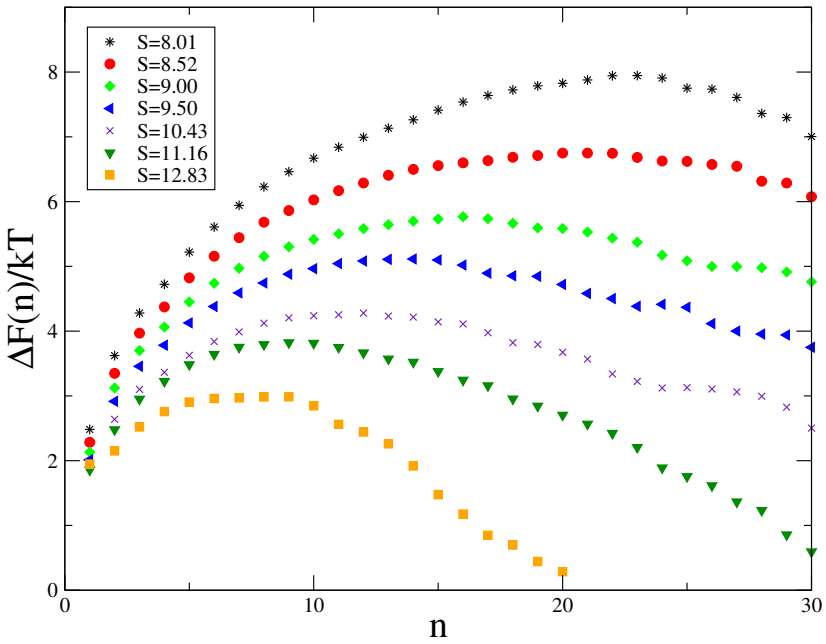

Figure 2.20: $\Delta F(n)/kT$ as a function of n at different supersaturations for a system with $N = 512$ and a seed particle with $\epsilon_{12} = 2.0$.

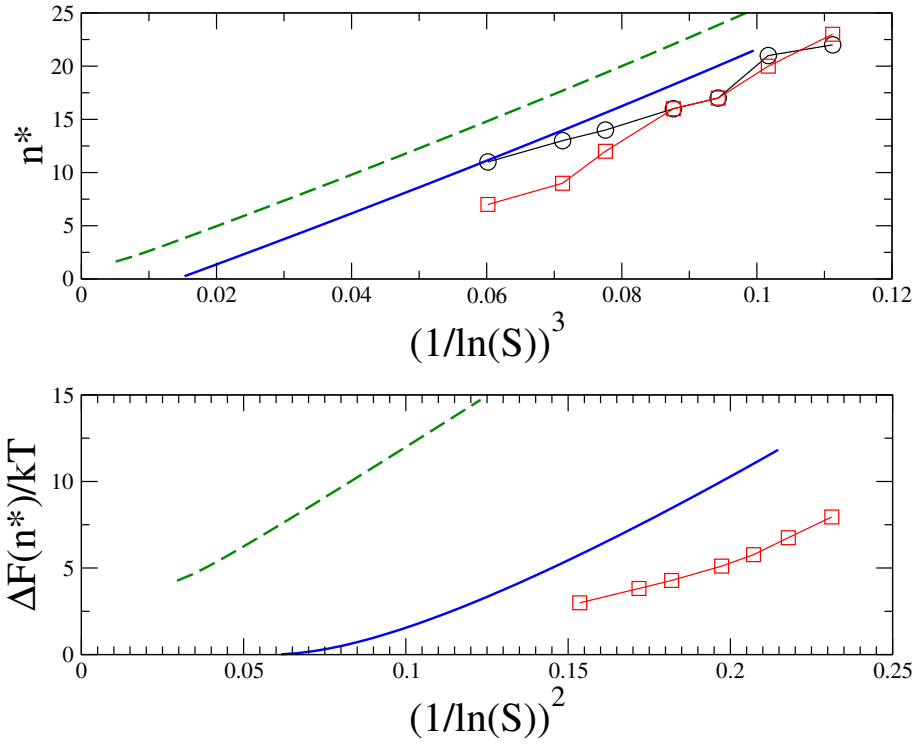

Figure 2.21: (Top) Critical cluster size, n^* as a function of $(1/\ln S)^3$. The circles and squares were obtained from fits of Eq. 1.58 to our simulation values of $\tau(n)$ and the $\Delta F(n)/kT$ curves in Fig. 2.20, respectively. The solid line is obtained from the model using Eq. 2.16, with $r_0/\sigma = 1.0$, and the dashed line is the liquid drop model with no heterogeneity. (Bottom) Critical barrier height, $\Delta F(n^*)/kT$, as a function of $(1/\ln S)^2$. Symbols are the same as above.

2.4 Discussion and Conclusion

One of the goals of this work was to develop an understanding of how the presence of a small, nanoscale heterogeneity effects the condensation of a vapour and to quantify this by measuring both the nucleation rate and calculating the free energy barrier for the process. The obvious result is that the presence of the heterogeneity allows nucleation to occur faster, but when the attraction between the seed and the vapour is only marginally more attractive than the vapour-vapour interaction, we see the work of forming small clusters is essentially unchanged and the free energy is only lowered for the larger clusters. This appears to result from an interesting balance between the energetics of cluster formation and the entropic, or translational degrees of freedom, inherent in the system. There is a small energetic advantage to forming a monomer liquid particle that includes the seed, but there are many more ways

of forming the monomer without the seed and these dominate the statistics in the density of states. Hence, there is no change in $\Delta F(n)$ for the small clusters. Larger clusters are rarer and the energetic advantage of including the seed in a cluster increases because it can have more neighbours. Eventually, the additional energy contribution dominates so the seed is connected to all the larger clusters and the barrier is lowered compared to homogeneous nucleation.

We could completely decouple the heterogeneous and homogeneous processes by considering an order parameter that focuses just on n-sized clusters that include the seed. However, Fig. 2.9 suggests the height of the nucleation barrier and the rate should remain unaffected because the seed is always part of the cluster that goes over the barrier and it is part of this cluster long before it reaches the critical size. As a result, the MFPT of the larger clusters will not change and neither should the probability of finding the larger clusters within the ensemble of runs. The work of forming the smaller clusters would be expected to increase, as the probability of finding monomers and dimers etc decreases relative to the homogeneous case and the probability of finding no liquid-like atoms connected to the seed increases.

We also wished to make some quantitative assessment of the effect small heterogeneities may have on our ability to measure homogeneous nucleation. The presence of a single seed in the current simulations changes the rate of nucleation by one or two orders of magnitude, but it is important to note that we have relatively high concentration of heterogeneities in our system and we would expect, on the basis of the entropic arguments presented above, that the effect should decrease as the concentration of heterogeneities decreases.

Finally, the comparison of our simulation results with those of our model show that the simple capillarity base approach is able to give good estimates of the critical sizes but not of the barrier heights themselves. Reguera et al. [69] found similar problems for CNT in homogeneous nucleation. Similarly, Winkler et al. [52] found that small nanoscale impurities were much better at activating heterogeneous nucleation than simple CNT based heterogeneous nucleation models suggested. We find the same trend here. The simulation nucleation rates are much higher than predicted by the model.

Nevertheless, the model does capture the general features of heterogeneous nucleation, demonstrating both a spinodal limit in the supersaturation for a fixed sized heterogeneity and a critical size of activation, where the barrier to nucleation goes to zero for a completely

wetting system above a certain size heterogeneity. There are also many corrections that could be introduced to the model to account for the small size of the system, such as size dependent surface tensions or the disjoining pressure, which provides a thermodynamic description of the interaction of the interfaces in a very thin film, that will probably lead to some improvement in the agreement. However, the very concepts of surface wetting and contact angle become poorly defined when describing processes involving heterogeneities that are of the small size considered here and more molecular approaches may be needed to describe nanoscale heterogeneous nucleation accurately.

Chapter 3

Vapour Condensation onto a Non-volatile Liquid Drop

3.1 Introduction

Atmospheric aerosols ranging in size from a few molecules to a 100 μm and containing complex mixtures of soluble, insoluble, miscible and immiscible species from a variety of anthropological and natural sources, play a critical role in the microphysics of clouds. Soluble and insoluble particles can act as cloud condensation nuclei (CCN) by providing heterogeneous nucleation sites that lower the free energy barrier for droplet formation and ice nucleation. They also serve as reactants and catalysts in atmospheric chemical cycles. However, the ability of aerosol particles to initiate water uptake is dependent on both the chemical composition of the particle and its size [70]. Consequently, understanding how composition, the distribution of material inside a particle and particle size impacts its CCN affinity remain important questions.

Köhler theory of activation [71, 72, 73] is based on the stability of the solutions to the Kelvin relation for a volatile solvent vapour in contact with a non-volatile drop and argues condensation begins at the vapour pressure where the drop becomes unstable with respect to particle growth, i.e. when there is no nucleation barrier. While nucleation theory provides a more detailed picture of condensation as a barrier crossing process, the difference in the predictions of the two approaches only becomes apparent for very small non-volatile drops [22] and the simplicity of the activation theory is appealing in most practical cases. When the liquids in the drop are ideal, the Kelvin relation has a stable and unstable region in the coexistence curve but Reiss and Koper [74] found that the Kelvin relation involving a non-ideal liquid solution exhibits an additional unstable branch that is related to the mixing of the two components. Tanlanquer and Oxtoby [32] used classical density functional theory

(DFT) to explore the properties of miscible and partially miscible systems and showed that a solubility transition, between a drop with surface absorbed solvent and a drop with solvent mixed into the core occurs before activation in the partially miscible case.

Deliquescence, where solid particles of soluble salts absorb water directly from the surrounding vapour to form solution droplets, provides an alternative way for particles to grow in the atmosphere. Measurements of micro-sized levitated [75, 76] particles showed deliquescence occurred at a well defined relative humidity corresponding to the vapour pressure where the activity of the water vapour equals the activity of the water in the bulk salt solution, but experiments on nanometer sized particles suggest surface effects can change the nature of the transition [24, 25, 27, 77]. Theoretical studies [22, 28, 31, 78, 79] show the properties of a surface film, that partially dissolves the soluble core, and the nucleation barrier associated with the phase transition play increasingly important roles in deliquescence as the particles becomes smaller, suggesting similar effects may become important for small droplets of partially miscible mixtures that can phase separate.

In this chapter, we use a combination of molecular dynamics (MD) simulations and thermodynamic theory to explore the kinetics and thermodynamics of condensation of a vapour onto nanoscale, non-volatile liquid drops for systems made up of miscible and partially miscible solvent-solute mixtures. In particular, we are interested in observing features consistent with the presence of a solubility transition in nanoscale droplets. We use a binary mixture of Lennard-Jones particles in our MD simulations because this is a model where the volatility of the component in the drop and the energy of mixing for the two components are easily controlled by adjusting the well depth in the interaction potentials between particles. Measurements of the equilibrium drop size and density of the condensing solvent at the core of the droplet show that the miscible systems always mix into the core of the drop, while still showing signs of surface enrichment of the volatile component. The partially miscible systems only begin to mix into the droplet core at an onset volume, once there is a significant amount of vapour condensed onto the drop surface, suggesting the presence of a solubility transition. We also develop a simple capillarity based non-volatile liquid drop model that captures the free energy landscape for a transition between a small and large drop, characteristic of a solubility transition, in the partially miscible system. We use this model to compare the roles of nucleation and Köhler activation for small soluble droplets.

The rest of the chapter is organized as follows: Section 3.2 describes the development and analysis of the non-volatile liquid drop model while Section 3.3 outlines a simple lattice gas model describing the surface absorption of a gas onto a nanoscale particle. In section 3.4, the molecular dynamics studies of the non-volatile drop system are described and the results are compared to the predictions of the thermodynamic and statistical mechanics models. Section 3.5 contains our discussion and conclusions.

3.2 Non-volatile liquid drop model

3.2.1 Model Development

The non-volatile liquid drop model consists of a canonical ensemble of N_1 particles of the volatile species and N_2 particles of the non-volatile species contained in a fixed volume V, at a fixed temperature T. All N_2 particles of the non-volatile species are contained in the spherical droplet phase, along with n_1^d particles of the volatile species that have dissolved into the droplet phase to produced a mixed droplet. The remaining $n_1^v = N_1 - n_1^d$ particles of species one are in the vapour phase which is treated as an ideal gas.

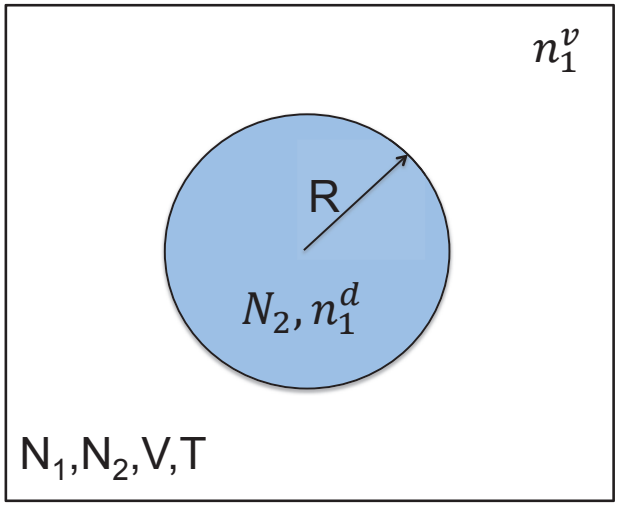

Figure 3.1: Non-volatile liquid drop model consists of a liquid drop of radius R, containing n_1^d particles of the solvent phase that have condensed and dissolved in the N_2 particles of the non-volatile component. The drop is surrounded by a n_1^v particles of the solvent in the gas phase. The system has fixed N_1, N_2, V, T.

At constant N_1, N_2, V, T, the Helmholtz free energy, F, is the appropriate thermodynamic

potential, with variations in F being given by

$$dF = dU - Td\bar{S}, \tag{3.1}$$

where $U = U^v + U^d$ is the internal energy, $\bar{S} = \bar{S}^v + \bar{S}^d$ is the entropy, and we have denoted quantities relating to the vapour phase and droplet phase with the superscripts v and d, respectively. Variations in U are given by

$$dU^v = Td\bar{S}^v - p^v dV^v + \mu_1^v dn_1^v, \tag{3.2}$$

$$dU^d = Td\bar{S}^d - p^d dV^d + \mu_1^d dn_1^d + \gamma dA^d, \tag{3.3}$$

where p^v and p^d are the pressures in the respective phases, μ_1^v is the chemical potential of component one in the vapour phase, μ_1^d is the chemical potential of component one in the drop phase, $V^d = \nu_1 n_1^d + \nu_2 N_2$ is the volume occupied by the drop and $V^v = V - V^d$ is the volume accessible to the vapour. Here, ν_i is the molecular volume of component i in the bulk liquid phase. We will assume that the drop-vapour interface is sharp, consistent with the capillarity approximation, so that the surface area of the drop is given by $A^d = 4\pi R^2$, where R is the radius of the drop, and γ is the bulk planar surface tension. It should be noted that Eq. 3.3 does not contain any chemical potential terms for species two because the non-volatile component does not exchange particles with the vapour phase, yielding $dn_2^d = 0$. However, in principle, dU^d should include a term corresponding to the work required to transfer particles from the pure non-volatile drop to the mixed drop. CNT generally assumes this term is large and negative but independent of the radius of the drop so that it is ignored as it does not effect the nucleation rate [80]. As the derivation proceeds, it will become clear that neglecting this term in Eq. 3.3 amounts to assuming that component two behaves ideally in solution even if we have included non-ideal behaviour for component one in the drop phase.

Using the conservation conditions $dV^v = -dV^d$ and $dn_1^v = -dn_1^d$, along with the relation $dA^d = 2dV^d/R$, in Eqs. 3.1-3.3 yields

$$dF = \left(p^v - p^d + \frac{2\gamma}{R}\right) dV^d + \left(\mu_1^d - \mu_1^v\right) dn_1^d \ , \tag{3.4}$$

which gives the equilibrium conditions satisfying $dF = 0$ as

$$\mu_1^d = \mu_1^v \tag{3.5}$$

and

$$p^d - p^v = \frac{2\gamma}{R}. \tag{3.6}$$

To obtain a more detailed model we need to find relations describing the chemical potential terms. Integrating the Gibbs-Duhem relation for the vapour phase, $\bar{S}^v dT - V^v dp^v + n_1^v d\mu_1^v = 0$, at constant T gives

$$\mu_1^v(p^v) - \mu_1^{eq}(p_1^{eq}) = kT \ln \frac{p^v}{p_1^{eq}}, \tag{3.7}$$

where we have used the coexistence pressure of the vapour in contact with the pure fluid via a planar interface, p_1^{eq}, as the reference state.

Starting from Eq. 3.3 and using the fundamental equation for U^d yields the Gibbs-Duhem relation for the drop and its associated surface,

$$\bar{S}_1^d dT - V^d dp^d + n_1^d d\mu_1^d + A^d d\gamma = 0. \tag{3.8}$$

However, the surface tension of a solution drop is generally dependent of the concentration of the species and Eq. 3.8 highlights the fact that this would have an effect on the chemical potential of the components in the drop. This problem arises because, as part of the capillary approximation, the surface has been assigned to the drop. To avoid the complications of having to deal with the concentration dependence of γ and to obtain an expression for the chemical potential that is correctly related to ν_1, it is necessary to make use of a Legendre transformation of the Gibbs free energy of the drop, which is given by,

$$G^d = U^d - T\bar{S}^d + p^d V^d. \tag{3.9}$$

Taking the complete differential of G^d, using Eq. 3.3 and then taking the derivative with respect to p^d, at constant T, n_1^d, yields,

$$\left(\frac{\partial G^d}{\partial p^d}\right)_{T,n_1^d} = V^d. \tag{3.10}$$

Finally, taking the derivative of Eq. 3.10, this time with respect to n_1^d, at constant p^d, yields a Maxwell relation,

$$\left[\frac{\partial}{\partial n_1^d}\left(\frac{\partial G^d}{\partial p^d}\right)_{T,n_1^d}\right]_{p^d} = \left[\frac{\partial}{\partial p^d}\left(\frac{\partial G^d}{\partial n_1^d}\right)_{T,p^d}\right]_{n_1^d}, \tag{3.11}$$

which reduces to

$$\left(\frac{\partial \mu_1^d}{\partial p^d}\right)_{T,n_1^d} = \nu_1. \tag{3.12}$$

In this last transformation, we have made use of fact that the chemical potential is just the partial molar Gibbs free energy and that $\nu_1 = (\partial V^d / \partial n_1^d)$. Eq. 3.12 can now be integrated

at constant T and fixed composition to obtain,

$$\mu_1^d(p^d, T, x_1) - \mu_1^d(p_1^{eq}, T, x_1) = \nu_1(p^d - p_1^{eq}), \tag{3.13}$$

where $x_1 = n_1^d/(n_1^d + N_2)$ is the mole fraction of component one in the drop.

Non-ideality of the solution is introduced into the model by treating component one in the droplet phase in terms of the regular solution model, which is based on the Bragg-Williams lattice approximation. This assumes that the drop mixes uniformly so the entropy of mixing is the same as the ideal solution, but the enthalpy of mixing is dependent on x_1. The chemical potential of component one at p_1^{eq}, T and x_1 is then described by

$$\mu_1^d(p_1^{eq}, T, x_1) = \mu^0 + kT \ln x_1 + b_0(1 - x_1)^2, \tag{3.14}$$

where $\mu^0 = \mu_1^d(p_1^{eq}, T, x_1 = 1)$ is the chemical potential of pure component one liquid at p_1^{eq} and b_0 accounts for the interaction between components. When b_0 is set to zero, Eq. 3.14 reduces to the expression for an ideal solution, while positive and negative values correspond to repulsive and attractive interactions respectively.

Using Eqs. 3.7, 3.13 and 3.14 in Eq. 3.4 and noting $dV^d = \nu_1 dn_1^d$ yields

$$dF = \left[\nu_1(p^v - p_1^{eq}) - kT \ln \frac{p^v}{x_1 p_1^{eq}} + \frac{2\nu_1\gamma}{R} + b_0(1 - x_1)^2\right] dn_1^d. \tag{3.15}$$

Equating the term inside the brackets of Eq. 3.15 to zero then gives us the Kelvin relation for the binary drop,

$$\frac{p^v}{p_1^{eq}} = a_1 \exp\left[\frac{2\nu_1\gamma}{kTR}\right], \tag{3.16}$$

where $a_1 = x_1 \exp[b_0(1 - x_1)^2/kT]$ is the activity of component one in the drop and the first term has been ignored because it is generally small. Reiss and Koper [74] also obtained Eq. 3.16 using a slightly less rigorous approach in an open system. Finally, Eq. 3.15 is integrated with respect to n_1^d to obtain the free energy of forming the drop,

$$\begin{aligned} \Delta F &= F(n_1^d) - F(0) \\ &= n_1^d\left[kT - \nu_1^d p_1^{eq} + b_0(1 - x_1)\right] + N_2 kT \ln(1 - x_1) \\ &+ N_1 kT \ln \tfrac{p^v}{p_1^0} - n_1^d kT \ln \tfrac{p_1^v}{x_1 P_1^{eq}} + \gamma[A^d(n_1^d) - A^d(0)], \end{aligned} \tag{3.17}$$

where $p_1^0 = N_1 kT/(V - V^d)$ is the pressure of the vapour before any particles have condensed onto the drop and the second term of the right hand side of the equation is the entropy of mixing for component two.

3.2.2 Model Analysis

To explore the general features of the free energy surface described by Eq. 3.17 as a function V and n_1^d, we use the thermodynamic parameters for argon [63] where appropriate and assume the volume per molecule of the two components is the same, giving $\nu_1 = \nu_2$. We also set $N_1 = 300$ to be consistent with the simulations of this system carried out in Section 3.4.

Fig. 3.2 summarizes the key elements of the free energy surface under different conditions. When b_0 is small or negative the entropy of mixing for the two components dominates the free energy, leading to the presence of a single free energy minimum, corresponding to the spontaneous formation of a mixed drop, for all system volumes (Fig. 3.2 (a)). As V decreases, the minimum simply moves to larger n_1^d as more vapour condenses and the drop grows. This is qualitatively the same as the ideal case, where $b_0 = 0$, but a non-zero interaction parameter shifts the value of n_1^d for the minimum to lower or higher values, compared to the ideal case, for the same V, when b_0 is positive or negative, respectively.

Figs. 3.2 (b)-(e) show that the evolution of the free energy surface as a function of volume, for a system with larger b_0, traces out a hysteresis loop similar to the one observed in the deliquescence and efflorescence of soluble salt particles. At large V, we see the spontaneous absorption of a few component one particles to form a small mixed drop. As V decreases, a minimum appears at larger n_1^d corresponding to a drop that has absorbed a significant fraction of the volatile solvent component, dissolving the non-volatile solute. Initially this minimum is metastable relative to the small drop, but it eventually becomes the most stable state at small enough volumes . The free energy minima of the small and large drops are separated by a free energy maximum that represents an unstable equilibrium solution to the Kelvin equation and the size of the drop at the maximum is the critical nucleus for the solubility transition. At smaller V, we reach the limit of stability of the non-volatile drop, causing it to dissolve spontaneously. At this point, the drop becomes activated in the sense described by Köhler theory.

For large N_2, the free energy surface is once again characterized by a single broad minimum (Fig. 3.2 (f)) as the entropy of mixing again becomes the most dominant term in the free energy. As the initial size of the non-volatile drop decreases, the minimum in the free energy for the small drop moves to smaller n_1^d and becomes shallower. In the limit of $N_2 \to 0$ Eq. 3.17 reduces to the free energy expression for the original homogeneous liquid drop model [62].

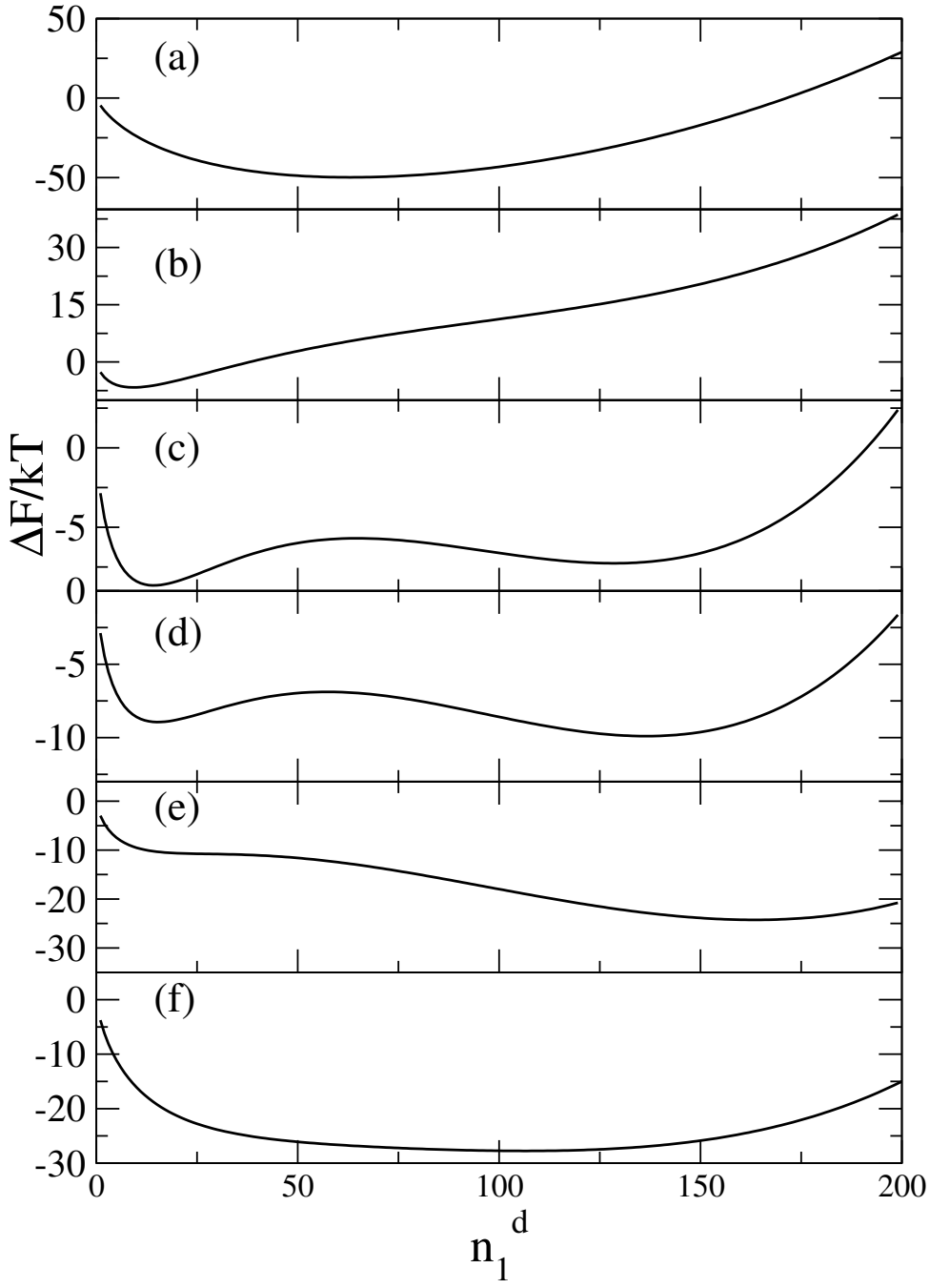

Figure 3.2: Free energy landscape as a function of n_1^d for a droplet with (a) $b_0 = 0$, $N_2 = 100$, $V/\sigma^3 = 30000$. For droplets with $b_0 = 3$ and $N_2 = 100$ at (b) $V/\sigma^3 = 12000$, (c) $V//\sigma^3 = 10000$, (d) $V/\sigma^3 = 9800$, (e) $V/\sigma^3 = 8900$, and (f) $N_2 = 200$, $V/\sigma^3 = 10000$.

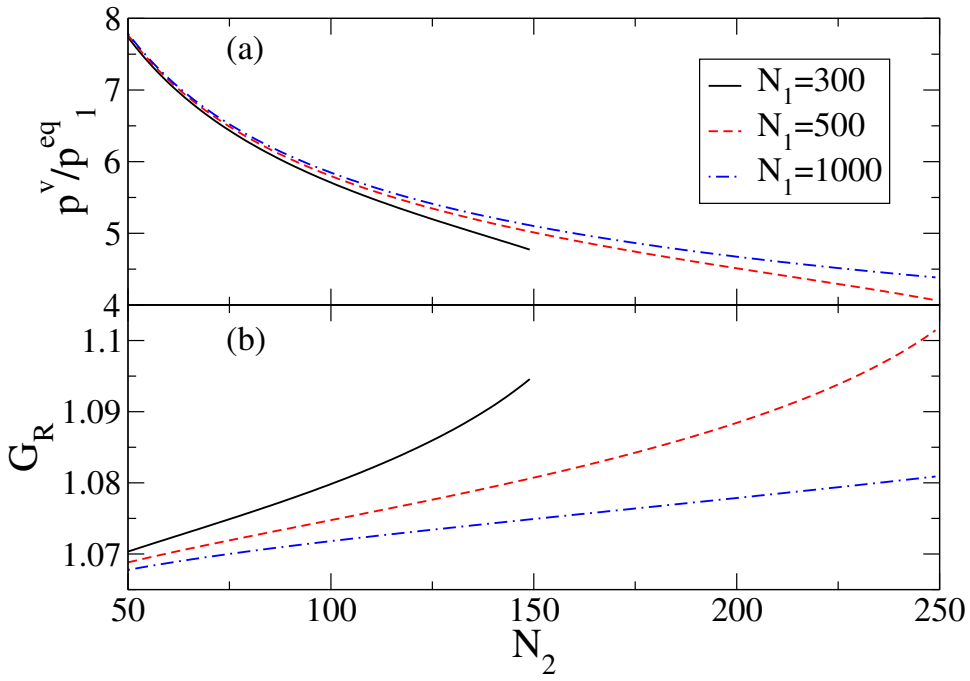

Figure 3.3: (a) The vapour pressure for the drop, given by Eq. 3.16, at the activation point as a function of N_2 for different number of initial values of N_1. (b) Growth factor, G_R of the drop at the activation point as a function of N_2.

In an open system, Köhler's theory of activation identifies the location of the transition as the supersaturation at which the small drop becomes unstable and grow spontaneously. To study the effect of the size of the non-volatile droplet on the location of the activation point in the modified liquid drop model, we note that the limit of stability for the drop must satisfy the conditions $\partial F/\partial n_1^d = 0$, and $\partial^2 F/\partial n_1^{d2} = 0$. We then plot the supersaturation of the vapour surrounding the drop, p^v/p_1^{eq}, as given by the Eq. 3.16, at the activation point, as a function of N_2 (see Fig. 3.3 (a)). The results of the model are mildly dependent on N_1 because as the droplet grows, but these effects decrease as the system size increases. Nevertheless, the supersaturation of the activation point increases as the size of the 'dry' drop decreases, which is consistent with the general trends of Köhler activation. We also see that the growth factor of the drop, $G_R = R/R_0$ where R_0 is the size of the pure non-volatile drop, decreases with decreasing N_2 (Fig. 3.3 (b)) which is consistent with capillarity based model

of deliquescence [22] and experiment [26, 81, 82]. However, Talanquer and Oxtoby [32], found DFT predicts that G_R, at the solubility transition, increases as the size of soluble particle decreases.

3.2.3 Nucleation Barriers

While activation theory successfully describes the location of the transition in large drops, nucleation becomes an increasing important mechanism for droplet growth as the particle size decreases [28, 31, 78] and we would expect the transition to occur at lower vapour pressures because droplets can get over the barrier in an activated process before the limit of stability is reached. Classical nucleation theory, (CNT) gives the rate of drops going over the barrier as

$$J = A \exp(-\Delta F^*/kT), \tag{3.18}$$

where $\Delta F^*/kT$ is the height of the free energy barrier associated with forming the critical droplet and A is the pre-exponential factor containing information about the dynamics. However, CNT, was developed under assumptions that the barrier is high relative to the thermal energy in the system, kT, but the barriers associated with the growth of non-volatile, soluble droplets are generally small so it then becomes questionable whether CNT is applicable to these systems.

Fig. 3.4 shows the free energy of forming a drop containing n_1^d particles of the volatile solvent from a drop containing no solvent particles as given by Eq. 3.17 and focusing on the region near the barrier. For a system with $N_2 = 75$, $N_1 = 300$ and $V = 9000\sigma^3$, the small drop has only just become metastable with respect to the large drop, which appears at much larger n_1^d and is not shown. The value of $\Delta F(n^*)/kT$, where n^* represents the value of n_1^d at the top of the barrier, is actually negative, which suggests it is more stable than dry droplet, but this does not mean the drop spontaneously grows. When the free energy surface contains a local minimum, the free energy barrier used in Eq. 3.18 is usually defined as the difference in free energy between the maximum and the minimum,

$$\Delta F_{mm} = \Delta F(n^*) - \Delta F(n_m), \tag{3.19}$$

where n_m denotes the value of n_1^d at the minimum. For this case, ΔF_{mm} is only a few kT and decreases as V is decreased. In particular, $\Delta F_{mm} \to 0$ at the limit of stability, which fits our intuitive understanding of activated processes.

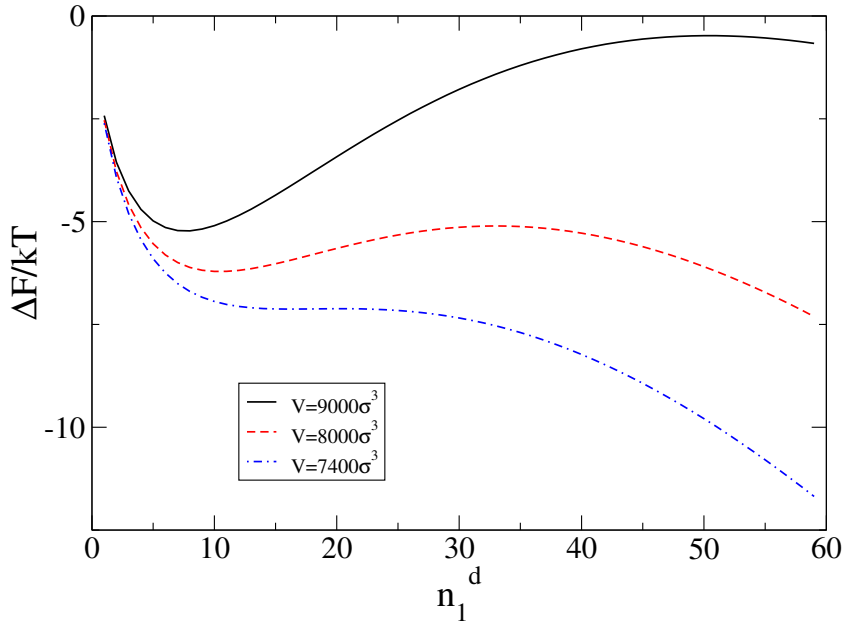

Figure 3.4: Model free energy from Eq. 3.17, with $N_2 = 75$ and $N_1 = 300$, showing the nucleation barrier and limit of stability.

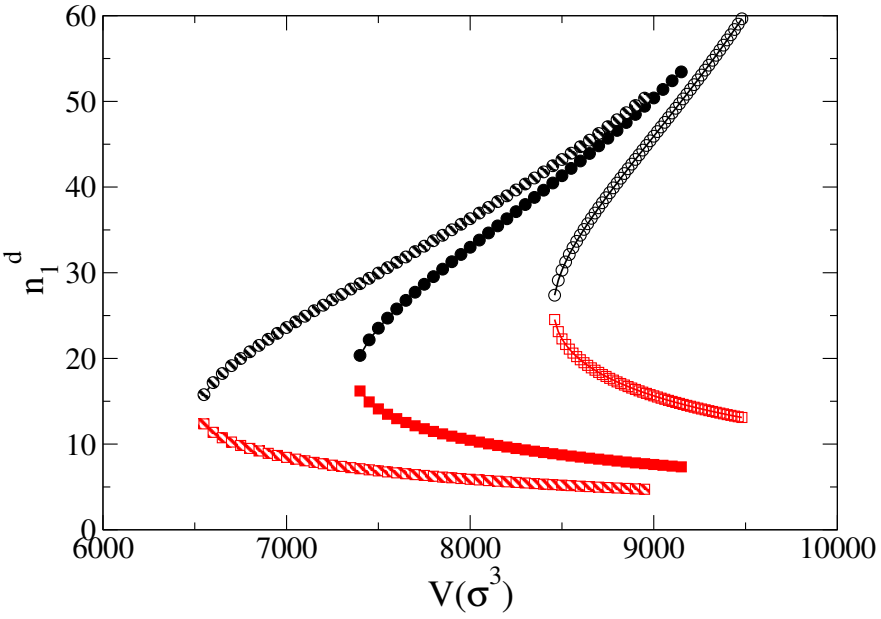

Figure 3.5: The number of solvent atoms in the droplet at the free energy minimum, n_m (squares) and at the free energy maximum, n^* (circles) for droplets with $N_2 = 100$ (open symbols), $N_2 = 75$, (filled symbols) and $N_2 = 50$ (striped symbols).

Fig. 3.5 shows n^* and n_m for systems with different size non-volatile particles. For each N_2, n^* and n_m approach one another and converge at the limit of stability. These plots show that the range of V over which the small mixed drop is metastable decreases for increasing N_2, which helps explain why nucleation becomes more important as the non-volatile particle get smaller. When N_2 is large, a small change in V, or supersaturation in an open system, will rapidly move the system beyond its limit of stability, while the smaller non-volatile particles require much larger changes in V.

However, while the free energy barrier defined by Eq. 3.19 fits our intuitive notions of metastability, recent work by Scheifele et al. [18] showed that $\Delta F_{mm}/kT$ did not correctly predict the rate for the heterogeneous nucleation of the two dimensional Ising model onto a nanoscale impurity. The free energy landscape for their system exhibits a minimum similar to that found in our non-volatile liquid drop model and their work highlights the fact that the exponential term in the rate is really a surrogate for the probability of finding the metastable drop at the transition state, $P(n^*)$. The free energy that provides the probability of finding a drop containing n_1^d particles can be expressed

$$\Delta F_0(n_1^d)/kT = -\ln P(n_1^d) = -\ln \frac{Q(n_1^d)}{Q(\text{met})}, \tag{3.20}$$

where $Q(n_1^d)$ is the partition function of the drop mixed drop with n_1^d and $Q(\text{met})$ is the partition function of the metastable system,

$$Q(\text{met}) = \sum_{n_1^d=0}^{n_1^d=n^*} Q(n_1^d). \tag{3.21}$$

The free energy that should appear in the rate expression is then given by $\Delta F_0(n^*)/kT$ and represents the work required to constrain the metastable droplet to the its critical size.

In the context of the thermodynamic, capillarity based model developed here, $\Delta F_0(n_1^d)/kT$ can be calculated by renormalizing the free energy given by Eq. 3.17, so that

$$P(n_1^d) = \frac{\exp(-\Delta F(n_1^d)/kT)}{\sum_{n_1^d=0}^{n_1^d=n^*} \exp(-\Delta F(n_1^d)/kT)}, \tag{3.22}$$

which ensures $\sum_{n_1^d=0}^{n_1^d=n^*} P(n_1^d) = 1$. $\Delta F_0(n_1^d)/kT$ can then be obtained from the left hand equality in Eq. 3.20. Implicit in Eq. 3.22, is the assumption that the capillarity model, which gives rise to $\Delta F(n_1^d)$, describes all the microscopic states of the partition function $Q(n_1^d)$.

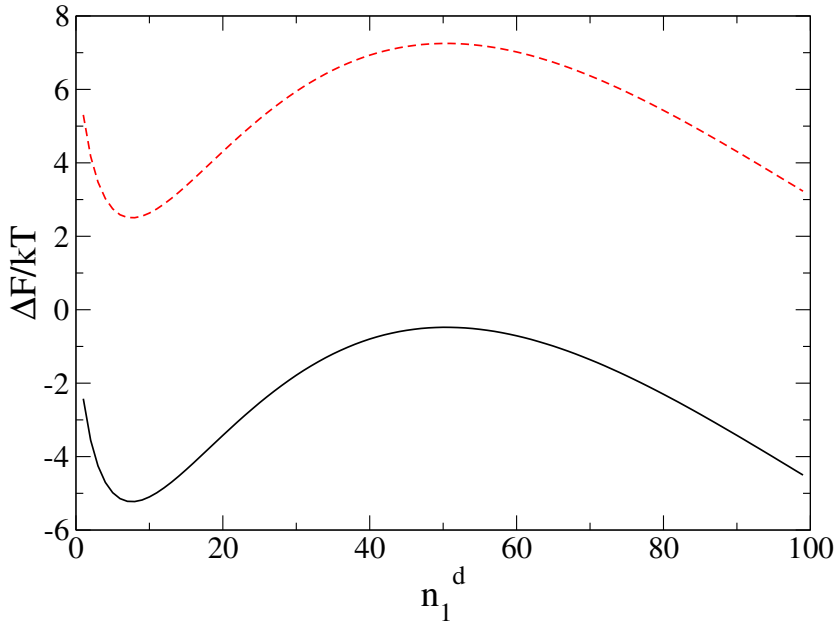

Figure 3.6: The free energy before (solid line) and after (dashed line) renormalization for nucleation.

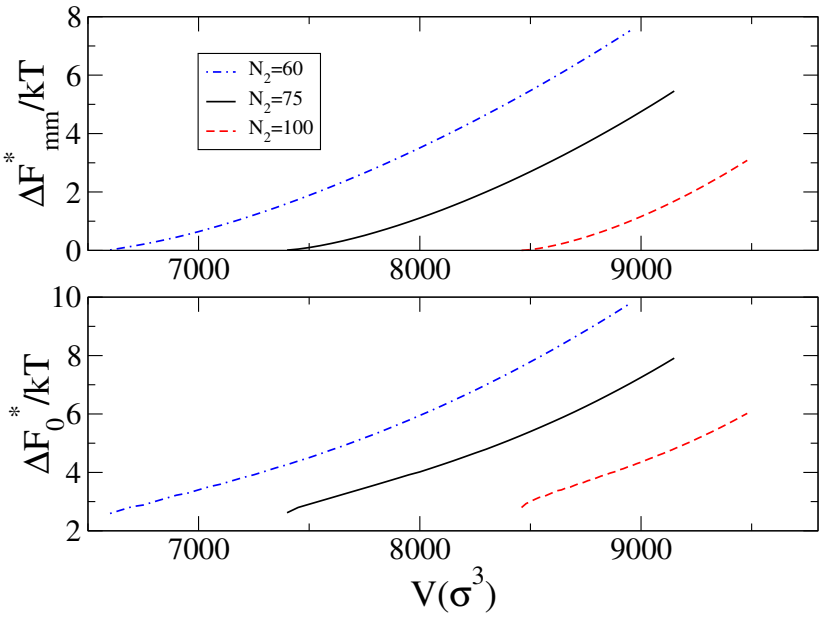

Figure 3.7: Nucleation barriers calculated using (top) the difference in free energy from maximum to minimum, $\Delta F^*_{mm}/kT$, and (bottom) the renormalized free energy $\Delta F^*_0/kT$, as a function of V for systems with $N_2 = 60, 75$ and 100.

Fig. 3.6 shows that the effect of the renormalisation is to shift the free energy curve vertically, without changing its shape because the denominator in Eq. 3.22 results in a constant term that is applied to the free energy of all the states. $\Delta F_0(n_1^d)/kT)$ is positive for all the drop sizes in the metastable region since it always takes work to constrain the system to the subset of states, but the values for $n_1^d > n^*$ have no real meaning because they are connected to the stable state and have not been included in the metastable drop partition function. A comparison of the nucleation free energy barriers predicted by Eq. 3.19 and Eqs. 3.20-3.22 (see shows Fig. 3.7) that $\Delta F_0^*/kT$ is generally $2-3\ kT$ higher than the minimum to maximum barrier which can lead to orders of magnitudes difference in the nucleation rates predicted by the two definitions.

$\Delta F_0^*/kT$ also remains finite at the limit of stability. This seems counter intuitive because we associate a positive free energy barrier with an activated process, but at the limit of stability the free energy landscape is monotonically decreasing from $n_1^d = 0$ so the drop grows spontaneously. This remains true, even after renormalization. However, in reality, the metastable region ceases to be defined at the limit of stability and the barrier is only defined as the limit of stability is approached from above. The finite barrier is then a result of the fact that $n^* \to n_n$ at a finite value of n_1^d, because of the minimum in the free energy.

Despite this unusual property, Scheifele et al. [18] showed that the free energy given by Eq. 3.20 correctly predicts the rate of nucleation right down to the limit of stability for their heterogeneous nucleation case. While we do not have any independent rate data to test in our current model, it seems reasonable to suggest the renormalization of the barrier described for the non-volatile liquid drop model would be necessary.

3.3 Lattice Gas Model for Monolayer Adsorption on a Nanoparticle

In this section, we develop a simple lattice gas model in three dimensions to describe the absorption of a monolayer of a vapour phase onto a nanoparticle in a closed system. Fig. 3.8 shows a two-dimensional representation of the model which consists of N particles in a cubic container of m equivalent lattice sites with periodic boundaries in all directions. A cubic nanoparticle, with sides of length l sites, occupies the l^3 sites at the center of the container

and these sites are not accessible to the particles. Particles only interact with each other by excluding volume so each lattice site can only be occupied by a single particle. Particles adsorb onto the nanoparticle with an energy ϵ and occupy sites adjacent to the face of the nanoparticle.

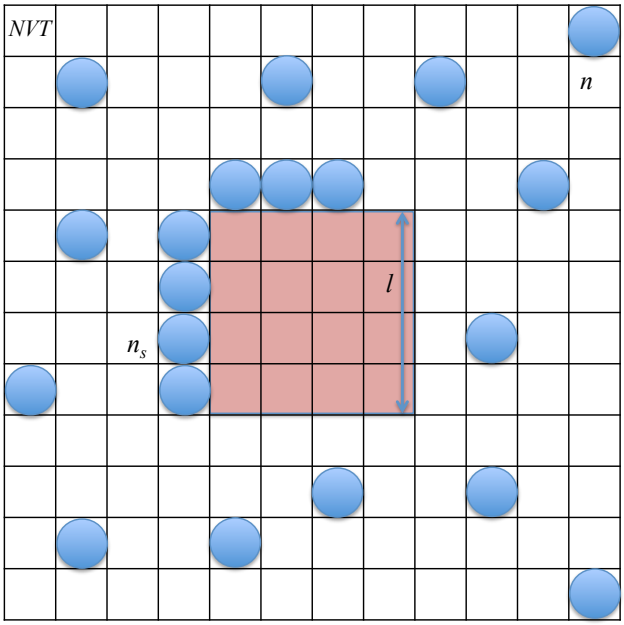

Figure 3.8: Schematic representation of the lattice gas model. n is the total number of gas particles, n_s is the total number of gas particles condensed on the nanoparticle and l is the size of the nanoparticle.

The general form of the canonical ensemble partition function can be written

$$Q(N, V, T) = \sum_v e^{-\beta E_v}, \tag{3.23}$$

where the sum is over all possible states of the system and E_v is the energy of state v. However, we are interested in calculating the average number of particles adsorbed on the surface, n_s, and the analysis is simplified if we note that the sum in Eq. 3.23 is dominated by the maximum term. We can then write a restricted partition function for all the states with n_s adsorbed particles and find the value of n_s that minimizes the free energy. This restricted partition function can be written,

$$Q(n_s) = \frac{m_g!}{n_g!(m_g - n_g)!} \frac{m_s!}{n_s!(m_s - n_s)!} e^{-n_s\epsilon/kT}, \tag{3.24}$$

where $m_g = m - (l^3 + 6l^2)$ is the number of sites accessible to the $n_g = N - n_s$ particles remaining in the vapour phase and $m_s = 6l^2$ is the total number of possible adsorption sites.

The first term in Eq. 3.24 represents the number of ways we can place n_g particles in the m_g sites and the second terms gives us the number of ways of distributing the n_s adsorbed particles over the m_s sites.

The Helmholtz free energy is then given by

$$\frac{F(n_s)}{kT} = -\ln Q(n_s). \tag{3.25}$$

However, this expression can be simplified further by using Stirling's approximation for the logarithm of the factorial terms, which then yields

$$\begin{aligned} \frac{F(n_s)}{kT} &= m_g \ln(m_g) - n_g \ln(n_g) - (m_g - n_g)\ln(m_g - n_g) \\ &+ m_s \ln(m_s) - n_s \ln(n_s) - (m_s - n_s)\ln(m_s - n_s) - n_s\epsilon. \end{aligned} \tag{3.26}$$

Fig. 3.9 compares $\Delta F/kT = F(n_s)/kT - F(0)/kT$, the free energy of adsorbing n_s particles on the surface relative to the dry nanoparticle, obtained from Eq. 3.25 with that obtained from Eq. 3.26. Using the Stirling approximation results in a deeper free energy minimum but the values of n_s at the minimum, which gives us the number of adsorbed particles at equilibrium, are very similar.

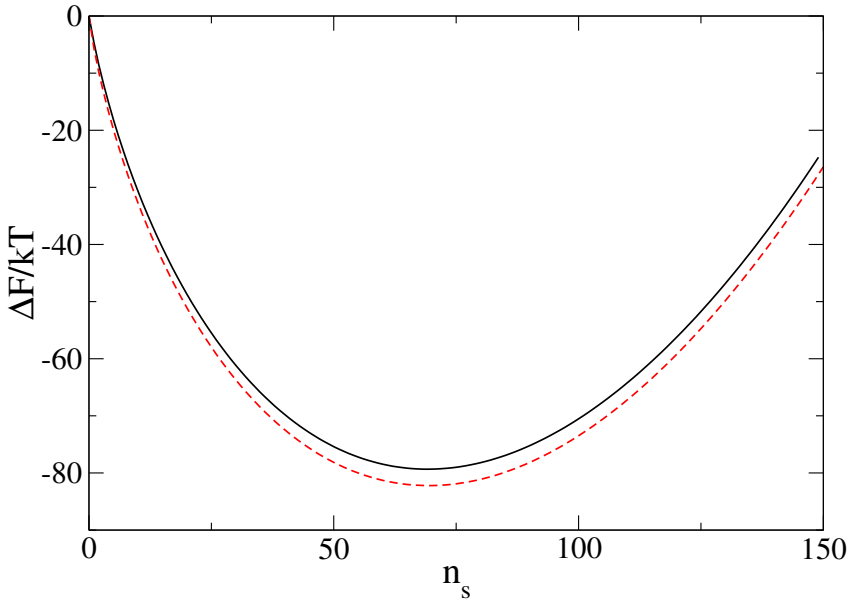

Figure 3.9: $\Delta F/kT$ using Eq. 3.25 (solid line) and Eq. 3.26 (dashed line) as a function of n_s for a system with $l = 12$, $\epsilon/kT = -1$ and $m = 10000$.

The advantage of using Eq. 3.26 is that we can obtain an analytical expression for the number of adsorbed particles. At equilibrium, $\partial F/\partial n_s = 0$, then solving for n_s gives,

$$\begin{aligned} n_s(n;l;m;\epsilon) &= \frac{-6l^2-n+e^{\epsilon}\left(l^3+6l^2-m+n\right)}{2(e^{\epsilon}-1)} \\ &+ \frac{\sqrt{24l^2n(e^{\epsilon}-1)+(6l^2+n+e^{\epsilon}(-l^3-6l^2+m-n))^2}}{2(e^{\epsilon}-1)}, \end{aligned} \tag{3.27}$$

where we have selected the positive root as the physically relevant solution. Fig. 3.10 shows the fraction of adsorption sites occupied by particles, $\theta_{abs} = n_s/m_s$, as a function of the volume m, again comparing the results with (Eq. 3.27) and without Stirling's approximation. They remain close over the entire range of volumes with the discrepancy increasing as the volume increases and the number of adsorbed particles becomes small. Finally, Fig 3.11 shows the adsorption isotherms for different size nanoparticles obtained using Eq. 3.27. The curves for the larger nanoparticles increase more rapidly as the volume decreases because the larger particles occupy more volume which leads to a higher effective pressure in the vapour phase at a given m. The increased vapour pressure favours adsorption.

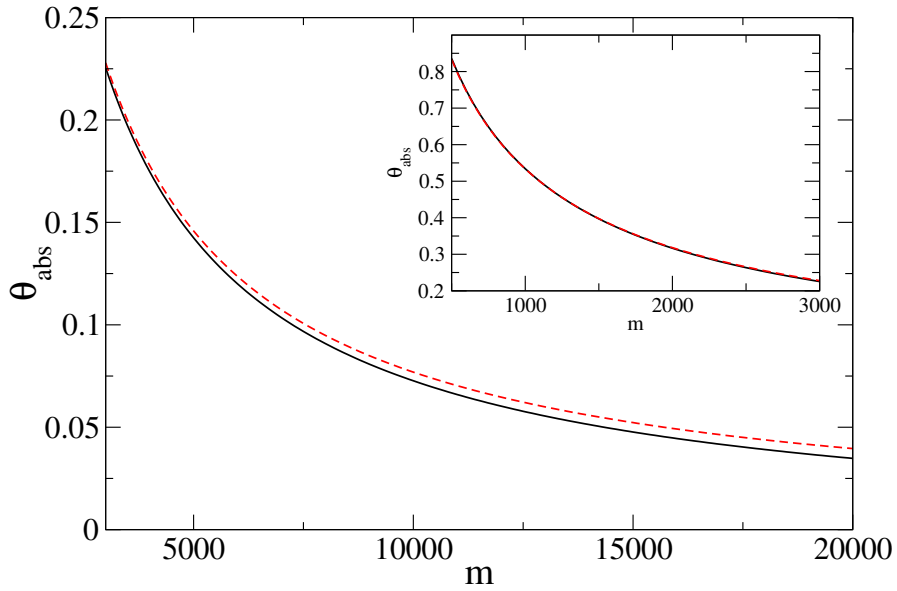

Figure 3.10: The fraction of adsorption sites occupied by particles, $\theta_{abs} = n_s/m_s$, as a function of the volume m, ($l = 4$).

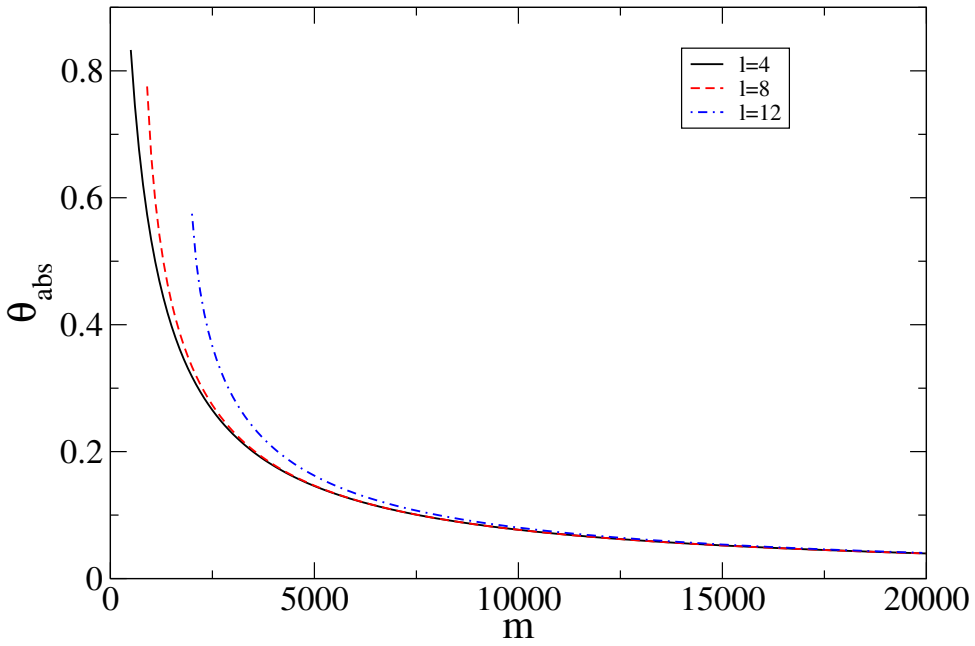

Figure 3.11: The adsorption isotherms for different size nanoparticles obtained using Eq. 3.27.

3.4 Simulations and Results

3.4.1 Simulation Details

We use MD simulations in the canonical ensemble to study the condensation of a vapour onto a liquid nanodrop. The composite system, vapour and droplet, is modelled using a binary mixture of Lennard - Jones particles interacting through the potential,

$$U(r_{ij}) = 4\epsilon_{ij}\left[(\sigma_{ij}/r_{ij})^{12} - (\sigma_{ij}/r_{ij})^{6}\right], \tag{3.28}$$

where ϵ_{ij} is the energy interaction parameter between species i and j, σ_{ij} is the particle size interaction between species and the potential is cut, but not shifted, at half the box length. The simulation cell is cubic and we employ periodic boundary conditions. Denoting the volatile solvent and the non-volatile solute as components one and two respectively, we set $\epsilon_{11} = 1.0$, $\epsilon_{22} = 2.0$ and $\sigma_{11} = \sigma_{22} = \sigma_{12} = 1.0$, then vary ϵ_{12} to control the miscibility of

the components. The energy of mixing parameter,

$$\Lambda^* = (\epsilon_{11} + \epsilon_{22} - 2\epsilon_{12})/\epsilon_{11} \ . \tag{3.29}$$

provides a measure of the energetic drive force for mixing. When $\Lambda^* < 0$, particle interactions favor mixing, otherwise they promote phase separation and we study systems with $\Lambda^* = -0.1$ and $\Lambda^* = 0.172$. The ratio $\epsilon_{22}/\epsilon_{11}$ controls the relative volatility of the components and we have chosen parameters consistent with the DFT model [32] where the supersaturation of the non-volatile phase was 10^5 times smaller than that of the vapour. The number of volatile particles, $N_1 = 300$, is maintained for all simulations and we study droplets with $N_2 = 75, 100$ and 150. Our simulations are carried out using the Gromacs 4.0 Package [65], where the leap frog integration scheme, with a step size of $\Delta t^* = 0.002$, is employed to evolve the equations of motion. The velocity rescaling thermostat is used to maintain the system at a reduced temperature, $T^* = kT/\epsilon_{11} = 0.8$, where k is the Boltzmann constant. All quantities are reported in reduced units.

Cluster criteria that allow us to follow the evolution of the droplet as a function of time were developed by measuring the nearest neighbour distributions in both the pure volatile vapour system and in the isolated pure component two droplet phase. Particles of the vapour were initially placed randomly in the simulation cell, with the restriction that no two particles were closer than $1.5\sigma_{11}$, then the system was equilibrated for 10^6 time steps before configurations were sampled every 10000 time steps for up to 10^7 time steps. Simulations of the isolated droplet were initialized with a compact BCC cluster and allowed to equilibrate for 10^7 time steps. Configurations were then sampled in the same way as the vapour. Fig. 3.12 shows fraction of particles with a given number of neighbours within $1.5\sigma_{11}$ for both phases. The distribution of the droplet phase exhibits two distinct peaks that were decomposed into distributions associated with particles at the core of the droplet and those on the surface, using the cone [83] method to identify surface atoms. Most core particles have 12 neighbours, which is consistent with the nearest neighbour distribution of the bulk Lennard-Jones fluid with $\epsilon_{ii} = 1$, but the core distribution measured here is more narrow because our non-volatile component has a stronger $\epsilon_{22} = 2$. The distribution for the surface atoms peaks at seven nearest neighbours and marginally overlaps the distribution of the vapour phase, which has no particles with more than three neighbours. On the basis of these results, we identify liquid-like particles as those with three or more neighbours and consider two particles to be

part of the same liquid cluster if they are neighbours.

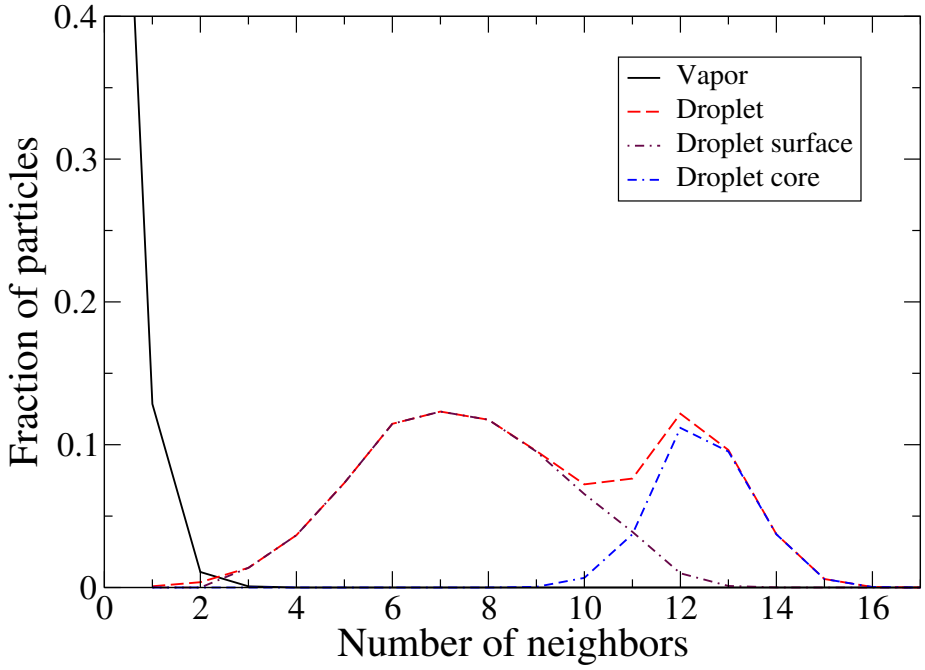

Figure 3.12: Neighbour distribution for particles in the vapour and droplet phase.

Throughout our simulations we follow three cluster based quantities: i) the size of the droplet, which is taken to be the largest cluster of liquid-like particles in the system and can contain both components, ii) the total number of component one particles in this largest cluster, and iii) the size and number of component one clusters that are part of the largest droplet. At each volume, V, studied, we generate the starting configuration by initially equilibrating the isolated component 2 droplet in the container, then sequentially add the component one particles to the system in random locations, ensuring they are not closer than $1.5\sigma_{11}$ to any other particle. Simulations were then run for 10^8 time steps. We also measure the equilibrium radial density distribution of each of the components in the droplet from the centre of mass of the droplet.

3.4.2 Simulations Results

In the absence of the vapour phase, the pure component two droplets with $N_2 = 100$ and 150 remain stable over the entire volume range studied and we only see the evaporation of five to six particles from the droplet at the largest volumes studied, confirming that the strong ϵ_{22} interaction keeps the volatility of the droplet low. The $N_2 = 75$ droplet begins to show significant evaporation above $V/\sigma^3 = 3 \times 10^5$ and these volumes are not included in our study.

In the presence of vapour, the growth of the drop exhibits two distinct time trajectories depending on the volume of the system. Fig. 3.13 shows that when V is large the size of the droplet only increases by a small amount and the vapour essentially remains stable, this also can be seen in Fig. 3.14 where starting configuration (left) and end configuration (right) for $V/\sigma^3 = 2 \times 10^5$, here green represent the initial droplet particles and ice blue is for vapour particles. The growth occurs rapidly, then the droplet fluctuates around its equilibrium size, losing and gaining component one particles in a dynamic equilibrium with the vapour phase. Fig. 3.14 (right) and Fig. 3.15 clearly shows that the component one particles are mainly located in the surface region of the droplet. Furthermore, the radial density distributions (Fig. 3.16 (a) and (c)) confirms it with a small amount of mixing into the core of the droplet when $\Lambda = -0.1$. However, there are not enough particles to form a complete monolayer and we see an equilibrium number of component one liquid clusters distributed over the complete cluster surface. This is observed for both values of Λ^* studied. Clarke et al. [84] also observed the submonolayer wetting of droplets in their study of the phase diagram for equimolar binary Lennard-Jones clusters for similar interaction parameters.

The fluctuations in the size of the largest component one liquid clusters also correlate with the fluctuations in the total size of the droplet suggesting these clusters grow and shrink by gaining and losing particles to the vapour, although some coalescence between clusters on the droplet surface is likely to occur.

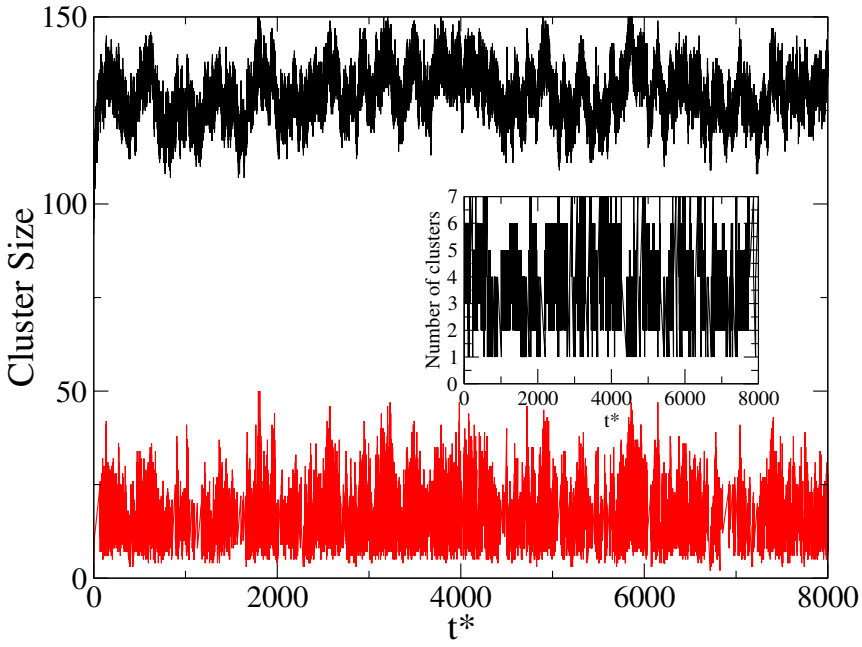

Figure 3.13: Size of the droplet (black line) and size of the largest component one cluster attached to the droplet (red line) for a system with $N_2 = 100$, $\Lambda^* = 0.172$ at $V/\sigma^3 = 2 \times 10^5$ as a function of reduced time $t^* = 2 \times 10^{-3}$. Inset: Number of clusters of component one attached to drop.

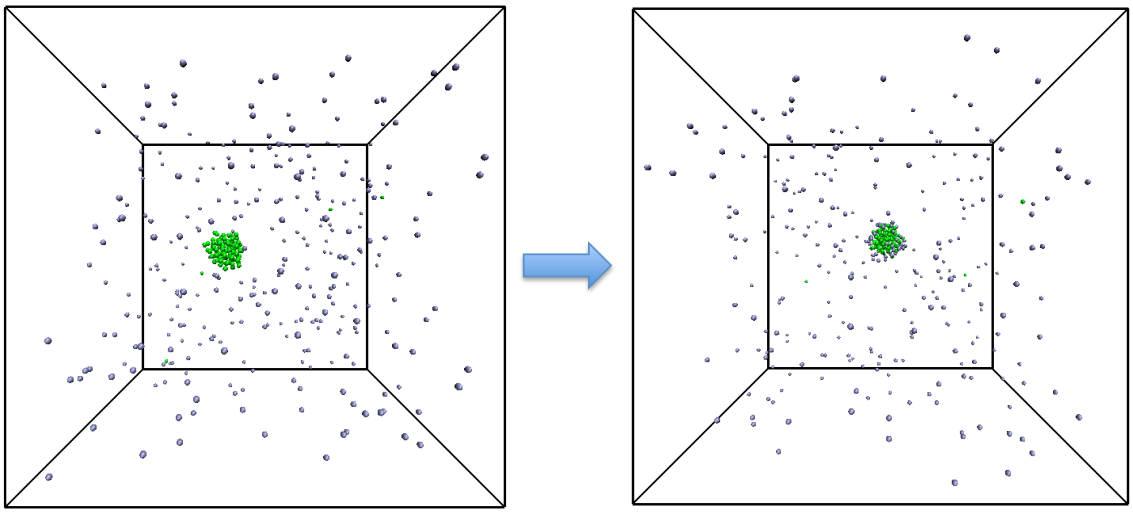

Figure 3.14: Snapshots for a system with $N_2 = 100$, $\Lambda^* = 0.172$ at $V/\sigma^3 = 2 \times 10^5$. Initial configuration (left) and end configuration (right). Green color is initial droplet particles, while ice blue is for the vapour particles.

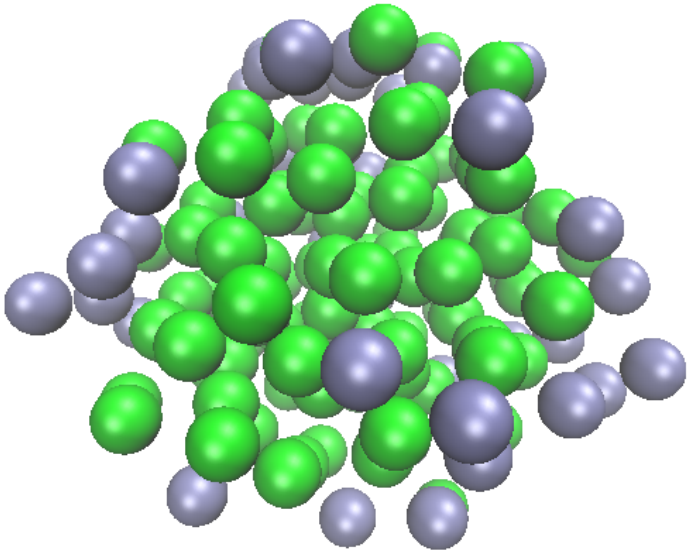

Figure 3.15: Snapshot for just the drop with $N_2 = 100$, $\Lambda^* = 0.172$ at $V/\sigma^3 = 2 \times 10^5$, vapour particles are not shown. Component 1 (green), condensed vapour particles (component 2) (ice blue).

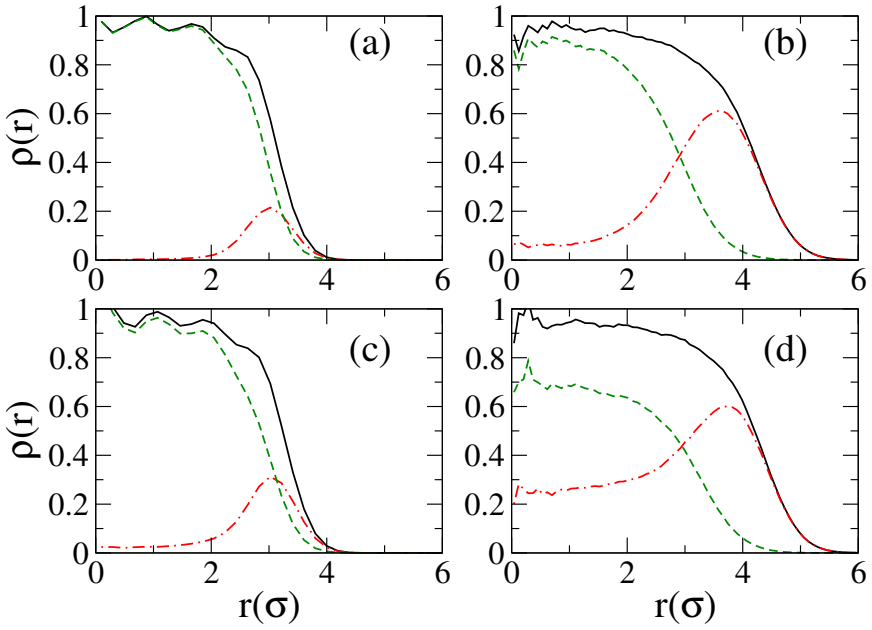

Figure 3.16: Radial density distributions for the complete droplet (black solid line), component one (red dot-dashed line) and component two (green dashed line) for (a) $\Lambda^* = 0.172$, $V/\sigma^3 = 2 \times 10^5$, (b) $\Lambda^* = 0.172$, $V/\sigma^3 = 1.5 \times 10^4$, (c) $\Lambda^* = -0.1$, $V/\sigma^3 = 2 \times 10^5$ and (d) $\Lambda^* = -0.1$, $V/\sigma^3 = 1.5 \times 10^4$.

When V is decreased, the vapour spontaneously condenses onto the droplet, causing it to grow. Fig. 3.17 shows the growth of the droplet, the growth of the largest component one cluster and the number of component one clusters on the drop as a function of time (Inset). Fig. 3.18 shows the initial (left) and end (right) configuration with $N_2 = 100$, $\Lambda^* = 0.172$ at $V/\sigma^3 = 1.5 \times 10^4$ and Fig. 3.19 illustrates just the drop for the same system and the drop (green) is totally covered by the component one particles (ice blue). The initial condensation onto the droplet leads to a rapid increase in the number and size of component one liquid clusters on the surface of the droplet, but the limited surface area means that the clusters start to interact. In particular, we note that the large fluctuations in the size of the largest component one liquid cluster on the droplet are decoupled from the fluctuations in the total size of the droplet, indicating clusters on the surface are coalescing and breaking up again as the film grows. For example, Fig. 3.20 is a snapshot for the same system showing the different clusters of condensed vapour particles. Cluster sizes of the component one on the surface ranging from 1 particle to 11 particles on this snapshot and each of these cluster satisfy our cluster criteria and are shown with different colors. Eventually, the fluctuations decrease as all the clusters grow and coalesce to form a single cluster representing the completed film (Fig. 3.19). The droplet is unable to grow indefinitely because total number of component one particles in the simulation container remains fixed in the canonical ensemble and the vapour pressure necessarily decreases until a new equilibrium is established with the enlarged droplet.

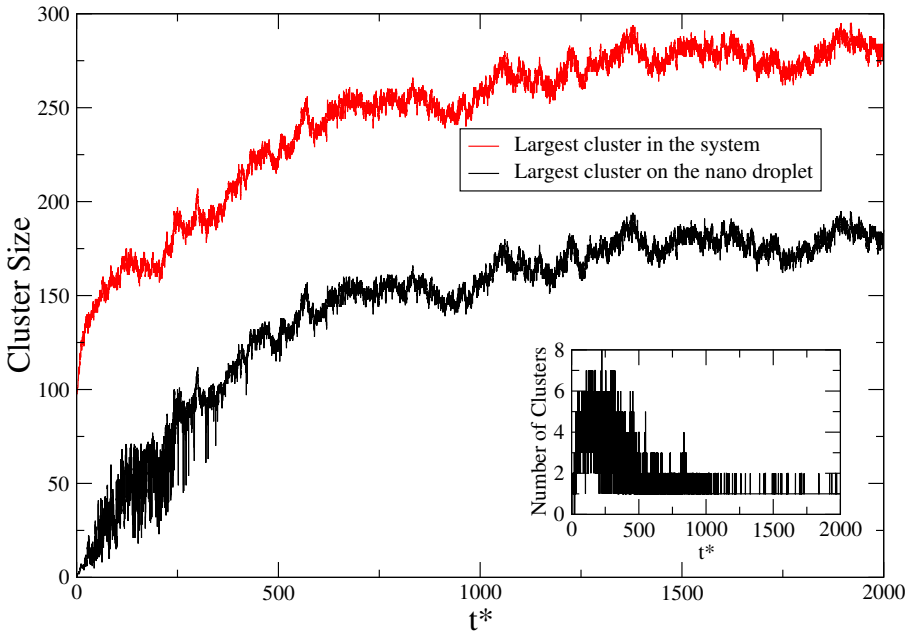

Figure 3.17: Size of the droplet (black line) and size of the largest component one cluster attached to the droplet (red line) for a system with $N_2 = 100$, $\Lambda^* = 0.172$ at $V = 1.5 \times 10^4$ as a function of reduced time $t^* = 2 \times 10^{-3}$. Inset: Number of clusters of component one attached to drop.

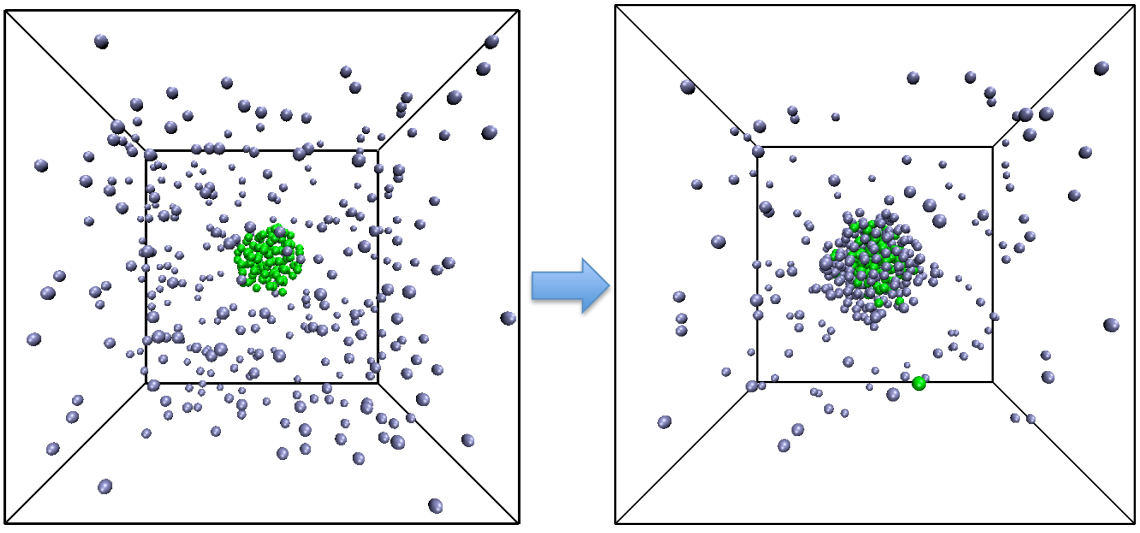

Figure 3.18: Snapshots for a system with $N_2 = 100$, $\Lambda^* = 0.172$ at $V = 1.5 \times 10^4$. Initial configuration (left) and end configuration (right).Initial droplet (green), vapour particles (ice blue).

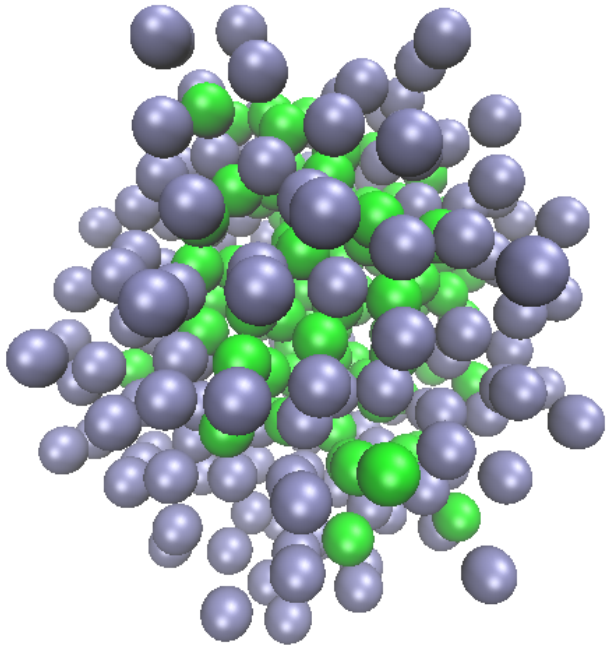

Figure 3.19: Snapshot for just the drop with $N_2 = 100$, $\Lambda^* = 0.172$ at $V = 1.5 \times 10^4$, vapour particles are not shown. Component 1 (green), condensed vapour particles (component 2) (ice blue).

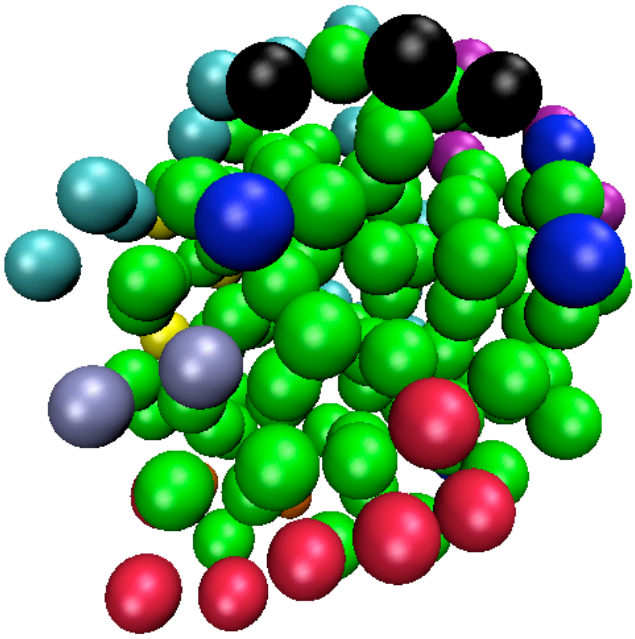

Figure 3.20: Snapshot for just the drop with $N_2 = 100$, $\Lambda^* = 0.172$ at $V = 1.5 \times 10^4$. Different clusters of component one are shown with different colors , and vapour particles are not shown. Initial droplet (green), condensed vapour particles clusters (ice blue, light blue, blue, black, red purple, and yellow).

The value of Λ^* has a strong influence on the distribution of the components in the droplet with the radial density distributions (Fig. 3.16) showing that lower values of the mixing parameter lead to greater mixing in the core of the droplet. However, even with $\Lambda^* < 0$, which represents the point where mixing should be energetically favourable, we see a significant degree of surface enrichment of the volatile solvent at the drop-vapour interface. Figs. 3.21 and Figs. 3.22 show the number of component one particles contained in the droplet, n_1^d, as a function of the volume of the system. The droplets formed from the miscible mixture generally grows larger than the partially miscible mixture for drops of the same size and the larger drops also grow more than the smaller ones, as we might expect. For all systems studied, n_1^d varies continuously over the full range of V studied.

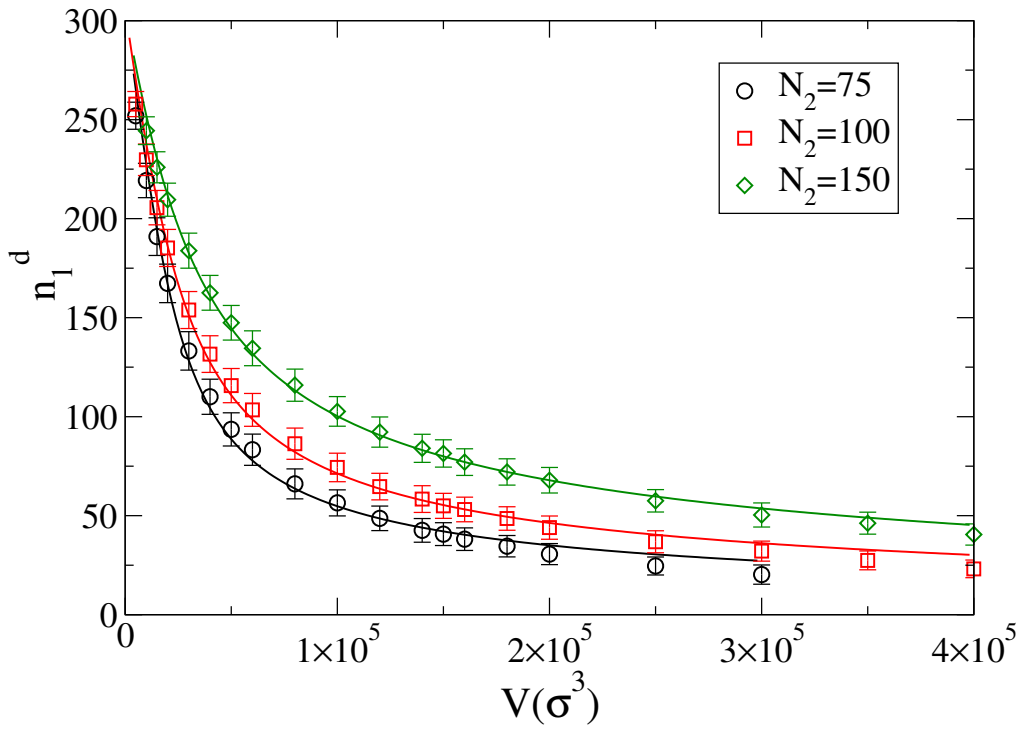

Figure 3.21: n_1^d as a function of V for non-volatile droplets with $\Lambda^* = -0.1$ and sizes $N_2 = 75, 100$ and 150. The error bars represent the standard deviation of n_1^d and the solid line are the best fits to the data using the non-volatile liquid drop model described in Section III.

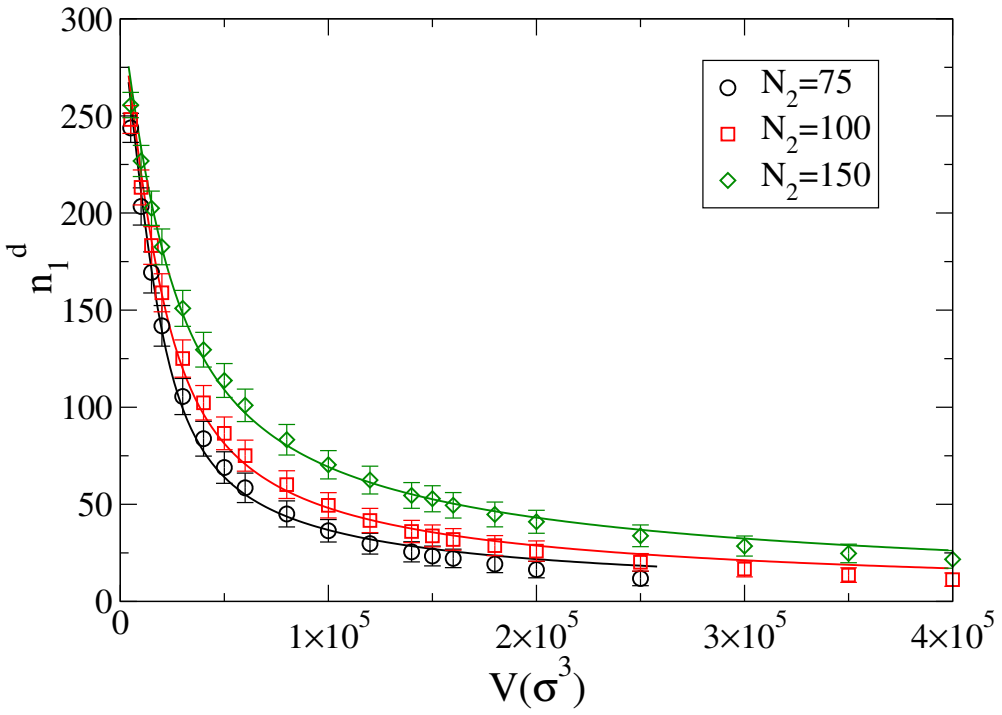

Figure 3.22: n_1^d as a function of V for non-volatile droplets with $\Lambda^* = 0.172$ and sizes $N_2 = 75, 100$ and 150. The error bars represent the standard deviation of n_1^d and the solid line are the best fits to the data using the non-volatile liquid drop model described in Section III.

One of the key challenges we face in studying these systems is defining and identifying contributions to n_1^d that arise from adsorption of component one at the non-volatile droplet surface and the mixing of components in the drop. To make this distinction, we measure the extent of mixing into the core of the drop by plotting the density of component one at the core of the drop $\rho_1(r = 0)$, obtained from measuring the equilibrium density profiles at $r = 0$, as a function of V in Fig. 3.23. For $\Lambda^* = -0.1$, $\rho_1(r = 0) > 0$ at all V and varies continuously, indicating the components always mix to some degree. However, we see a change in the N_2 dependence of $\rho_1(r = 0)$ compared to that observed for n_1^d in Figs. 3.21 and 3.22. Larger non-volatile drops have a higher component one core density when V is large, but the core density of the smaller drops increases faster as V decreases, leading to an inversion of the $\rho_1(r = 0)$ dependence on N_2, with small drops having greater core densities. The same trend is observed for cases with $\Lambda^* = 0.172$ at small system volumes, but at $V/\sigma^3 > 1.5 \times 10^5$ the

core density goes to zero, which suggests that the n_1^d particles found in the drop at these volumes can be described as being surface adsorbed. The penetration of component one into the core of the particle, below a specific volume, occurs once more than a monolayer of material is condensed onto the drop and suggests the presence of a solubility transition as a function of volume of the system.

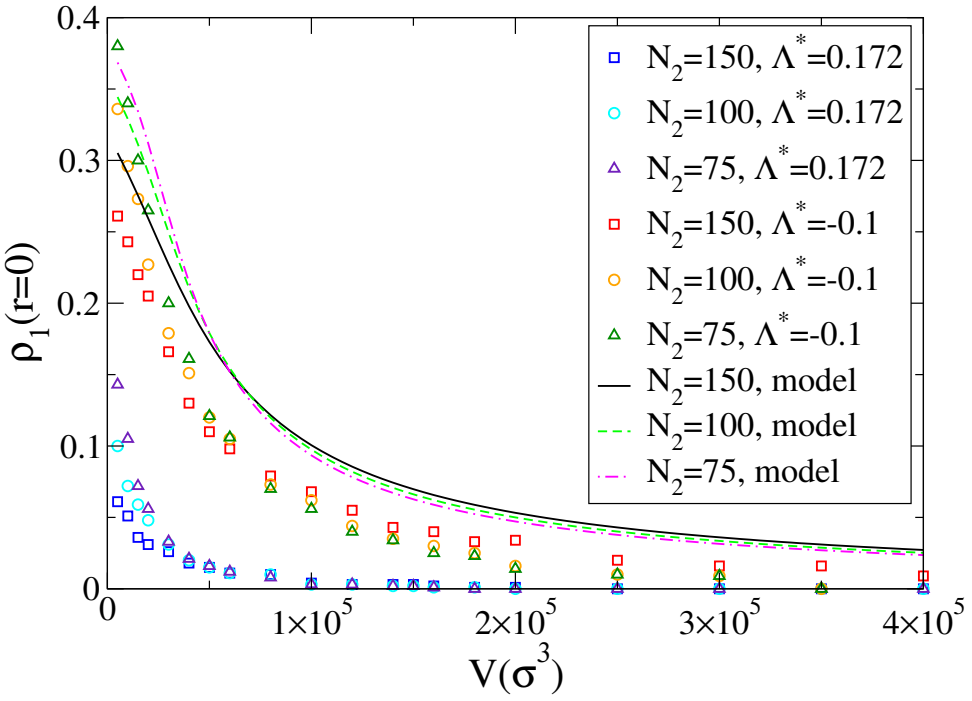

Figure 3.23: Core density $\rho_1(r = 0)$ as a function of V. The point represent simulation data and the solid lines represent the predictions of the non-volatile liquid drop model described in Section III, with $b_0 = 0$.

3.4.3 Comparison with Non-volatile liquid drop model

Figs. 3.21 and 3.22 show fits of the liquid drop model to our simulation data, where we have used b_0 and γ as fit parameters, while fixing the remaining parameters. The model fits the data well for both values of Λ^*, and all non-volatile drop sizes, over the the entire range of volumes studied. The values of γ^* range from 1.59-1.80 and 1.92-2.36 for $\Lambda^* = -0.1$ and 0.172 respectively. These values are higher than the surface tension for the pure fluid of component one and are physically reasonable, but we would expect the true surface tension

of the drop to be dependent on the mole fraction of the components and this effect has been ignored in our model. We also find that the fit values for b_0 are negative. This reflects the fact that the model assumes all n_1^d condensed particles are uniformly distributed in the drop rather than having some partitioned to the surface, so it over estimates the degree to which the particles like to mix. A key feature of the models is that it predicts the transition between small and large drops should be accompanied by a discontinuous increase in n_1^d as a function of V. The simulation trajectories show that the thin films form spontaneously and there is no clear sign of nucleation like behaviour or of the expected discontinuity in the equilibrium droplet size, but these may be obscured to some degree by surface absorption.

We also compare the model predictions for the core density using $\rho_1(r = 0) = \rho_1 = n_1^d/(\nu_1 n_1^d + \nu_2 N_2)$ because it is assumed the components are uniformly mixed. Fig. 3.23 shows that the model, assuming ideal mixing ($b_0 = 0$) correctly predicts the dependency of $\rho_1(r = 0)$ on N_2, including the inversion of the trend as a function of the V. Fitting the model to the data using b_0 and γ as fit parameters yield excellent looking curves, but the two fit parameters become highly anti-correlated and particle size dependent.

3.4.4 Comparison with Lattice Gas Model for Monolayer Adsorption on a Nano Particle

Here we used Eq. 3.27 to find the film size for different droplets with ϵ and l being used as fit parameters. Table 3.1 shows the fit parameters used for partially miscible case where $\Lambda^* = 0.172$. Fig. 3.24 illustrates the results for nano-droplet sizes 75, 100 and 150 for different volumes and the model fits for those nano-droplets. As can be seen from Fig. 3.24, simulations for large volumes appears to agree well with the model, since at large volumes there are only few ($\sim 10 - 20$) particles on the surface of nano-droplet. However for small volumes we clearly see a film formation and some mixing into the core of the droplet, but the lattice model cannot account for this.

Table 3.1: Lattice model fit parameters ϵ and l for partially miscible case.

N_2	l	ϵ	n
75	20.77	-1.52	300
100	21.41	-1.85	300
150	15.21	-3.12	300

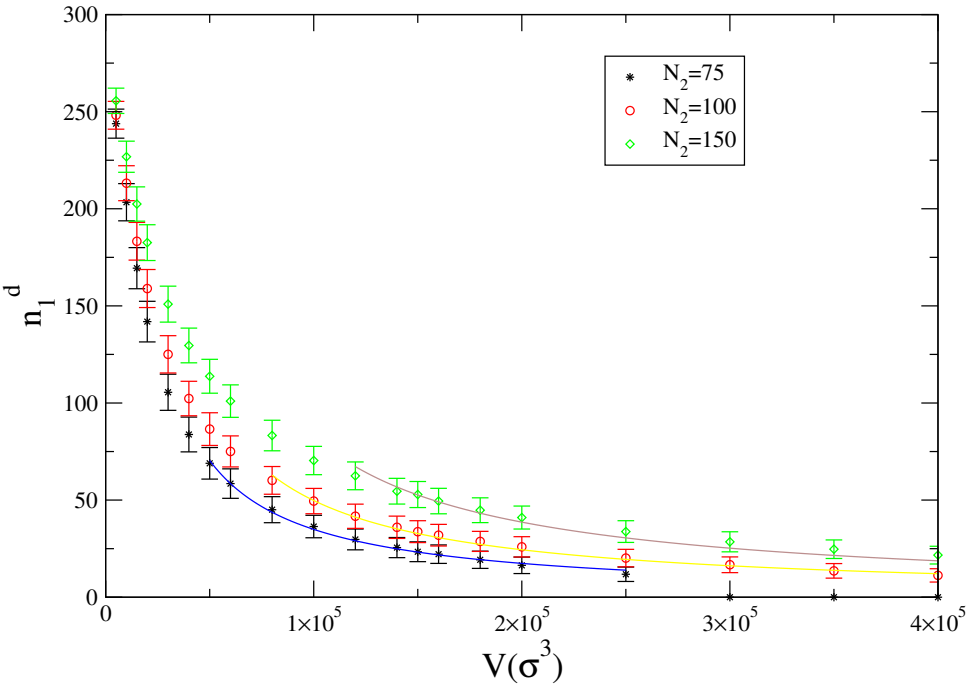

Figure 3.24: Film sizes for different volumes for different nano-droplet sizes and lattice adsorption model fits ($\epsilon_{12} = 1.414$). Solid lines are model fits.

Table 3.2 shows fit parameters used for partially miscible case. Fig. 3.25 illustrates the film sizes versus different volumes for a partially miscible case where $\epsilon_{12} = 1.550$. The increase in the interaction parameter ϵ_{12} causes to increase in film size as expected and simulation results agree well with the model for large volume. Although we get nice fits to our simulation results, both table shows that the trend in the fit of l is wrong, because it decreases as N_2 increases. We would expect l to increases as N_2 increases.

Table 3.2: Lattice model fit parameters ϵ and l for miscible case.

N_2	l	ϵ	n
75	13.70	-3.02	300
100	10.09	-4.10	300
150	9.97	-4.66	300

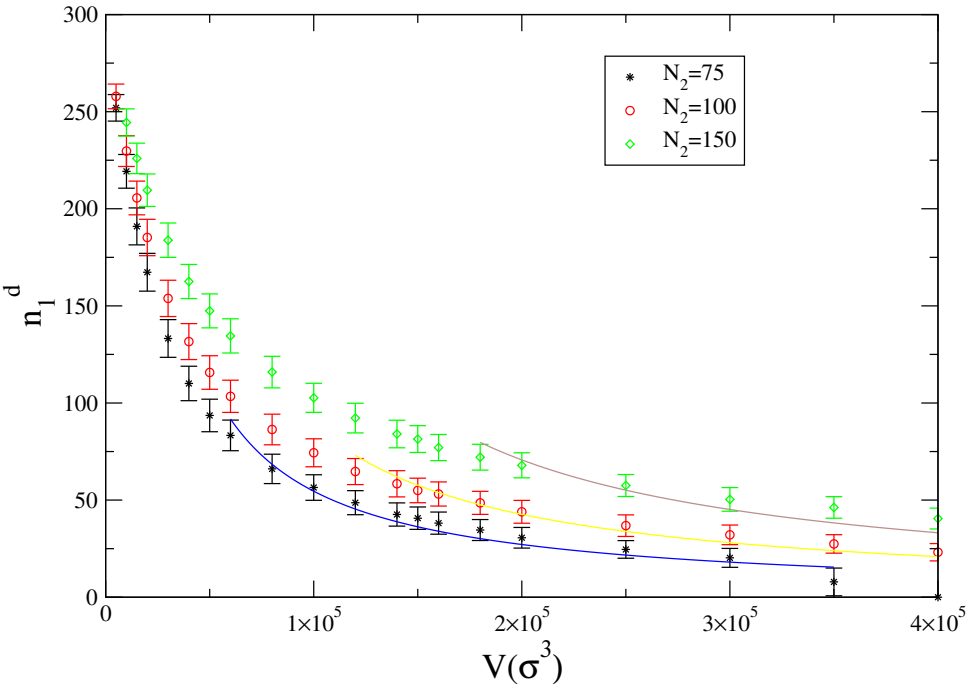

Figure 3.25: Film sizes for different volumes for different nano-droplet sizes and lattice adsorption model fits ($\epsilon_{12} = 1.550$). Solid lines are model fits.

3.5 Discussion and Conclusion

In this chapter, we have performed a series of molecular dynamics simulations to study the condensation of a vapour onto a non-volatile drop for both miscible and partially miscible binary Lennard-Jones mixtures. In the canonical ensemble the drop grows spontaneously as the vapour condenses, but eventually it comes to equilibrium as the vapour phase is depleted. When V is large, a submonolayer amount of the vapour is adsorbed onto the drop with the particles being distributed over the droplet surface in small clusters. Some mixing into the core does occur for the miscible mixtures but no mixing is observed for the partially miscible systems. When V is small enough to cause a substantial number of vapour particles to condense, we see a film growth mechanism that is dominated by cluster-cluster coalescence due to the restricted surface area available on the nanoscale sized drop. This is likely to be a common feature of nucleation and growth mechanisms in nanoscale systems and is in contrast to the usual mechanisms observed during film formation on macroscopic surfaces that usually occur through the addition and loss of individual particles to and from isolated

clusters. Once a monolayer is formed, we also begin to see mixing into the core for the droplet for the partially miscible systems which is a sign that the droplet core has started to dissolve.

We also developed the non-volatile liquid drop model, combined with elements of the regular solution theory, to described the general features of free energy surface associated with droplet growth in nanoscale systems. The free energy landscape of the model for partially miscible components exhibits a hysteresis loop similar to that observed in deliquescence and efflorescence of small particles, caused by the presence of a nucleation barrier between the small drop and large dissolved drop phases. This transition resembles elements of the solubility transition described by Talanquer and Oxtoby [32] using DFT. However, the DFT model directly includes effects due surface absorption where our model ignores this feature, even though our simulations show that these are important.

A number of capillarity based models have been developed to study deliquescence in small particles and capture the effects of partial dissolution of the solid phase by introducing a surface phase involving condensed solvent and small amounts of the dissolved salt surrounding a pure solid phase core. These models involve conditions of the equality of the chemical potentials in the vapour solvent and surface phase solvent, as well as equality of chemical potentials for the solid salt and the dissolved surface salt. Our study suggests that it may be useful to develop similar thermodynamics models to describe the solubility transition in non-volatile liquid drops where the additional element involves the equality of chemical potentials for the vapour, surface absorbed and dissolved core solvent phases. In addition, experiments [82, 85] have shown that large atmospheric aerosols made from complex mixtures of soluble salts, organics and water lead to increasingly complicated cycles of structural transformations where solubility-like liquid-liquid transitions, involving phase separation of organics from inorganic salt solutions, and the deliquescence of the resulting salt solution all occur as a function of the relative humidity. These studies have focused on large particles, but it is likely surface effects will further complicate the nature of these transformations as the particles become smaller.

We also used the non-volatile liquid drop model to explore the role of nucleation in the growth of solution droplets. The model shows that the region of V over which the drops are metastable decreases with increasing initial particle size, which helps explain why Köhler activation is effective for describing the growth properties of large particles and why nucleation

becomes increasing important for the smaller particles. The model also allowed us to examine the effect on the nucleation barrier of renormalizing the free energy to give the correct probability of finding the drop at the transition state, as required by transition state theory and highlighted by Scheifele et al. [18]. In particular, the renormalisation raises the barrier and predicts a slowing down of the nucleation rate in comparison to calculations using the traditional minimum to maximum barrier.

Finally, the model also provides a good description of the results of the simulations, including the core densities, but it is obvious that the assumption of uniform mixing prevents the model from providing quantitative agreement. The model predicts that there should a discontinuity in the size of the drop as it goes through the transition, but this is not observed in our simulations.

Understanding nanoscale particle size effects on the dynamics, thermodynamics and physical structure of small atmospheric aerosol particles remains an important challenge. We have shown that molecular dynamics simulations of a simple binary mixture of Lennard-Jones particles are able to capture the key elements of the dynamics and thermodynamics of the condensation of a solvent vapour onto a non-volatile solute particle. In particular, we shown that cluster-cluster coalescence plays an important role in film formation in nanoscale surfaces and that partially miscible droplets exhibit a solubility transition. We have also shown that simple capillarity based model also captures the main features of the solubility transition, but more complex models are needed to account for surface absorption.

Chapter 4

Summary and Outlook

Nucleation is one of the main mechanisms by which systems change phase. It is an activated process involving the formation of critically-sized embryos that spontaneously grow into the more stable phase. For example, a supersaturated vapour is a metastable state that condenses through the formation of critically sized droplets of the more stable liquid phase. Similarly, crystals nucleate from supersaturated solutions or supercooled liquid through structural fluctuations that eventually lead to the formation of small crystallites. Homogeneous nucleation occurs in the bulk of a material while heterogeneous nucleation, which has a lower free energy barrier and hence occurs more readily, begins at an interface with an impurity.

Heterogeneous nucleation, in particular, plays an important role in the microphysics of clouds where small aerosol particles act as cloud condensation nuclei, act as small chemical reactors in atmospherically important reactions and scatter or absorb light, which contributes to the global radiation balance. Many of these particles also have complex compositions that effect their ability to interact with water vapour, their phase changes, sizes and particle shapes. For example, organic molecules on the ocean surface, formed from both natural and anthropological sources, can coat the surface of sea-salt particles, forming multicomponent aerosol particles, which in return, will affect the hygroscopic behaviour of the aerosol particle. Particle size also plays a significant role. Recent experiments found vapour condensation onto small clusters and nanoparticles, with diameters of 1–24 nm, occurred at supersaturations well below those predicted by classical nucleation theory (CNT) and the Kelvin relation [52]. Sear [86] also found that a microscopic heterogeneity involving a single spin particle was sufficient to accelerate the nucleation rate in a two-dimensional Ising model by as much as four orders of magnitude. While heterogeneous nucleation at the macroscopic level is well known and documented, much less is understood about both the dynamics and thermodynamics of nucleation involving nanoscale heterogeneities.

The goal of this thesis was to understand some of the general features of the condensation of vapours onto nanoscale heterogeneities and to investigate the influence of the solubility of the impurity on this process. To achieve this, the work used a combination of thermodynamic theory and computer simulation to study the condensation of the Lennard-Jones vapour onto nanometer sized impurities of variable size and miscibility. This model was chosen because the homogeneous nucleation of the Lennard-Jones vapour has been studied extensively and the properties of interest, such as the miscibility, could be easily controlled by adjusting the energy of interaction between the Lennard-Jones particles. The thermodynamics models were developed at a level of theory consistent with the capillarity model because these models form the basis for most studies of classical nucleation theory. This involves assuming the materials in the embryo have the same properties as the bulk phases and that the interfaces are sharp and characterized by the surface tension of a bulk, flat interface. The appropriateness of such assumptions to nucleation involving nanoscale heterogeneities is discussed in more detail below.

In Chapter 2, the condensation of a supersaturated vapour onto an insoluble particle is investigated. The phenomenological model developed here has a fixed total number particles N, a fixed volume V, and a constant temperature T. The heterogeneity is considered to be an insoluble, spherical, solid particle, while the liquid forms a uniform film that completely wets the particle, giving rise to a film-particle composite and leaving rest of atoms in the vapour phase, which is treated as an ideal gas. The model captured the main features of heterogeneous nucleation on to a nanoscale impurity and clearly showed that free energy barrier to forming a film once the heterogeneity is small enough, even when the film completely wets the impurity. Complete wetting of a bulk surface leads to spontaneous, barrierless, film formation.

Molecular dynamics simulations were then used to calculate the nucleation rate and free energy barriers for the heterogeneous nucleation of the vapour onto a single atom seed impurity that had particle-particle interactions in the range of $\epsilon/kT = 1.5 - 2.5$. Despite the small size of the impurity, and the weakness of the interactions, the nucleation rate increased, relative to the homogeneous case, by several orders of magnitude by lowering the nucleation barrier and decreasing the size of the critical cluster. A key finding of these simulations was that the presence of this small impurity had no effect on the work of formation of small

clusters but lowered the free energy of forming the larger clusters. An analysis of the MD trajectories, which involved following the size of the largest cluster in the system, showed that most fluctuations involving small clusters did not include the seed particle. However, the seed was always part of the cluster that eventually fluctuated over the barrier. This suggests an interesting balance between the entropic and energetic contributions to cluster formation. The vapour phase can easily make small clusters in a wide variety of ways, so the presence of a single seed particle, with weak interactions has little impact on the probability of observing the small clusters, hence their free energy of formation is unchanged. Larger clusters are rare but the energetic advantage of including the seed, even when the interaction is weak seems to be enough to lower the free energy of formation. A comparison of the simulations results with the model showed that the model, with no fit parameters, provided good estimates of the critical cluster size but systematically over estimated the size of the nucleation barrier. Hence, it would under estimate the nucleation rate. This is consistent with comparisons of classical nucleation theory with homogeneous nucleations rates, and is consistent with the experimental findings that show small heterogeneities are better at initiating nucleation than expected.

In these simulations, the seed particle is small enough that it is modelled by a single Lennard-Jones particle. It could be argued that effects being observed is more closely related to a colligative property of mixing than heterogeneous nucleation. That is, we are seeing binary nucleation involving one atom from a second gas phase. This may well be a possibility as it becomes more and more difficult to distinguish between these phenomena as the heterogeneities become small and smaller, but the agreement between the model and simulations regarding the critical size cluster suggest there is still considerable value to approaching this as a heterogeneous nucleation problem.

In Chapter 3, a Lennard-Jones binary mixture consisting of a non-volatile liquid nanodroplet surrounded by an solvent vapour phase is studied using Molecular Dynamics (MD) simulations and thermodynamic theory to understand the growth of droplets with with different solubilities. Fully miscible and partially miscible cases were considered. In the case of the thermodynamic model, the degree of miscibility was introduced through the real solution model which adds an enthalpic cost to mixing while assuming the entropy of mixing remains ideal. The model clearly exhibits a solubility transition associated with the drop

being dissolved by the absorption of the solvent vapour, similar to the one described by Oxtoby using density functional theory. This transition is also shown to exhibit a hysteresis loop like the one observed in deliquescence. The model also provides a reasonable description of the results of the simulations, including features of the core densities, but it is obvious that the assumption of uniform, ideal mixing prevents the model from providing quantitative agreement.

The model also allowed us to examine the effect on the nucleation barrier of renormalizing the free energy to give the correct probability of finding the drop at the transition state, as required by transition state theory and highlighted by Scheifele et al. [18]. In particular, the renormalisation raises the barrier and predicts a slowing down of the nucleation rate in comparison to calculations using the traditional minimum to maximum barrier. It also suggests that the barrier that correctly predicts the nucleation rates does not go to zero as the limit of stability is approached.

A simple lattice gas model in three dimensions was also developed to describe the absorption of a monolayer of a vapour phase onto a droplet in a closed system. In this model, particles only interacted with each other by excluding volume so each lattice site can only be occupied by a single particle. Particles adsorb onto the nanoparticle with an energy and occupy sites adjacent to the face of the nanoparticle. In effect, this modelled the particle as a solid object and while the fits to the data appear good at low supersaturations, the predictions of particle size from the model had the wrong trend. For high supersaturations, simulations shows mixing into the core and surface enrichment of the solvent phase and this model fails to capture this. Furthermore, many corrections can be introduced to the lattice model to get better fits for higher supersaturations. For example, a soft interface could be modelled by allowing some mixing of the two components in the surface layer of the particle and it might be possible to include multilayer adsorption.

The equilibrium properties of the drops and the dynamics of their formation were studied using molecular dynamics simulations. The growth factor of a drop, which measure the size of the drop after condensations relative to its initial "dry" state is usually used as an order parameter to describe the state of the droplet. Oxtoby's DFT study, and the thermodynamic model developed in this thesis suggest the size of the drop increases in a discontinuous way as the drop dissolves at the solubility transition. The simulation measurements of the size of

the droplets, for both miscible and partially miscible cases, varied continuously as a function of the volume of the system. The radial density profiles of the droplets indicate that there is always some absorption or surface enrichment of the solvent phase at the drop-vapour interface. Mixing into the core of the particles always occurs for the miscible drops, but mixing only occurs below a certain threshold system volume in the partially miscible drops, suggesting there is a solubility transition in these systems as predicted. However, this study also suggests that the total droplet size may not be the best order parameter for describing the solubility transition because surface absorption swamps any signal of particle grow due to the transition.

The simulations show that the growth of the drops exhibit two distinct time trajectories depending on the volume of the system. When the V is large the size of the droplet only increases by a small amount and the vapour essentially remains stable. The growth occurs rapidly by forming a number of small clusters of the solvent that remain on the surface of the drop but are constantly fluctuating in size and number in a dynamic equilibrium with the vapour phase. This represents sub-monolayer absorption.

When V is decreased, the vapour spontaneously condenses onto the droplet, causing a rapid increase the number and size of solvent clusters on the surface of the droplet, but the limited surface area means that the clusters start to interact. Large fluctuations in the size of the largest solvent cluster on the droplet that are decoupled from fluctuation in the total size of the droplet indicate clusters on the surface are coalescing and breaking up again as the film grows. In the end, the fluctuations decrease as all the clusters grow and coalesce to form a single cluster representing the completed film. This type of growth is very different from that observed on bulk surfaces where individual clusters generally grow and nucleate in isolation. It also presents a problem for nucleation theory which assumes that clusters grow by the addition and loss of single molecules. Here, the cluster size fluctuates more rapidly and there is the possibility that the coalescence of two larger clusters could take the system over the barrier faster than expected.

An attempt was made to measure the rate of film nucleation using the mean first passage time, but the results were not reported because it was not possible to obtain good fits to the expected nucleation time curves represented by Eq 1.60. This is probably due this coalescence growth mechanism. It may be possible we could calculate the free energy barriers associated

the solubility transition by using umbrella sampling Monte Carlo simulations. This uses a biasing potential to ensure the correct sampling of states associated with an particular order parameter and does not rely on the dynamics, thus it avoids the problems experienced in the mean first passage time approach.

All the thermodynamic models developed in this thesis used the approximations associated with the capillarity model used in classical nucleation theory. This includes assuming all phases have uniform bulk densities, and that the interfaces are sharp and characterized by the surface tension of a macroscopic, planar interface. However, the focus of the thesis is the condensation of vapours onto nanometer sized heterogeneities and it is questionable if such approximations are valid in these nanoscale systems. For example, in Chapter 2, the density profiles of the clusters containing the impurity never reached bulk values and the interface was very diffuse suggesting it would be difficult to define the surface or a surface tension. Density functional theory provides a molecular level approach that can overcome many of these problems because it treats the free energy as a functional of a smoothly varying density profile and it has been used extensively to study nucleation in droplets. However, the approach can be computationally expensive, as can many molecular level methods, making it difficult to implement in large scale atmospheric models. The attraction of the capillarity model is that there are very few parameters and it is easy to compute. It would therefore be useful to find ways of improving the models to overcome some of the main assumptions while retaining the simplicity. Some steps that have been taken in this direction. Djikaev and Shchekin have introduced a disjoining pressure into the capillarity model to account for the properties of thin films of solution forming on nanoscale salt particles undergoing deliquescence. McGraw [28], also studying deliquescence, developed a thin layer criterion for the formation of thin layers in nanoscale systems. These approaches could be extended to deal with the surface effects described in this thesis work.

In summary, the general features of the condensation of vapours onto nanoscale heterogeneities have been studied using thermodynamic theory and molecular dynamics simulations in this thesis. The phenomenological models discussed in Chapter 2 and 3 were simple and designed to capture general features of phase behaviour and kinetic transformations in nanoscale systems. Similarly, the intermolecular models used in the simulations were simple. However, atmospheric aerosol particles are complex systems containing soluble-insoluble mixtures with

diverse properties such as chemical composition, shape, size and phase. Bertram's [82] work on liquid-liquid phase separation, efflorescence, and deliquescence of mixed particles of ammonium sulfate, organic material, and water, and gas-particle partitioning of atmospheric aerosols highlights how complicated the phase behaviour can become in these mixed system. However, they also show that the Köhler type approach continues to work for large particles. As it has been shown in this thesis, we would expect nucleation of the different phases to play an increasingly important role in these complex systems as the particles become small. One of the main challenges in moving forward will be the development of thermodynamics models capable of capturing the complexity of these systems while remaining simple enough to be used effectively.

References

[1] M. O. Andreae, Science **339**, 911 (2013).

[2] M. Kulmala, J. Kontkanen, H. Junninen, K. Lehtipalo, H. E. Manninen, T. Nieminen, T. Petaja, M. Sipila, S. Schobesberger, P. Rantala, A. Franchin, T. Jokinen, E. Jarvinen, M. Aijala, J. Kangasluoma, J. Hakala, P. P. Aalto, P. Paasonen, J. Mikkila, J. Vanhanen, J. Aalto, H. Hakola, U. Makkonen, T. Ruuskanen, R. L. Mauldin, J. Duplissy, H. Vehkamaki, J. Back, A. Kortelainen, I. Riipinen, T. Kurten, M. V. Johnston, J. N. Smith, M. Ehn, T. F. Mentel, K. E. J. Lehtinen, A. Laaksonen, V. M. Kerminen, and D. R. Worsnop, Science **339**, 943 (2013).

[3] A. A. Zakhidov, R. H. Baughman, Z. Iqbal, C. Cui, I. Khayrullin, S. O. Dantas, J. Marti, and V. G. Ralchenko, Science **282**, 897 (1998).

[4] P. G. Debenedetti, *Metastable Liquids* (Princeton University, Princeton, NJ, 1996).

[5] J. S. Rowlinson, *J D van der Waals: On the Continuity of Gaseous and liquid States* (Nort-Hooland:Amsterdam, 1988).

[6] M. Volmer and A. Weber, Z. Phys. Chem. (Leipzig) **119**, 227 (1926).

[7] R. Becker and W. Döring, Ann. Phys. **24**, 719 (1935).

[8] J. Frenkel, *Kinetic Theory of Liquids* (Clarendon, Oxford, 1946).

[9] Y. B. Zeldovich, Acta Physicochim. URSS **18**, 1 (1943).

[10] K. F. Kelton and A. L. Greer, *Nucleation in Condensed Matter* (Elsevier, 2010).

[11] D. Turnbull, J. Chem. Phys. **18**, 198 (1950).

[12] D. Kashchiev, *Nucleation:Basic Theory with Applications* (Butterworth-Heinemann, Oxford, 2000).

[13] S. Auer and D. Frenkel, Phys. Rev. Lett. **91**, 015703 (2003).

[14] A. Cacciuto, S. Auer, and D. Frenkel, Nature (London) **428**, 404 (2004).

[15] A. Cacciuto and D. Frenkel, Phys. Rev. E **72**, 41604 (2005).

[16] D. Winter, P. Virnau, and K. Binder, J. Phys.:Condens. Matter, **21**,464118, (2009).

[17] N. H. Fletcher, J. Chem. Phys. **29**, 572 (1958).

[18] B. Scheifele, I. Saika-Voivod, R. K. Bowles, and P. H. Poole, Phys. Rev. E **87**, 042407 (2013).

[19] D. J. Wales, *Energy Landscapes: Applications to Clusters, Biomolecules and Glasses* (Cambridge University Press, 2003).

[20] J. H. Seinfeld and S. N. Pandis, *Atmospheric Chemistry and Physics:From Air Pollution to Climate Change* 2nd ed. (Wiley-Interscience, 2006).

[21] C. M. Carrico, P. Kus, M. J. Rood, P. K. Quinn, and T. S. Bates, J. Geophys. Res. **108**, 8650 (2003).

[22] P. Mirabel, H. Reiss, and R. K. Bowles, J. Chem. Phys. **113**, 8200 (2000).

[23] M. E. Wise, G. Biskos, S. T. Martin, L. M. Russell, and P. R. Buseck, Aerosol Sci. Tech. **39**, 849 (2005).

[24] G. Biskos, A. Malinowski, L. M. Russell, P. R. Buseck, and S. T. Martin, Aerosol Sci. Tech. **40**, 97 (2006).

[25] G. Biskos, L. M. Russell, P. R. Buseck, and S. T. Martin, Geophys. Res. Lett. **33**, L07801 (2006).

[26] G. Biskos, D. Paulsen, L. M. Russell, P. R. Buseck, and S. T. Martin, Atmos. Chem. Phys. **6**, 4633 (2006).

[27] K. Hämeri, A. Laaksonen, M. Väkevä, and T. Suni, J. Geophys. Res. **106**, 20749 (2001).

[28] R. McGraw and E. R. Lewis, J. Chem. Phys. **131**, 194705 (2009).

[29] A. Y. Zasetsky, J. J. Sloan, and I. M. Svishchev, J. Phys. Chem. A **112**, 3114 (2008).

[30] P. Mirabel, H. Reiss, and R. K. Bowles, J. Chem. Phys. **113**, 8194 (2000).

[31] Y. Djikaev, R. K. Bowles, H. Reiss, K. Hameri, A. Laaksonen, and M. Vakeva, J. Phys. Chem. B **105**, 7708 (2001).

[32] V. Talanquer and D. W. Oxtoby, J. Chem. Phys. **119**, 9121 (2003).

[33] B. J. Alder and T. E. Wainwright, J. Chem. Phys. **27**, 1208 (1957).

[34] A. Rahman, Phys. Rev. **136**, 405 (1964).

[35] F. H. Stillinger and A. Rahman, J. Chem. Phys. **55**, 3336 (1971).

[36] F. H. Stillinger and A. Rahman, J. Chem. Phys. **61**, 4973 (1974).

[37] M. P. Allen and D. J. Tildesley, *Computer Simulation of Liquids* (Oxford University Press, Oxford, 1989).

[38] D. C. Rapaport, *The Art of Molecular Dynamics Simulation* 2nd ed. (Cambridge University Press, 2004).

[39] D. Frenkel and B. Smit, *Understanding Molecular Simulation.* 2nd ed. (Academic, San Diego, 2002).

[40] J. E. Lennard-Jones, Cohesion **43**, 462 (1931).

[41] L. Verlet, Phys. Rev. **159**, 98 (1967).

[42] J. Wedekind, R. Strey, and D. Reguera, J. Chem. Phys. **126**, 4103 (2007).

[43] J. Wedekind and D. Reguera, J. Chem. Phys. **127**, 4516 (2007).

[44] J. Wedekind and D. Reguera, J. Phys. Chem. B **112**, 11060 (2008).

[45] J. Julin, I. Napari, J. Merikanto, and H. Vehkamaki, J. Chem. Phys. **129**, 234506 (2008).

[46] D. Reguera, J. M. Rubi, and J. M. G. Vilar, J. Phys. Chem. B **109**, 21502 (2005).

[47] J. Julin, I. Napari, and H. Vehkamäki, J. Chem. Phys. **126**, 4517 (2007).

[48] K. Yasuoka and M. Matsumoto, J. Chem. Phys. **109**, 8451 (1998).

[49] D. T. Gillespie, J. Chem. Phys. **74**, 661 (1981).

[50] M. Kulmala, H. Vehkamäki, T. Petäjä, M. D. Maso, A. Lauri, V. M. Kerminen, W. Birmili, and P. H. McMurry, J. Aerosol Sci. **35**, 143 (2004).

[51] M. Kulmala and V. M. Kerminen, Atmos. Res. **90**, 132 (2008).

[52] P. M. Winkler, G. Steiner, A. Vrtala, H. Vehkamäki, M. Noppel, K. E. J. Lehtinen, G. P. Reischl, P. E. Wagner, and K. Kulmala, Science **319**, 1374, (2008).

[53] R. P. Sear, J. Phys. Chem. B **110**, 4985 (2006).

[54] P. R. ten Wolde and D. Frenkel, J. Chem. Phys. **109**, 9901 (1998).

[55] B. Senger, P. Schaaf, D. S. Corti, R. K. Bowles, D. Pointu, J. C. Voegel, and H. Reiss, J. Chem. Phys. **110**, 6438 (1999).

[56] J. Wedekind, J. Wölk, D. Reguera, and R. Strey, J. Chem. Phys. **127**, 154515 (2007).

[57] J. Wedekind, G. Chkonia, J. Wölk, R. Strey, and D. Reguera. J. Chem. Phys. **131**, 114506 (2009).

[58] S. Toxvaerd, J. Chem. Phys. **117**, 10303 (2002).

[59] D. Suh, W. Yoon, M. Shibahara, and S. Jung, J. Chem. Phys. **128**, 154523 (2008).

[60] D. Suh and K. Yasuoka, J. Phys. Chem. B **115**, 10631 (2011).

[61] C. L. Weakliem and H. Reiss, J. Chem. Phys. **99**, 5374 (1993).

[62] D. Reguera, R. K. Bowles, Y. Djikaev, and H. Reiss, J. Chem. Phys. **118**, 340 (2003).

[63] V. G. Baidakov, S. P. Protsenko, Z. R. Kozlova, and G. G. Chernykh, J. Chem. Phys. **126**, 214505 (2007).

[64] J. Wedekind, D. Reguera, and R. Strey, J. Chem. Phys. **125**, 4505 (2006).

[65] B. Hess, C. Kutzner, D. van der Spoel, and E. Lindahl, J. Chem. Theory Comput. **4**, 435 (2008).

[66] J. Wedekind, D. Reguera, and R. Strey, J. Chem. Phys. **127**, 4501 (2007).

[67] S. E. M. Lundrigan and I. Saika-Voivod, J. Chem. Phys. **131**, 4503 (2009).

[68] K. Laasonen, S. Wonczak, R. Strey, and A. Laaksonen, J. Chem. Phys. **113**, 9741 (2000).

[69] G. Chkonia, J. Wölk, R. Strey, J. Wedekind, and D. Reguera, J. Chem. Phys. **130**, 064505 (2009).

[70] S. T. Martin, Chemical Reviews **100**, 3403 (2000).

[71] H. Köhler, Gepfys. Pub. Krestiana **1**, 1 (1921).

[72] H. Köhler, Gepfys. Pub. Krestiana **2**, 6 (1922).

[73] H. Köhler, Trans. Faraday Soc. **32**, 1152 (1936).

[74] H. Reiss and G. J. M. Koper, J. Phys. Chem. **99**, 7837 (1995).

[75] I. N. Tang and H. R. Munkelwitz, J. Geophys. Res. **99**, 18801 (1994).

[76] C. B. Richardson and T. D. Snyder, Langmuir **10**, 2462 (1994).

[77] J. Hakala, J. Kangasluoma, and T. Petäjä, Hygroscopicity of sub-6 nm sodium chloride particles. In *NUCLEATION AND ATMOSPHERIC AEROSOLS: 19th International Conference*, pages 480–482. AIP.

[78] Y. S. Djikaev, J. Chem. Phys. **116**, 9865 (2002).

[79] A. K. Shchekin, I. V. Shabaev, and A. I. Rusanov, J. Chem. Phys. **129**, 214111 (2008).

[80] R. P. Sear, Europhys. Lett. **83**, 66002 (2008).

[81] T. Semeniuk, M. Wise, S. T. Martin, L. M. Russel, and P. Buseck, Atmos. Environ. **41**, 6225 (2007).

[82] A. K. Bertram, S. T. Martin, S. J. Hanna, M. L. Smith, A. Bodsworth, Q. Chen, M. Kuwata, A. Liu, Y. You, and S. R. Zorn, Atmos. Chem. Phys. **11**, 10995 (2011).

[83] Y. Wang, S. Teitel, and C. Dellago, J. Chem. Phys. **122**, 214722 (2005).

[84] A. S. Clarke, R. Kapral, and G. N. Patey, J. Chem. Phys. **101**, 2432 (1994).

[85] Y. You, L. Renbaum-Wolff, M. Carreras-Sospedra, S. J. Hanna, N. Hiranuma, S. Kamal, M. L. Smith, X. Zhang, R. J. Weber, J. E. Shilling, D. Dabdub, S. T. Martin, and A. K. Bertram, *Proceedings of the National Academy of Sciences*, 109(33):13188–13193, 2012.

[86] R. P. Sear, J. Chem. Phys. **131**, 074702 (2009).